

PROJECTILE FRAGMENTATION OF KRYPTON
ISOTOPES AT INTERMEDIATE ENERGIES

By

Raman Pfaff

A DISSERTATION

Submitted to
Michigan State University
in partial fulfillment of the requirements
for the Degree of

DOCTOR OF PHILOSOPHY

Department of Physics

1996

ABSTRACT

PROJECTILE FRAGMENTATION OF KRYPTON ISOTOPES AT INTERMEDIATE ENERGIES

By

Raman Pfaff

To gain a better understanding of the production of projectile-like fragmentation products and exotic isotopes and to provide information on the stability of nuclei along the path of the rapid-proton capture process, isotopic cross sections from the reactions $^{78}\text{Kr} + ^{58}\text{Ni}$ at 70 MeV/nucleon and $^{86}\text{Kr} + ^{27}\text{Al}$ at 75 MeV/nucleon were measured at 0° with the A1200 fragment separator at the National Superconducting Cyclotron Laboratory. The particle stability of ^{69}Br , which is a critical isotope to the path of the rapid-proton capture process, was thoroughly probed during the fragmentation of ^{78}Kr , and it appears to be particle unstable. The experimental production cross section data are compared to previous krypton isotope fragmentation data as well as to an intranuclear cascade code developed for higher energies (> 200 MeV/nucleon) and a semiempirical parametrization derived from high energy systematics. An effort was made to explore the dependence of the N/Z ratio of the projectile on the observed isotopic distributions and to place tighter limitations of the half-lives on several nuclei important to the rapid-proton capture process.

To My Grandmother

Clara Kruh

ACKNOWLEDGEMENTS

Of all the cyclotrons, in all the labs, in all the world, I had to walk into this one... I'll start out by thanking my advisor Walt Benenson for giving me the opportunity to do research here at the NSCL, and pursue my own research interests along the way. I would also like to thank Dave Morrissey for helping me along my 'fragmented' research path. Without the helpful guidance of those two gentlemen, I would not have managed to become a NSCL graduate.

When I first started here at the NSCL, John Stevenson, Jim Clayton, and Mike Mohar gave me my "introduction to experimentation," and the countless hours of set-up that go into our research. Without their help, I would not have become one of those (few and proud) individuals that sat around the focal plane discussing the philosophical implications of putting your finger through the silicon detectors.

The majority of my time during graduate school was spent with fellow graduate students. I've met so many interesting (and sometimes helpful) graduate students during my years here and I can't even begin to name them all, but I'll try to mention at least a few (names may occasionally be changed to preserve anonymity). Mike Fauerbach is the only true football fan left here at the lab and we both got to sit around griping about our teams every Monday morning. Besides that, he also helped me with many aspects of my research during our fruitful discussions. Spike Nelson helped to keep me motivated (particularly in

my TV viewing habits) and I hope I've done the same for him. John "the banker" Johnson really helped me get both my undergrad and graduate careers rolling along, and I certainly enjoyed inheriting his NSCL window seat - since I spent a good number of years staring at the Chemistry building (among other things). And now, in no particular order, here are some other people who I've met during my years here at MSU and will not soon forget: Shigeru Yokoyama, Renan Fontus, Sally Gaff, The Omen, Mike Lisa, Phil Zecher, Paul "I know where some paper is" Mantica, Erik Hendrickson, Dan Marino, Lily "let's burn the couch" Hoines, Larry Phair, Bo Zhang, Craig Snow, Ric Harkewicz, Dan "sports manager" Cebra, Ned Kelley, Maggie Hellström, Bob Kryger, Jim Brown, Jac Caggiano, Mathias Steiner, Jerry Seinfeld, Rooster McConville, Bill "Dolfan" Llope, Easwar Ramakrishnan, Tater "let's go to the PB and discuss quantum" Sackett, Kevin "I'm off to Fiji" Liddiard, Darren Star, Paul Rutt, Debbie "I'll get it published for you" Brodbar, Rilla McHarris, Jon Kruse, Chris "Mr. Clean" Powell, Stephanie Holland, Ninamarie Levinsky, Dave and Cheryl Bartley, Helmut Laumer, and Lord Melbeck. If I missed anyone (I'm sure I did), let me know and I'll be sure to get your name on the WWW version.

Victor Dolenc is another person who I will forever be grateful to. He flew over from Yugoslavia and did a rather amazing surgery to remove a tumor from my head. He deserves a long round of applause. Also, special thanks to my uncle, Bob Moskowitz, who helped get me connected with Dr. Dolenc.

A few other things here at MSU that I'll always be thankful for during my years as a grad student include: the Wharton Center, the MSU Theater Department, the daily aerobics bunch, all the people that played on the various Bozon teams with me (maybe one day we'll actually have a winning season), and Espresso Royale (they really need one of

those in Los Alamos!). The Peanut Barrel is also one of those places that every town should have, and I'm sure I'll always make it back there every time I roll through town.

There are a few friends I met many years ago that I'd like to mention. Eric Hoffmann and Nelson Howard were two guys from Miami that I'll never forget (motorcycle rides, beach runs, Fin games, trips to the pool hall at 3 am....). Mike Shorna and his family helped me get my life going after high school and I'll always be thankful. And special thanks to Miriam Rojas, who actually talked me into attending college while enjoying a cool day in the "pit" at MDCC.

I'd also like to give my thanks to "Doc" Erin Shore, who saw me through a good part of my days as a graduate student. She helped me enjoy many evenings at Wharton – from the last row of the balcony to the center of the front row, survive the daily grind while studying for the comps, get through a long year and a half of a medical adventure, and enjoy life in general. I wish her the best and am sure she will have a great medical career.

The one thing that is obvious to me now (as I've made it to page three of this and can still think of two hundred more people...and I must leave for New Mexico in about ten minutes) is that it's impossible to mention all the people that have helped me get my Ph.D., and also impossible to let them know via these "acknowledgments" how much I appreciate their help and friendship – everything from daily "mac-chats" in the hallway to serious discussions about research analysis.

Finally, I'd like to thank my parents who gave me a great start to my education by letting me read anything I could get my hands on.

TABLE OF CONTENTS

	LIST OF TABLES	vii
	LIST OF FIGURES	viii
1	Introduction	1
1.1	Projectile Fragmentation	1
1.1.1	Energy regimes of projectile fragmentation	4
1.2	Purpose of the present work	6
2	Previous Research/Theory	10
2.1	Applicable Systematics	11
2.2	ISApac Model	19
2.3	Recent Research	27
2.3.1	Krypton Fragmentation at 44 MeV/nucleon	28
2.3.2	Krypton Fragmentation at 200 MeV/nucleon	32
2.3.3	High Energy Krypton Fragmentation	36
2.3.4	Rapid-Proton Capture Process	41
3	Experimental Apparatus and Analysis	48
3.1	The A1200 Fragment Separator	48
3.2	Detector Setup	49
3.3	Electronic Setup	51
3.4	Isotopic Identification	51

3.5	Parallel Momentum Distributions.....	56
4	Results and Discussion	60
4.1	Fragmentation of ^{86}Kr Projectiles.....	60
4.1.1	Momentum Widths	60
4.1.2	Momentum Transfer	64
4.1.3	Isotopic Cross Sections.....	68
4.2	Fragmentation of ^{78}Kr Projectiles.....	70
4.2.1	Isotopic Cross Sections.....	71
4.2.2	Memory Effect	74
4.2.3	Implications for the rp-process	78
5	Summary	82
A	Measured Cross Sections	84
B	ISApac Input Parameters	91
	List of References	92

LIST OF TABLES

Table 4.1:Fitted slope parameters for individual elements from ^{86}Kr fragmentation. . . .	66
Table A.1:Isotopic cross sections from $^{78}\text{Kr} + ^{58}\text{Ni}$ at 75 MeV/nucleon.	85
Table A.2:Isotopic cross sections from $^{86}\text{Kr} + ^{27}\text{Al}$ at 70 MeV/nucleon.	89

LIST OF FIGURES

FIGURE 1.1:	A simplistic picture of the projectile fragmentation process.	2
FIGURE 2.1:	Bar chart showing importance of in RNB experiments at the NSCL.	10
FIGURE 2.2:	A plot used to determine a parametrization for the momentum width from both target and projectile fragmentation residues.	12
FIGURE 2.3:	The plot used to determine the parametrization for the momentum shift that fragments undergo during both target and projectile fragmentation.	12
FIGURE 2.4:	The experimental data originally used for the parametrization of the memory effect.	17
FIGURE 2.5:	Parametrization of the “memory effect” from Eq. 2.14. The data used for this parametrization are shown in Figure 2.4.	18
FIGURE 2.6:	Nucleon-nucleon cross sections as a function of incident energy.	21
FIGURE 2.7:	Nuclear density for ^{86}Kr from the ISABEL code, a Yukawa distribution and a square well density distribution.	23
FIGURE 2.8:	Simple view of the energy diagram used to determine created holes, captured particles, and free particles in the ISABEL code.	25
FIGURE 2.9:	The momentum distribution for $^{72}\text{Ge}^{31+}$ from the fragmentation of $^{84}\text{Kr} + ^{27}\text{Al}$ at 44 MeV/nucleon.	29
FIGURE 2.10:	The two-peak structure observed for several momentum distributions from the reaction $^{86}\text{Kr} + ^{27}\text{Al}$ at 44 MeV/nucleon.	29
FIGURE 2.11:	Cross sections resulting from $^{84}\text{Kr} + ^{27}\text{Al}$, ^{103}Rh , ^{197}Au at 44 MeV/nucleon.	30

FIGURE 2.12:	Selected yields from 44 MeV/nucleon krypton fragmentation along with corresponding predictions from a high energy fragmentation model.	31
FIGURE 2.13:	Cross sections from krypton fragmentation at 200 MeV/nucleon.	32
FIGURE 2.14:	Velocity shift for the fragmentation products resulting from $^{84}\text{Kr} + ^{197}\text{Au}$ at 200 MeV/nucleon.	34
FIGURE 2.15:	Parallel momentum widths for the intermediate energy fragmentation products.	35
FIGURE 2.16:	Typical momentum distribution observed during high energy fragmentation - in this case $^{86}\text{Kr} + ^9\text{Be}$ at 500 MeV/nucleon.	36
FIGURE 2.17:	Parallel momentum widths observed during high energy krypton fragmentation of $^{86}\text{Kr} + ^9\text{Be}$	37
FIGURE 2.18:	Momentum shifts observed during the fragmentation of $^{86}\text{Kr} + ^9\text{Be}$ at 500 MeV/nucleon.	38
FIGURE 2.19:	The momentum shift for the fragments near the mass of the projectile during high energy krypton fragmentation.	39
FIGURE 2.20:	Cross sections for the reaction products resulting from high energy fragmentation of $^{86}\text{Kr} + ^9\text{Be}$ at 500 MeV/nucleon.	40
FIGURE 2.21:	The CNO and HCNO cycles.	42
FIGURE 2.22:	Proposed rp-paths for varied temperature and density conditions.	43
FIGURE 2.23:	Proposed path of the rp-process for the region applicable to the present research.	44
FIGURE 2.24:	Isotopic yields resulting from $^{78}\text{Kr} + ^{58}\text{Ni}$ at 65 MeV/nucleon.	45
FIGURE 2.25:	Yield from the fragmentation of $^{78}\text{Kr} + \text{Ni}$ at 73 MeV/nucleon.	46
FIGURE 3.1:	A schematic diagram of the A1200 fragment separator.	50
FIGURE 3.2:	A schematic diagram of the electronic setup that was used during the fragmentation experiments.	52

FIGURE 3.3:	Turning radius vs. horizontal position for PPAC0 at Dispersive Image #2 that was observed during the ^{78}Kr fragmentation experiment.....	53
FIGURE 3.4:	A plot of ΔE vs. TOF observed during the reaction $^{78}\text{Kr} + ^{58}\text{Ni}$. The arrow indicates the “gap” where ^{69}Br should be observed.	54
FIGURE 3.5:	Energy and time calibrations for the detectors during the ^{86}Kr fragmentation experiment.	55
FIGURE 3.6:	The A,Z, and Q resolution obtained in the ^{86}Kr fragmentation experiment.....	57
FIGURE 3.7:	The momentum distribution of $^{80}\text{Br}^{35+}$ with varied Gaussian fits. The arrow indicates the projectile momentum.	58
FIGURE 4.1:	Parallel momentum distribution widths for isotopes observed during the fragmentation of ^{86}Kr	61
FIGURE 4.2:	Parallel momentum width from recent krypton fragmentation experiments.....	62
FIGURE 4.3:	Momentum transfer vs. mass loss for the projectile-like fragments observed during ^{86}Kr fragmentation at 70 MeV/nucleon.	65
FIGURE 4.4:	Isotopic cross sections determined from the fragmentation of $^{86}\text{Kr} + ^{27}\text{Al}$ at 70 MeV/nucleon.	69
FIGURE 4.5:	Centroids of parallel momentum distributions for isotopes observed during projectile fragmentation of $^{78}\text{Kr} + ^{58}\text{Ni}$ at 75 MeV/nucleon.....	71
FIGURE 4.6:	Mass distributions for the Z=30 to Z=38 isotopes recorded while magnetic rigidity was optimized for observation of ^{69}Br	72
FIGURE 4.7:	Isotopic cross sections determined from $^{78}\text{Kr} + ^{58}\text{Ni}$ at 75 MeV/nucleon.	73
FIGURE 4.8:	Parametrization of the memory effect which shows data from several krypton fragmentation experiments.	76
FIGURE 4.9:	Halfives calculated using the WKB approximation for ^{69}Br and ^{73}Rb	80

Chapter 1

Introduction

1.1 Projectile Fragmentation

In recent years the use of radioactive nuclear beams (RNB's) has become a rapidly moving and promising specialty of nuclear science, and the development and implementation of RNB facilities has become a high priority at many research institutions. There are only 263 stable isotopes in nature but estimates predict there may be more than 8000 radioactive isotopes which could be created and observed. These radioactive isotopes are vital to the study of many aspects of nuclear physics including mass models, half-lives, cross sections, shell structure, isomeric production rates, and astrophysical processes. When planning such studies for the laboratory, target, projectile, and beam current requirements must be explored in an effort to understand the practicality of the experiment. For this aspect of the planning it is necessary to have reliable predictions for the most basic results of the fragmentation process – most notably the expected cross sections for the particles of interest.

In 1947 Serber [ser47] proposed the idea that peripheral highly energetic heavy-ion reactions can be described as a two-step process in which each step occurs in clearly separated time intervals. The first step describes the initial collision between the constituents of the target and projectile nucleus and occurs rapidly, on the order of 10^{-23}

seconds. This step can lead to highly excited objects (prefragments) which are usually very different from the final observed fragments. Before detection, the prefragments lose their excitation energy through the emission of particles (neutrons, protons, and small clusters) and γ -rays. This second step (deexcitation) occurs slowly relative to the first step and typically occurs on the order of 10^{-16} to 10^{-18} seconds (depending on the excitation energy of the prefragment). A simple portrayal of this process is shown in Figure 1.1 in which the overlapping region of the target and projectile is sheared off, leaving an excited prefragment. The prefragment then deexcites through statistical emission and becomes the final observed fragment.

Due to the differences in the physical nature of the two processes, one usually uses separate theoretical models to describe the two individual steps of the fragmentation. To simulate the rapid first step of the nuclear reaction an intranuclear cascade model (INC) is often used. The INC models treat the projectile–target interaction as simple nucleon-

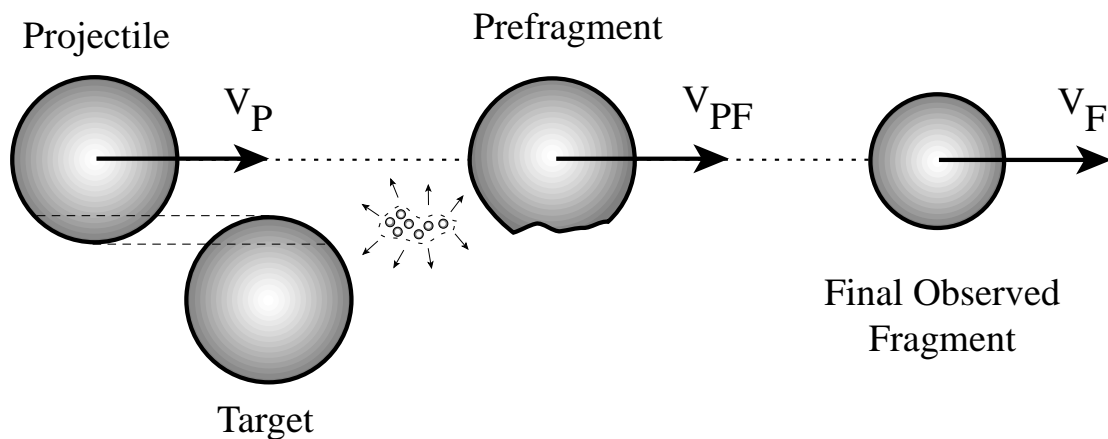


FIGURE 1.1: A simplistic picture of the projectile fragmentation process.

nucleon collisions in a microscopic manner (further details will be discussed in the subsequent chapter). After performing the INC calculation, one deals with excited prefragments that are characterized by their atomic mass, proton number, excitation energy, and their linear and angular momentum. These prefragments are usually far away from their ground state and have a very short lifetime. To describe the deexcitation process a statistical evaporation code is generally used. These codes were originally developed (and successfully used) to describe compound nucleus reactions near the Coulomb barrier. The basic properties of INC models and some details of the INC code used in the present research will be described in Chapter 2 along with a discussion of the statistical evaporation code. The results of the present research will be compared to the predictions from the ISApac model [fau92], which uses the INC code ISABEL [yar79] in conjunction with a statistical evaporation code PACE [gav80].

Use of the INC model together with the statistical evaporation code is a computer intensive method that has been used to gain further insight into the physical properties involved in the fragmentation process. Because it is often necessary to estimate cross sections quickly during the preparation of an experiment, a relatively simple parametrization is often a more practical method than a computer intensive solution. Sümmerer *et al.* [sum90] used the data available in 1988 to develop the widely used EPAX parametrization, which has proved reliable for a large portion of the high energy radioactive nuclear beam research performed over the past decade. The parametrization was developed from high energy data, and the only input parameters are the mass and proton number of the projectile and target. The energy of the projectile is not considered to be an essential input parameter due to the fact that EPAX was geared towards high energy

fragmentation in which the nucleon-nucleon cross section is relatively constant (limiting fragmentation). However, recent advances in technology have allowed experiments to be performed using intermediate mass projectiles at intermediate energies, in which energy dependent factors could cause the EPAX parametrization to fail. The EPAX parametrization and comparisons to the present experimental results will be discussed in subsequent chapters.

1.1.1 Energy regimes of projectile fragmentation

The bombarding energies used for projectile fragmentation experiments have changed with technological advances. The processes which occur at the various energies differ tremendously. Low energy “fragmentation” was available for many years, and a large amount of data has been accumulated [fle74]. At low energies ($E/A \leq 20$ MeV/nucleon), several different reaction mechanisms contribute to the process. Reactions in this energy regime are generally not considered “true” fragmentation and can not be described by Serber’s [ser47] simple two-step process. The time of interaction is long, due to the slow relative velocity between the target and the nucleus, and the Fermi momentum of the individual nucleon constituents of the target and the projectile is greater than the momentum of the nucleus itself. These factors can result in a combination of processes (dependent on the impact parameter of the collision) including Coulomb scattering, incomplete fusion, complete fusion, and compound nucleus interaction.

Reactions occurring at much higher energies ($E/A \geq 200$ MeV/nucleon) are considered to be “pure” fragmentation as was discussed by Serber. It should be noted that the energy limits are not exact since transitions between dominant processes occur gradually as a function of beam energy. In this situation the kinetic energy is on the order

of magnitude of the rest mass of the constituent nucleons, and the interaction time between the target and the projectile is very short. Central collisions will result in a “shattering” of the projectile into light particles and individual nucleons while distant interactions will undergo Coulomb scattering and excitation. Peripheral reactions will exhibit “pure” fragmentation in which the region of the projectile that overlaps the target during the interaction will be torn off, leaving an excited prefragment. As accelerators improved over the past few decades, many high energy experiments using heavy fragments were performed [bol86, gol78]. In recent years exploration of fragmentation in the intermediate energy regime ($20 \text{ MeV/nucleon} \leq E/A \leq 200 \text{ MeV/nucleon}$) has been carried out in an effort to understand the transition from the high energy fragmentation to the complex processes occurring in the low energy regime. This intermediate energy regime has proven to be very interesting and challenging, to both the experimental procedures and theoretical models.

The collection of systematic data in which cross sections and momentum distributions were measured for a large collection of fragmentation products are still limited, but growing. At the National Superconducting Cyclotron Laboratory (NSCL) Souliotis *et al.* [sou91, sou92] performed several experiments involving ^{14}N beam on both ^{27}Al and ^{181}Ta targets at 75 MeV/nucleon and $^{18}\text{O} + ^{27}\text{Al}$ at 80 MeV/nucleon. Fauerbach *et al.* [fau96] studied the fragmentation of $^{40}\text{Ar} + ^9\text{Be}$ at 90 MeV/nucleon. The data available for heavier elements are rather limited due to the complexity of the experiments, from both the technological and analytical side. Until recently, beams comprised of intermediate mass projectiles could not be easily produced at experimental facilities, and analysis was difficult since good energy resolution was needed to separate isotopic charge

states which are prevalent in the intermediate and low energy regimes. Bazin *et al.* [baz90] performed an experiment at GANIL near the low end of the intermediate energy regime that used $^{84}\text{Kr} + ^{27}\text{Al}$, ^{103}Rh , ^{197}Au at 44 MeV/nucleon. In an effort to add to the database of information pertaining to intermediate energy fragmentation performed with intermediate mass projectiles, two experiments were carried out at the NSCL; one involved the fragmentation of neutron-rich $^{86}\text{Kr} + ^{27}\text{Al}$ at 70 MeV/nucleon, and a second experiment with proton-rich $^{78}\text{Kr} + ^{58}\text{Ni}$ at 75 MeV/nucleon.

1.2 Purpose of the present work

The primary goal of the present work was to gain a greater understanding of projectile-like fragmentation in the intermediate energy regime, however, each experiment had specific individual goals. For the fragmentation of the neutron-rich $^{86}\text{Kr} + ^{27}\text{Al}$ system, the cross sections and parallel momentum distributions were measured for many nuclei near the beam mass, and the momentum dependence of the fragmentation products was closely explored – most notably for nucleon pick-up products which occur rarely at high energies. A parametrization was developed to explain the momentum shift observed for fragmentation products that acquired as many as three additional protons in the process. The results of the pick-up process data will be compared to previous experiments which involved neutron pick-up [sou92]. The data from this experiment will also be compared to previous neutron-rich krypton fragmentation experiments which were performed at both higher and lower energies and with the predictions of the ISApax model and the EPAX parametrization.

Fragmentation of the proton-rich $^{78}\text{Kr} + ^{58}\text{Ni}$ system at 75 MeV/nucleon was performed in an effort to provide further information on the stability of nuclei along the

path of the rapid-proton capture process (rp-process). The rp-process was first proposed by Wallace and Woosley [wal81] who showed that heavy isotopes (up to $A=100$) could be produced in astrophysical processes in which high temperatures and densities exist, such as supernova shock waves, novae, and x-ray bursts [wor94, cha92]. The rp-process proceeds via a sequence of proton capture and β^+ decays near and sometimes along the proton drip line. Particle stability and half-lives are important in determining the rate and actual path of the rp-process since it occurs during explosive processes in short time periods ($\sim 10 - 100$ s). When the rp-process path must pass through isotopes with long β^+ half-lives, the rp-process will be slowed or terminated. Mass models [jan88] differ on predictions of the exact position of the proton drip line which prompted several experiments that looked for possible termination points of the rp-process [rob90, moh91]. In recent years the odd Z isotopes of ^{65}As and ^{69}Br have been investigated as the most likely termination points because the half-lives of ^{64}Ge and ^{68}Se , the proton capture targets, are thought to be longer than the time scale of the explosion that provides the proton flux. Evidence for the existence of ^{65}As and ^{69}Br (along with four other new isotopes) was first reported by Mohar *et al.* [moh91]. A subsequent experiment measured the half-life of several of the isotopes including ^{65}As ; however, ^{69}Br was not observed [win93, hel95]. A recent experiment at GANIL [bla95] reported five new isotopes (^{60}Ga , ^{64}As , $^{69,70}\text{Kr}$, and ^{74}Sr) which extended the experimentally observed proton drip line, but no events were attributed to ^{69}Br . The latter experiment had a flight path six times longer than the one performed by Mohar *et al.* [moh91], indicating that ^{69}Br was not stable or had a very short half life (< 100 ns). To explore these possibilities the ^{78}Kr fragmentation

experiment was performed such that it would be sensitive to nuclei with very short (~ 100 ns) half-lives.

The present study of the proton-drip line nuclei also involved the measurement of production cross sections of many proton-rich isotopes. The data from both the ^{78}Kr and ^{86}Kr fragmentation data allowed a parallel investigation of the so-called “memory” effect [chu71] by comparison of the ^{78}Kr to the ^{86}Kr results. The memory effect deals with the fact that fragments close to the mass of the projectile can “remember” the N/Z ratio of the projectile. Prefragments with (very) high excitation energies are likely to produce final products along a ridge parallel to the valley of β stability (e.g. Stephan *et al.* [ste91]) due to evaporation of many nucleons. The final observed fragments that are far in mass from the projectile will have no “memory” of the N/Z ratio of the projectile. Prefragments that have low excitation energies will not lose many nucleons, will be much closer in mass to the original projectile, and have an N/Z ratio similar to the projectile. The memory effect parametrization is an attempt to describe the rate at which fragments will “forget” the N/Z of the projectile. Isotopic cross sections from fragmentation reactions involving members from both extremes of an isotopic chain can therefore provide crucial information on this influence of the projectile N/Z ratio on the fragment charge dispersion distribution (“memory effect”). Data from the experiment which utilized the very proton-rich ^{78}Kr projectile (N/Z ~ 1.17) are compared to data from the fragmentation of the very neutron-rich krypton isotopes ^{86}Kr (N/Z ~ 1.39) and an earlier experiment [ste91] that involved fragmentation of ^{84}Kr (N/Z ~ 1.33).

The subsequent chapters will present the results from the two intermediate energy fragmentation experiments which used proton- and neutron-rich krypton projectiles. The following subjects will be addressed in detail:

- isotopic cross sections for many projectile-like fragments
- influence of the use of a Gaussian fit on the isotopic momentum widths
- momentum shift parametrization developed for proton pick-up products
- possible termination points of the rapid proton capture process
- lifetime limitations placed on several proton drip-line nuclei
- memory effect parametrization for use in the intermediate energy/mass regime
- comparison of experimental data to the EPAX parametrization
- comparison of experimental data to calculations using the ISApax code.

Chapter 2

Previous Research/Theory

Projectile fragmentation has become a widely used technique for production of radioactive nuclear beams (RNB's) at many facilities [mue93]. In the past decade, new fragment separators have been constructed at Gesellschaft für Schwerionenforschung mbH (GSI), The Institute of Physical and Chemical Research (RIKEN), Grand Accélérateur National d'Ions Lourds (GANIL), and here at the NSCL [arm87, nol89, she91] in an effort to take advantage of the technique of projectile fragmentation.

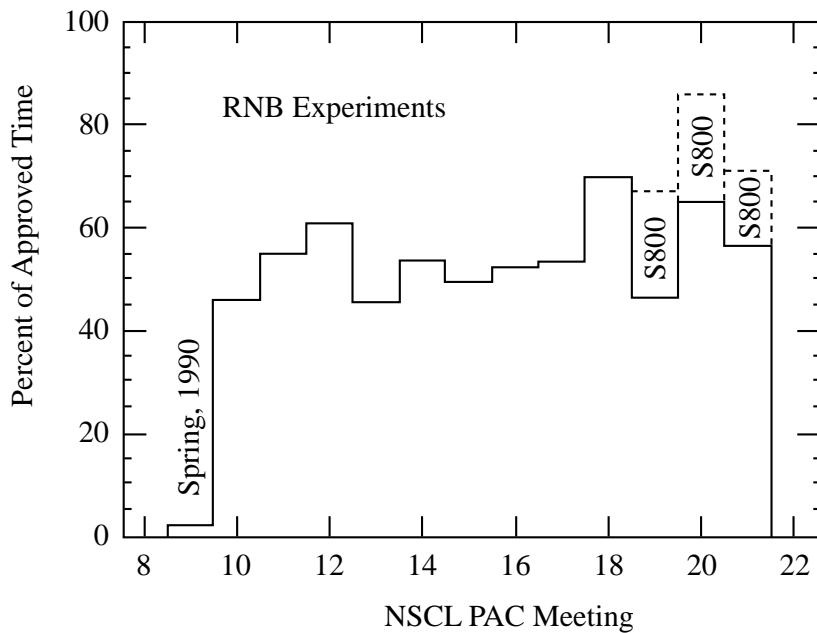


FIGURE 2.1: Bar chart showing importance of in RNB experiments at the NSCL.

Figure 2.1 shows the rapid increase in the percentage of beam time used at the NSCL for RNB research over the past several years and therefore the need for a good understanding of the isotopic production cross sections from various beam and target combinations which will be employed to produce the fragments of interest.

Two techniques are primarily used to predict the cross sections for intermediate and high energy reactions, the EPAX parametrization and an intranuclear cascade (INC) calculation (ISApac is currently a widely used INC code combined with an evaporation code). This chapter will introduce much of the background material which led to the development of the techniques and some recent research which inspired the present work to be performed. The basics of the EPAX parametrization will be discussed in Section 2.1, and Section 2.2 will do the same for the ISApac model. In Section 2.3 a recap will be given for some of the previous research which was performed using krypton projectiles at a variety of energies in an effort to study both projectile fragmentation and limits of isotopic stability important to the rp-process.

2.1 Applicable Systematics

After more than two decades of target fragmentation experiments and a rising use of projectile fragmentation to produce exotic isotopes, parametrizations were needed which could describe three basic observables (the momentum width, longitudinal momentum, and the yield of the fragments) for any target/projectile reaction so that predictions could be made for future experimentation. In 1989 the “Morrissey systematics” [mor89] included a parametrization of the momentum width and momentum transfer of fragmentation products. It was shown that the formalism was applicable to both target and projectile fragmentation which it should be – since the reactions are equivalent

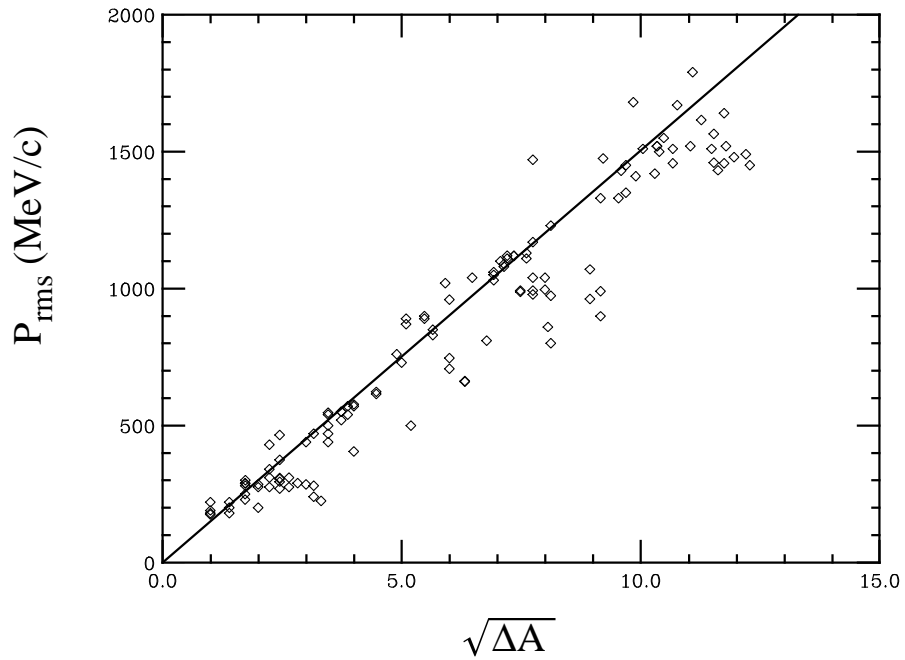


FIGURE 2.2: A plot used to determine a parametrization for the momentum width from both target and projectile fragmentation residues.

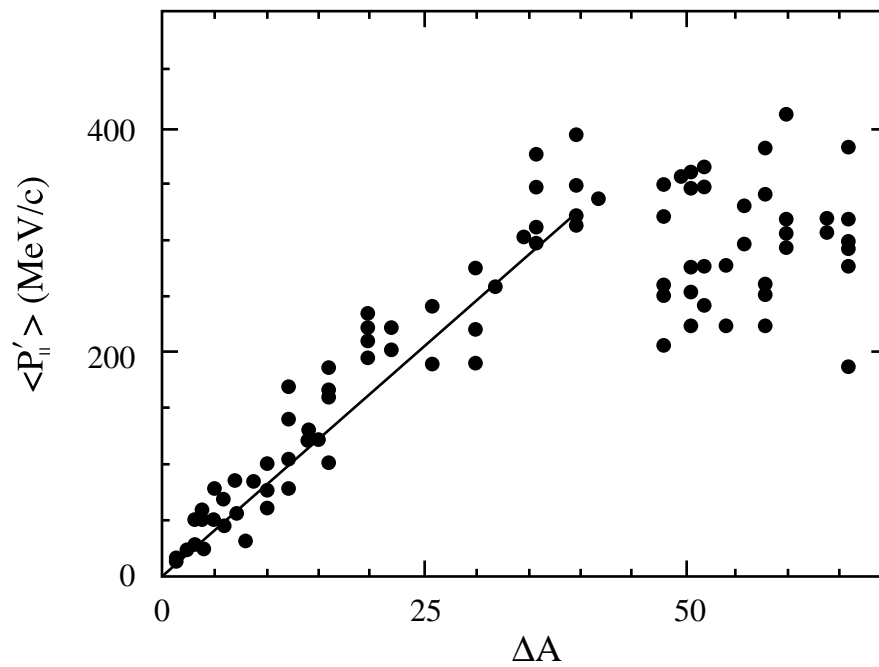


FIGURE 2.3: The plot used to determine the parametrization for the momentum shift that fragments undergo during both target and projectile fragmentation.

in different rest frames. Morrissey considered three different mechanisms for the production of both target and projectile residue and showed (using conservation of momentum) that the momentum width could be written as

$$\sigma_{\parallel} = \sigma_o \cdot \sqrt{\Delta A} \quad (2.1)$$

where $\Delta A = A_{\text{initial}} - A_{\text{observed}}$, σ_o is a constant, and the parallel momentum width is given by σ_{\parallel} . Figure 2.2 shows a fit using a variation of Eq. 2.1 (where $P_{\text{rms}} = \sqrt{3} \cdot \sigma_{\parallel}$) to a collection of high energy data (both projectile and target fragmentation) available at that time and it yields a value of $\sigma_o \sim 90 \text{ MeV/c}$ which reproduces the data relatively well.

The longitudinal momentum transfer (for target fragmentation) was presented by Morrissey as

$$\langle P'_{\parallel} \rangle = m_{\text{targ}} \langle \beta_{\parallel} \rangle \beta \gamma / (\gamma + 1) \quad (2.2)$$

where m_{targ} is the mass of the target, $\langle \beta_{\parallel} \rangle$ is the average velocity along the beam axis, and the kinematic factor of $\beta \gamma / (\gamma + 1)$ depends only on the initial velocity of the beam. Morrissey made the assumption that the mass of the primary residue is approximately equal to the mass of the target (for target fragmentation). Figure 2.3 shows the longitudinal momentum transfer plotted against the mass loss ($\Delta A = A_{\text{initial}} - A_{\text{observed}}$) for several sets of data which were available at the time (both target and projectile fragmentation) and for the relatively low ΔA values (where Eq. 2.2 would be applicable) a direct linear relationship was observed where

$$\frac{\langle P'_{\parallel} \rangle}{\Delta A} \sim 8 \text{ MeV/c/u}. \quad (2.3)$$

The slope of 8 MeV/c/u did a relatively good job reproducing the data available at the time.

Using the parametrizations in Eq. 2.1 and Eq. 2.2, the momentum width and transfer for the residue from high energy fragmentation reactions could be predicted relatively well which leaves one important observable in need of a parametrization – the cross section. One year after the publication by Morrissey, Sümmerer *et al.* [sum90] published a paper in which over 700 experimental fragment cross sections available at that time were analyzed – from both target and projectile fragmentation. The goal of the paper was to determine an analytical form (often referred to as the EPAX parametrization) which could predict the yield for any target/projectile reaction at high energy, and Sümmerer points out that several parametrizations published at the time did not achieve that goal.

The cross section parametrization for a particular A and Z can be written as follows:

$$\sigma(A,Z) = Y(A) n \exp(-R|Z_{\beta} + \Delta + \Delta_m - Z|^U) \quad (2.4)$$

where the first term represents a mass yield (the sum of the isobaric cross sections with mass A), the n term is for normalization, and the exponential term represents the distribution of elemental cross sections with a given mass around the maximum (Z_p). The width of the charge dispersion is controlled by the width parameter, R, and the exponent U. The two Δ terms represent a shift in the peak of the charge dispersion due to the N/Z ratio of the projectile during projectile fragmentation or the target during target fragmentation. The various terms are then broken down further to the point at which the cross section is only a function of the mass of the target and projectile, and the mass and charge of the isotope of interest. (Note that this is not dependent upon the energy of the reaction since it was developed for high energy fragmentation.) The following breakdown of the terms from Eq. 2.4 was developed by Sümmerer *et al.* by analyzing the data that

was available at the time and fitting the results with applicable functions. Over 85% of the data present at the time could be reproduced within a factor of two using this parametrization.

The $Y(A)$ term is given as

$$Y(A) = \sigma_R P(A_t) \exp[-P(A_t)(A_t - A)] \quad (2.5)$$

where A_t is the mass of the target, A is the mass of the observed isotope, $P(A_t)$ is formulated as

$$\ln P(A_t) = -7.57 \times 10^{-3} A_t - 2.548, \quad (2.6)$$

and the total reaction cross section term of σ_R is written as

$$\sigma_R = 450(A_p^{1/3} + A_t^{1/3} - 2.38) \text{ mb} \quad (2.7)$$

where A_p is the mass of the projectile.

The exponential term contains the variables of R , U , and Z_p which are strongly correlated and Sümmerer *et al.* chose to fix the value of U and then determine the best formalism for Z_p and R . The U term was then given simply as

$$U = 2 \text{ for } (Z_p - Z) < 0 \text{ and } U = 1.5 \text{ for } (Z_p - Z) \geq 0 \quad (2.8)$$

where Z_p represents the peak of the charge distribution and can be written as

$$Z_p(A) = Z_\beta(A) + \Delta \quad (2.9)$$

and the right hand side of Eq. 2.9 is given by

$$Z_\beta(A) = \frac{A}{1.98 + 0.0155A^{2/3}} \quad (2.10)$$

and

$$\Delta = \begin{cases} 2.041 \times 10^{-4} \cdot A^2 & \text{if } A < 66 \\ 2.703 \times 10^{-2} \cdot A - 0.895 & \text{if } A \geq 66. \end{cases} \quad (2.11)$$

The width parameter of R is given as

$$\ln R(A) = -6.770 \times 10^{-3} A + 0.778 \quad (2.12)$$

and it is pointed out that this variable can have a dramatic effect on the rates predicted for exotic isotopes on the wings of the isotopic distributions. The normalization term n is then given as:

$$n = \sqrt{\frac{R}{\pi}}. \quad (2.13)$$

The final term from Eq. 2.4, that has not yet been discussed, is the Δ_m or “memory effect” term which was introduced by Sümmerer *et al.* to explain the “shift” in the charge dispersion curve that occurs due to different N/Z ratios in the projectile during projectile fragmentation or the target during target fragmentation. The majority of data that was analyzed by Sümmerer consisted of target fragmentation where the N/Z ratio of the targets was generally close to the valley of β stability, and experiments with targets (or projectiles) far from the valley of stability did not occur until recently. Sümmerer used very limited data to obtain a formalism for the memory effect, and those data are shown in Figure 2.4. The neutron-rich data was obtained by Westfall *et al.* [wes79] and involved the projectile fragmentation of $^{48}\text{Ca} + ^9\text{Be}$ at 212 MeV/nucleon, and the proton-rich data implemented target fragmentation with the reactions of $p + ^{96}\text{Ru}$ and $p + ^{96}\text{Mo}$ at 1.8 GeV [por64]. As can clearly be seen in Figure 2.4, the proton-rich data are extremely limited and the neutron-rich data are “one-sided” and the value of Z_p (needed in Eq. 2.8) could not be directly determined from the data. The parametrization for Δ_m from the limited data is shown in Figure 2.5 by the solid curves (the hollow data points are the result of a calculation - not actual data) and was described as

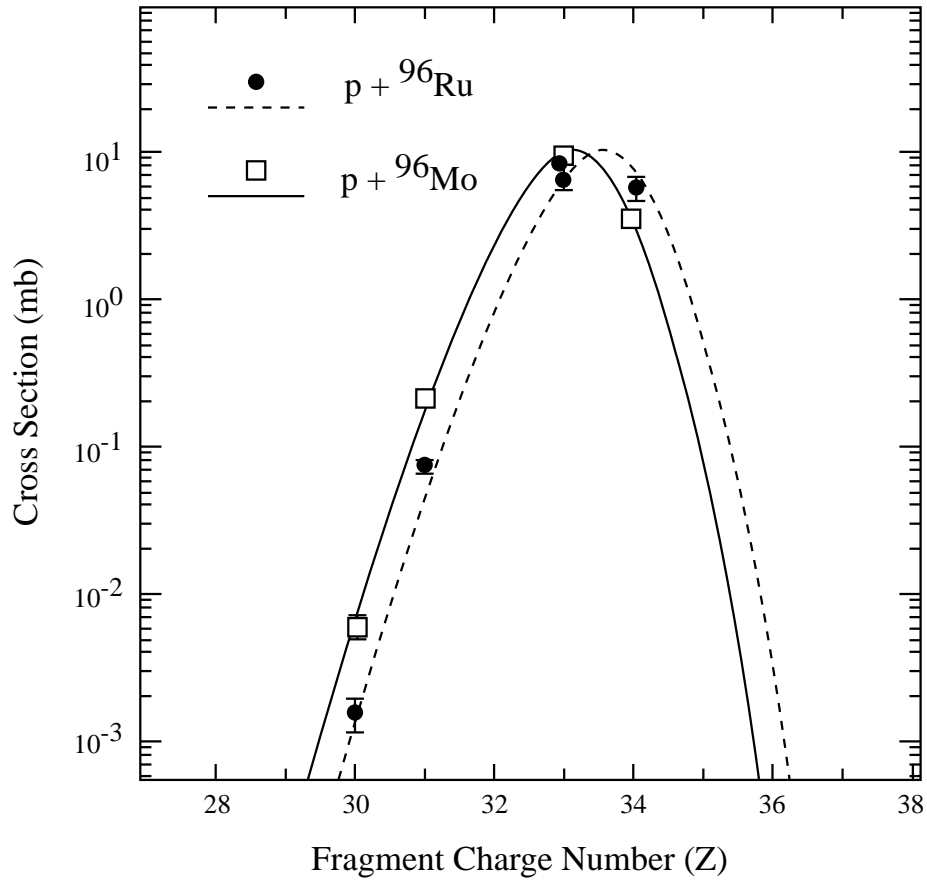
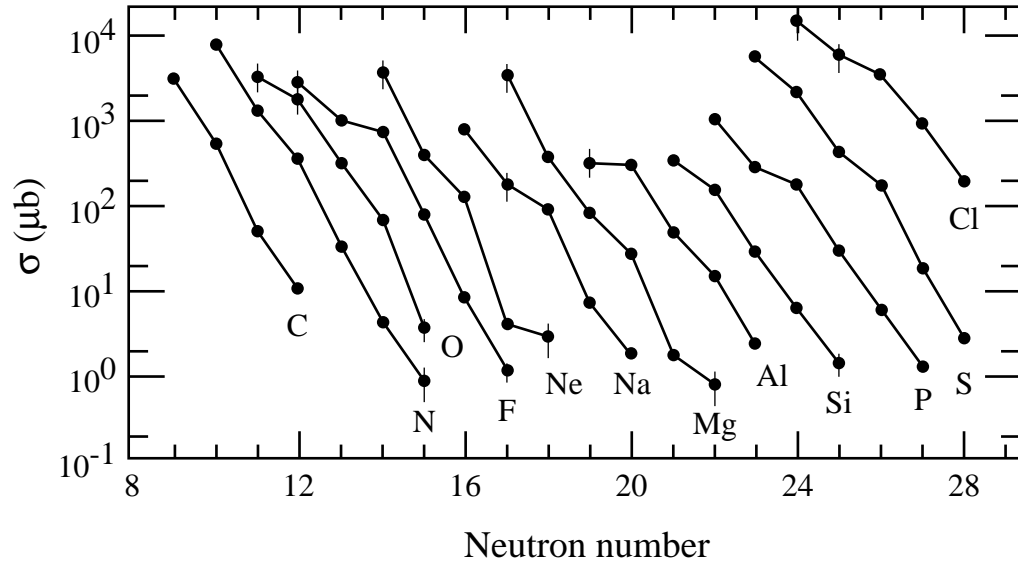


FIGURE 2.4: The experimental data originally used for the parametrization of the memory effect.

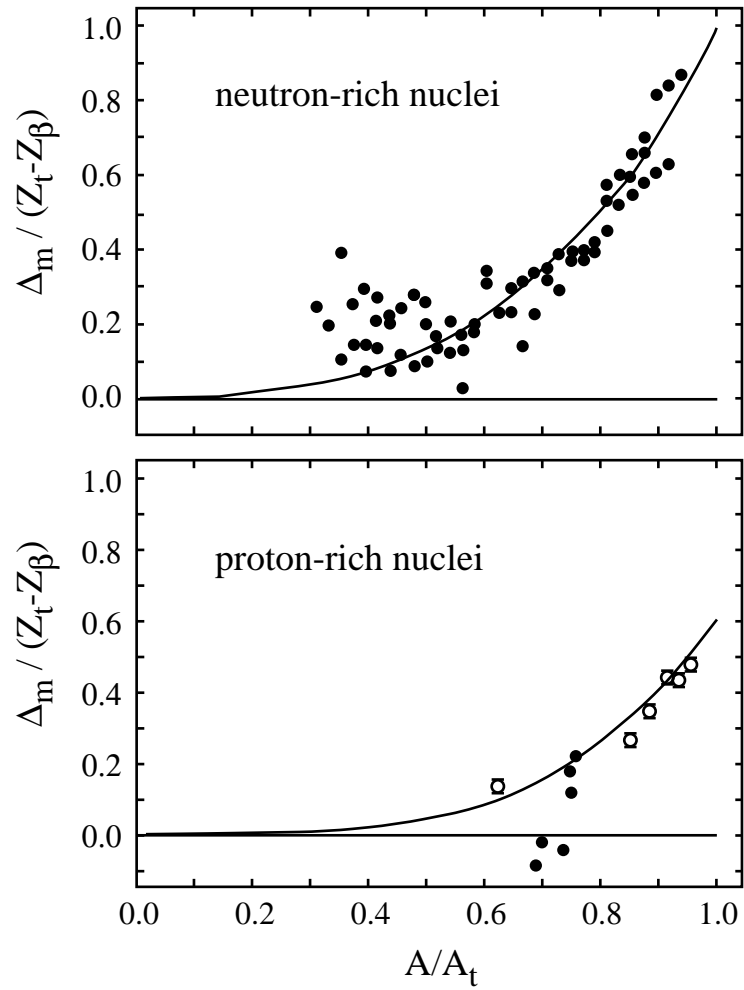


FIGURE 2.5: Parametrization of the “memory effect” from Eq. 2.14. The data used for this parametrization are shown in Figure 2.4.

$$\Delta_m(A) = \left[c_1 \left(\frac{A}{A_t} \right)^2 + c_2 \left(\frac{A}{A_t} \right)^4 \right] \Delta_\beta(A_t) \quad (2.14)$$

where A_t is the target mass and $\Delta_\beta(A_t) = Z_t - Z_\beta(A_t)$, in which Z_t is the target proton number, and A_t is the target mass. Different values for the coefficients c_1 and c_2 were determined for neutron- and proton-rich fragmentation and are given by

$$\begin{array}{llll} c_1 = 0.4 & \text{and} & c_2 = 0.6 & \text{for neutron-rich nuclei} \\ c_1 = 0.0 & \text{and} & c_2 = 0.6 & \text{for proton-rich nuclei} \end{array} \quad (2.15)$$

and the solid curves in Figure 2.5 use these values.

2.2 ISApac Model

The basic idea behind all intranuclear cascade models is that high energy heavy-ion reactions can be described as a sequence of independent nucleon-nucleon (N-N) collisions between the constituents of the projectile and the target nucleus. Collisions between the individual nucleons are treated as collisions between classical particles. In other words: the colliding nucleons are not treated as a quantum mechanical system; rather one assumes that the spacial coordinates and momentum of the nucleons is known, and therefore their trajectories. All calculations in the code are performed using relativistic kinematics, but, as was described above, the nucleons are treated in a classical sense. The only quantum mechanical effect that is taken into account is Pauli-blocking. Describing the colliding nuclei as a classical system can of course only be justified within certain boundaries. The mean free path (λ) between two subsequent nucleon-nucleon collisions must be large relative to the range of the nuclear force (R), otherwise this effect on the reaction dynamics must be taken into account. Assuming that the nuclear force is established via the exchange of virtual mesons, a rough estimate of the range of the nuclear force can be determined. The pion is the exchange particle responsible for the long

range part of the nuclear force. Using the mass of the pion and the $\Delta E \cdot \Delta t$ uncertainty relationship, we can estimate the mean lifetime of the virtual pion from

$$\Delta t \cdot m_{\pi} c^2 \sim \hbar, \quad (2.16)$$

where m_{π} is the rest mass of a pion, c is the speed of light, and \hbar is the reduced Planck's constant. The range of the nuclear force can now be estimated by assuming that the pion can not be propagating faster than the speed of light between its emission and absorption. This leads to the determination of the range where:

$$R = c \cdot \Delta t \approx \frac{\hbar}{m_{\pi} c} \quad (2.17)$$

and the limiting condition placed on the mean free path becomes

$$\lambda \gg R \approx \frac{\hbar}{m_{\pi} c} \sim 1.5 \text{ fm} . \quad (2.18)$$

Another basic concept which stands behind all INC models is that the mean free path between two subsequent collisions must be large relative to the de Broglie wavelength of the colliding nucleons. This condition insures that the wave function of the colliding nucleons is already in its asymptotic form before the next collision occurs and enables one to neglect possible interference effects between subsequent collisions, as well as the possibility of simultaneous collisions between more than two nucleons. The condition we need to fulfill can be written as:

$$\lambda \gg \frac{\hbar}{p} \sim 3.4 \text{ fm} \quad (2.19)$$

where the projectile momentum of the present work was used.

To check if the two conditions placed on the mean free path are actually met in heavy ion reactions, we need to get an estimate of the mean free path of nucleons inside

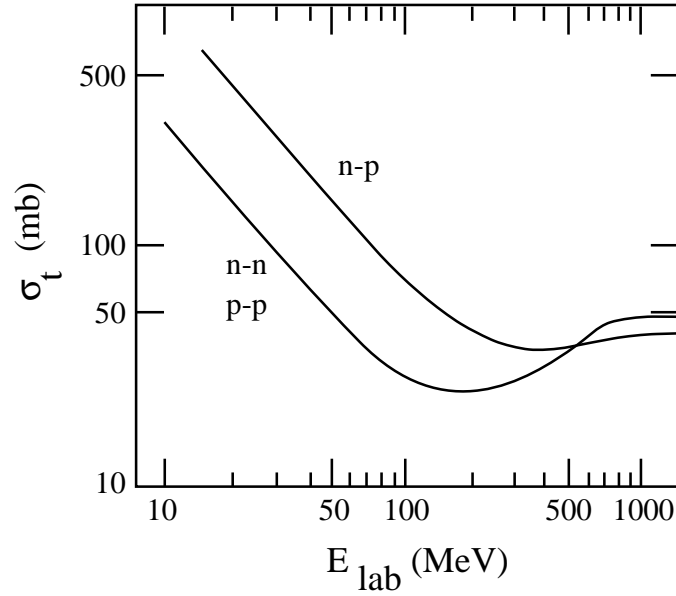


FIGURE 2.6: Nucleon-nucleon cross sections as a function of incident energy.

nuclear matter. In the following, effects related to being in the nuclear medium will be neglected, e.g. the reduction of the nucleon mass due to its binding inside the nucleus. The experimentally known total reaction cross sections (σ) for collisions between unbound nucleons from neutron-proton (n-p) and proton-proton (p-p) collisions can be combined with the nuclear density (ρ) to make an estimate of the mean free path:

$$\lambda = \frac{1}{\rho \sigma_{n,p}} \sim 1.7 \text{ fm.} \quad (2.20)$$

For the above estimate of the mean free path of nucleons inside nuclear matter the saturation value of the nucleon-nucleon cross section of about 40 mb was used along with a constant nuclear density of 0.15 fm^{-3} . From this crude estimate it is obvious that the condition stated in Eq. 2.18 and Eq. 2.19, namely that the mean free path has to be much larger than the range of the nuclear force and the de Broglie wavelength, are not exactly met, and in fact they are actually of the same order of magnitude.

It is also important to look at the total N-N cross section as a function of incident energy, and its influence on the mean free path of the nucleons. As can be seen in Figure 2.6 [che68] the nucleon-nucleon cross section gets very large for low incident energies. This behavior can be explained via the dominating pure s-wave scattering in this energy regime. From Eq. 2.20 we can see that the mean free path gets very short and quickly becomes smaller than the nuclear range. Therefore, one has to be very careful when using INC models for incident energies below 100 MeV/nucleon. However, since the present research is primarily interested in peripheral collisions leading to projectile-like fragments, nature is on our side. The diffuseness of the nuclear surface leads to a decrease in the nuclear density for peripheral reactions, thus increasing the mean free path of the nucleons. This behavior offsets, at least in part, the increase in the total N-N cross section at low incident energies. Figure 2.7 shows two approximations for the nuclear density of the nucleus ^{86}Kr . The constant density distribution shown in Figure 2.7 uses the so called “folded Yukawa sharp cut-off” density distribution [kra76] (where $R=r_0A^{1/3}$ and a value of $r_0=1.18$ fm is used) while the INC code ISABEL [yar79] approximates this with 16 steps of constant densities. The agreement is good over the entire distribution.

As was mentioned earlier, INC models treat the projectile and target nucleus as an ensemble of ‘free’ nucleons in which the nucleons undergo independent collisions during a heavy ion reaction. It should be pointed out one more time, that the majority of INC codes (including the ISABEL code used for the present work) use the free nucleon masses and differential cross sections known from reactions between free nucleons to simulate the heavy ion reaction. The calculations take the energy dependence of the N-N cross sections into account as was shown in Figure 2.6. The angular distribution of the particles after the

collisions is determined by using the experimentally known differential cross sections at the given energy. The azimuth angle is chosen randomly.

In principle, since the nuclear force is charge independent, one does not have to distinguish between n-n and p-p collisions (after correcting for Coulomb effects), however, the n-p (p-n) collisions must be treated separately. As is clearly shown in Figure 2.6, the total reaction cross section for n-p (p-n) reactions at low energies is significantly higher than the one for n-n (p-p). This effect can be explained by looking at the relevant exchange particles for each type of collision. For the n-n (p-p) scattering neutral pions (π^0) are the only allowed exchange particles, whereas for the scattering of non-identical particles (n-p, p-n) the charged pions (π^+ , π^-) are also allowed exchange particles along with the π^0 's, leading to three allowed exchange particles. The strength of the interaction has to be weighed according to the number of exchange particles.

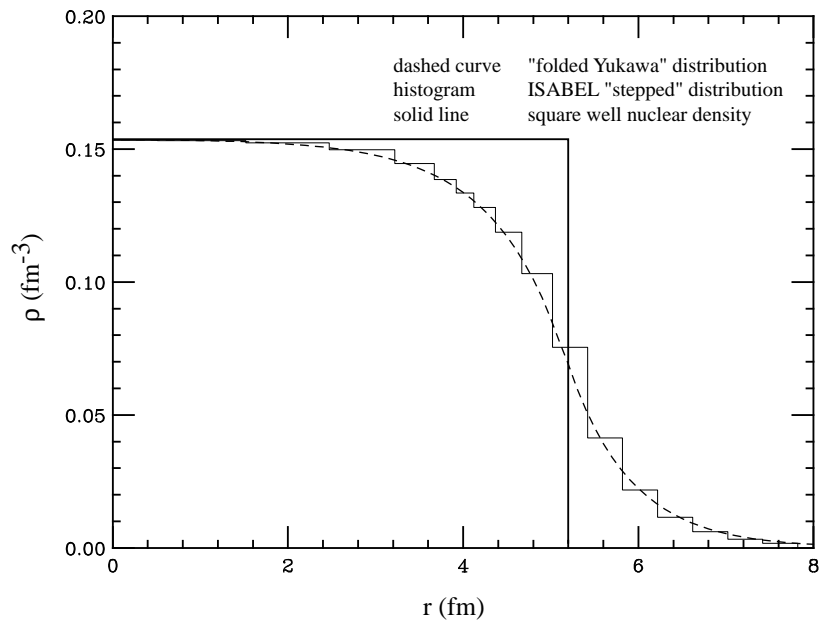
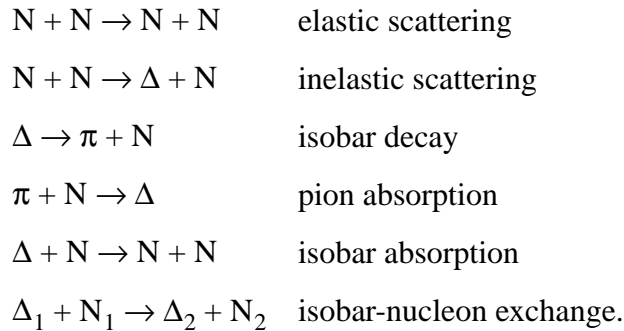


FIGURE 2.7: Nuclear density for ^{86}Kr from the ISABEL code, a Yukawa distribution and a square well density distribution.

The ISABEL code used for this work takes the following six collisions into account:



As was previously mentioned, the cross sections for the first two types of collisions are taken from experimental systematics, and the cross section for the isobar absorption and isobar-nucleon exchange are taken to be the same as the elastic scattering. The cross section for the isobar decay is obtained by detailed balance [ber88].

Another important variable that needs to be determined by the INC code is the excitation energy of the prefragments. It should be noted here that the ISABEL code with the option of a uniform Fermi gas distribution was used for the present work, and it has been shown [fau92a] that this leads to the best reproduction of experimental data. The excitation energy is determined from the energies of ‘holes’ created in the Fermi sea during the collision and the energies of particles which are captured by the nuclear potential. Particles with an energy below a certain “cutoff” energy are considered captured (or trapped) by the nuclear potential. This cutoff energy is isospin dependent and is determined as follows: 1) for neutrons the sum of the Fermi energy and twice the neutron binding energy and 2) for protons it is given by the maximum value of either the sum of the Fermi energy and twice the proton binding energy or the sum of the Fermi energy, the proton binding energy and the Coulomb energy. Figure 2.8 shows a simplified view of the energy diagram for clarification.

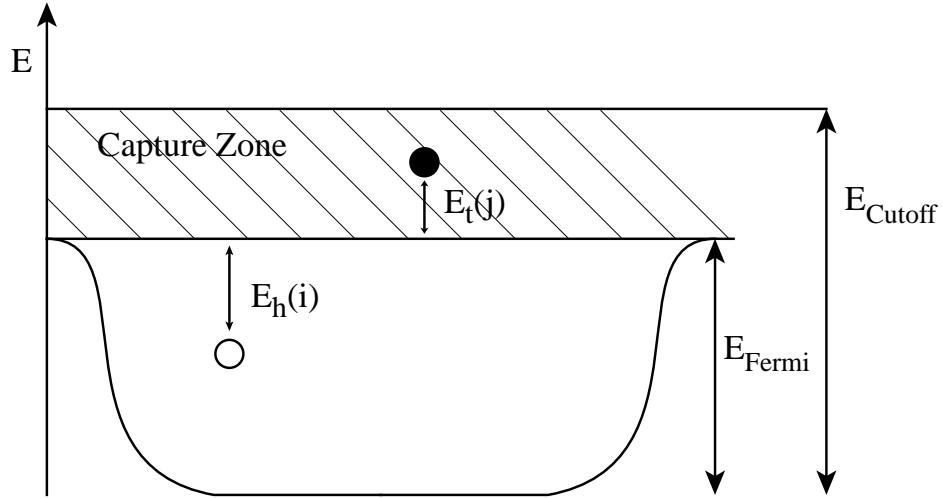


FIGURE 2.8: Simple view of the energy diagram used to determine created holes, captured particles, and free particles in the ISABEL code.

All nucleons will be “tracked” by the ISABEL code as long as they are inside the overlap volume of the two colliding nuclei, independent of their energy. Nucleons outside of the overlap volume will only be tracked until a) their energy drops below the cutoff energy – in which case they are considered captured, or b) they leave the projectile or target volume, and they are then considered free particles. For details of these processes please refer to [che68]. The excitation energy is therefore given by:

$$E^* = \sum_i^{\text{holes}} E_h(i) + \sum_j^{\text{trapped}} E_t(j) \quad (2.21)$$

and the linear momentum of the prefragments is similarly given by the sum over the Fermi momentum of the holes created in the Fermi sea and the sum of the momenta of the captured particles:

$$\bar{P} = \sum_i^{\text{holes}} \bar{p}_h(i) + \sum_j^{\text{trapped}} \bar{p}_t(j). \quad (2.22)$$

We have now discussed the first step of the heavy ion reaction, which is simulated via an INC code, leading to so called prefragments. These prefragments are characterized by their mass, charge, excitation energy, as well as their linear and angular momentum. Since the prefragments are highly excited, they are far away from their ground state and have rather short lifetimes. The prefragments reduce their excitation energy via the evaporation of neutrons, protons, alphas, and sometimes even more complex clusters of nucleons, fission processes, as well as via the emission of γ -rays. To simulate these processes, one usually uses so called statistical evaporation codes. These codes have been successfully used to describe compound-nucleus systems, produced in fusion-evaporation reactions close to the Coulomb barrier, and since the nuclear excitation energies involved in fusion-evaporation reactions are of the same order of magnitude as the prefragments produced in peripheral heavy ion collisions, this seems to be a reasonable step. However, this assumption can only be justified if the produced prefragments reach a statistical equilibrium before they decay. Comparison of the de-excitation calculations to experimental data [gav80] seems to prove that this assumption is fulfilled.

The basic concept of the statistical evaporation codes goes back to an idea of Niels Bohr from 1936 [boh36]. It assumes, that the de-excitation of the excited nucleus depends on the statistical weight of all possible (allowed) decay channels and their transmission probability. The entrance channel, or in other words “how the system became excited,” does not matter. This of course implies that the system has reached a thermal equilibrium before it decays — which can lead to problems if one wishes to use statistical models for extremely high excited systems which are produced in violent central collisions. In this situation, the lifetime of the system might become too short to equilibriate all inner

degrees of freedom. Another basic assumption of the statistical model is that of the sequential decay. It assumes, that if more than one decay occurs, they happen one after the other. It's also assumed that the decaying nucleus has enough time between the sequential decays to reach thermal equilibrium again. For the calculations performed in the present work, the well established and widely used code PACE by Gavron [gav80] was utilized.

2.3 Recent Research

The intermediate energy regime is generally considered to range from 20 MeV/nucleon to 200 MeV/nucleon, and the results from two experiments performed with krypton projectiles near the opposite ends of that energy regime were recently published. These experiments showed that different reaction processes are occurring at the two ends of the intermediate energy regime, which is not unexpected since a transition must occur between the low and high energy regimes. An experiment performed by Stéphan *et al.* [ste91] at 200 MeV/nucleon led to results similar to those obtained in high energy fragmentation. Bazin *et al.* [baz90] performed an experiment at 44 MeV/nucleon which had significantly different results and seemed to indicate that the primary mechanism involved at that energy was deep inelastic transfer and not (high energy) fragmentation. A third experiment involving krypton fragmentation at 500 MeV/nucleon was later carried out by Weber *et al.* [web94] in an effort to understand the energy at which the transition to true fragmentation is taking place. Recent experiments involving krypton fragmentation were also performed in an effort to explore the rp-process.

The “specific” experiments [moh91, bla95] did not involve systematic studies of the cross sections, momentum distributions, and momentum transfer, but they closely studied the fragmentation products near the proton drip-line. Some of the results and

conclusions from the systematic measurements, along with the rp-process related work will be presented here in order to provide some background which will be helpful for understanding the motivation for the present research.

2.3.1 Krypton Fragmentation at 44 MeV/nucleon

D. Bazin *et al.* [baz90] performed an experiment which involved a primary beam of ^{84}Kr at 44 MeV/nucleon impinging on several targets (^{27}Al , ^{103}Rh , ^{197}Au) using the GANIL facility. The data provided a mapping of the isotopic yields and momentum distributions from the three different targets and covered a wide range of masses and elements ($6 \leq Z \leq 38$). Typical momentum distributions from this experiment are shown in Figure 2.9. The arrow indicates the momentum per nucleon of the beam, and as expected the momentum distribution of the observed fragment falls slightly below this level, however, it should be pointed out that several of the distributions of the low Z fragments from the $^{84}\text{Kr} + ^{27}\text{Al}$ reaction showed a two-peak structure in which one peak was located at a velocity greater than the projectile velocity, while the other was well below that value. This effect is shown in Figure 2.10. The two-peak structure is indicative of forward and backward emission of light fragments in an asymmetric fission like process – which certainly is not present during high energy fragmentation. The cross sections resulting from the fragmentation at 44 MeV/nucleon are shown in Figure 2.11, and the author points out several features that are evident in the figure which show that two reaction mechanisms are contributing to isotopic yield: 1) There is a noticeable contribution of yield near the N/Z of the projectile which is significantly different for the various targets that were used, and 2) a large contribution of yield is far from the N/Z ratio of the projectile and falls closer to the valley of β -stability. The later seems to indicate that highly

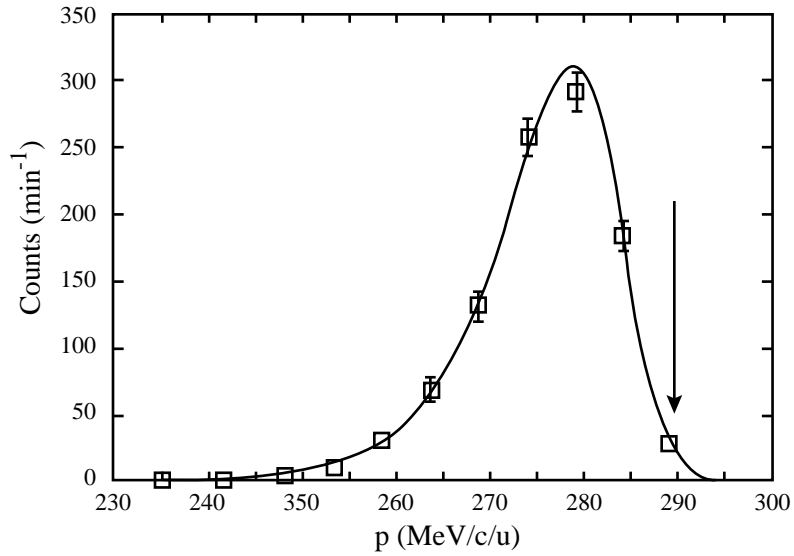


FIGURE 2.9: The momentum distribution for $^{72}\text{Ge}^{31+}$ from the fragmentation of $^{84}\text{Kr} + ^{27}\text{Al}$ at 44 MeV/nucleon.

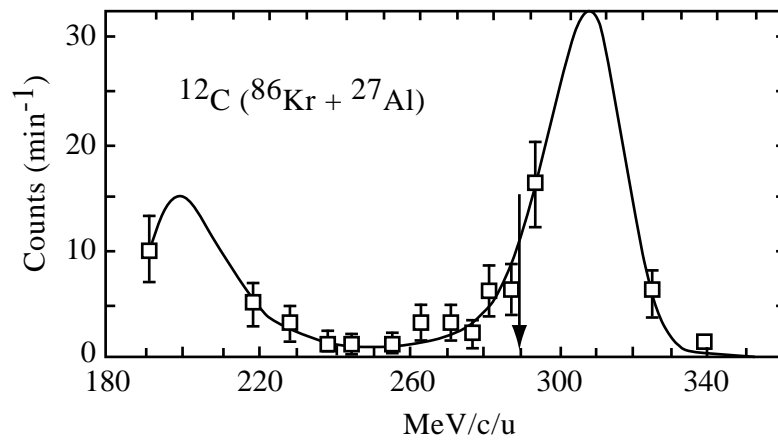


FIGURE 2.10: The two-peak structure observed for several momentum distributions from the reaction $^{86}\text{Kr} + ^{27}\text{Al}$ at 44 MeV/nucleon.

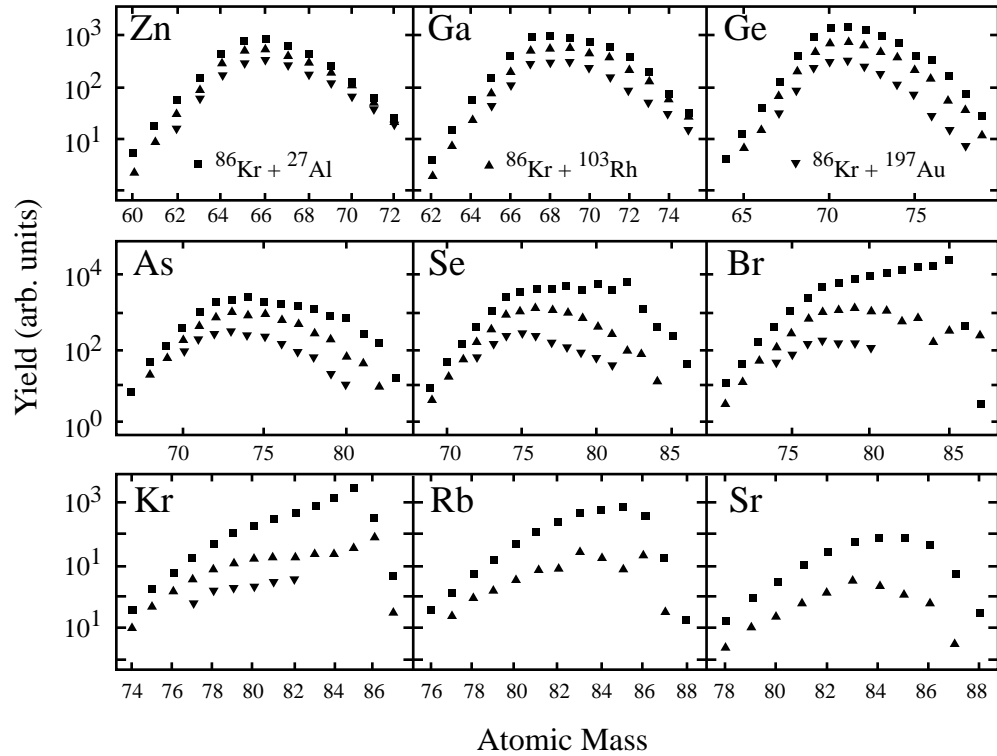


FIGURE 2.11: Cross sections resulting from $^{84}\text{Kr} + ^{27}\text{Al}$, ^{103}Rh , ^{197}Au at 44 MeV/nucleon.

excited prefragments are responsible for the production of the observed fragments, while the difference caused by altering the targets seemed to indicate that an incomplete fusion process was the primary reaction mechanism (as had been previously described in work involving 22 MeV/nucleon $^{84}\text{Kr} + ^{197}\text{Au}$, ^{108}Ag [luc87]). The experimental cross sections for $Z=10$, 20 , and 30 are shown in Figure 2.12 and are compared with theoretical values from a high energy model that was often used at that time (see [baz90] for complete details). It is quite apparent that the code used could not reliably predict the experimental results.

Although it was not mentioned in the published article, one can use the typical momentum distribution that was shown in Figure 2.9 to get an estimate of the longitudinal

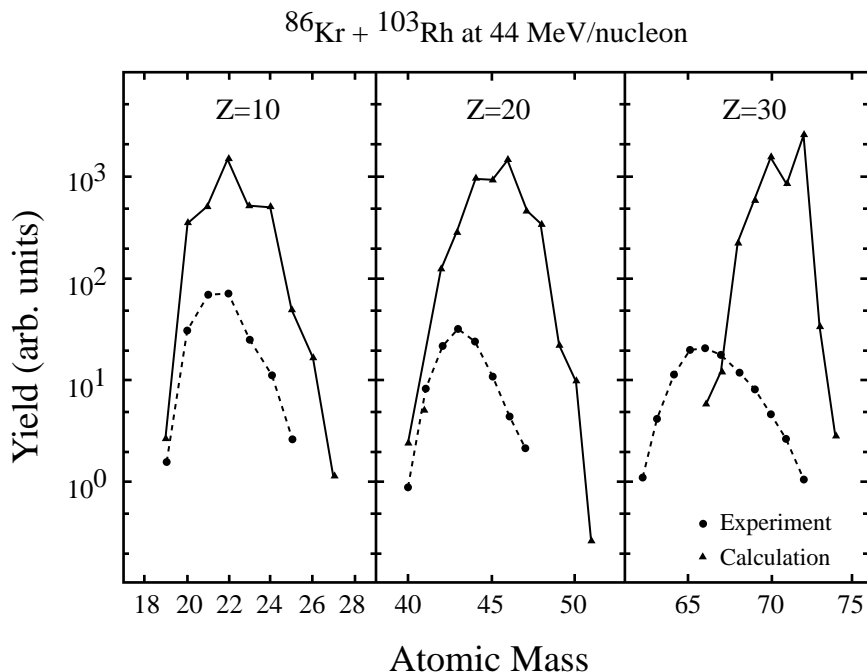


FIGURE 2.12: Selected yields from 44 MeV/nucleon krypton fragmentation along with corresponding predictions from a high energy fragmentation model.

momentum width (referred to as σ_0 , see discussion of the Goldhaber model in Chapter 4 for further details). The value of $\sigma_0 \sim 95$ MeV/c is typically found from high energy fragmentation, but the data at 44 MeV/nucleon yield a value of $\sigma_0 \sim 130$ MeV/c which is significantly larger than expected.

The cross sections and momentum distributions observed during fragmentation at 44 MeV/nucleon showed drastic differences from the predictions of codes used to describe high energy fragmentation at that time. The author concluded that no real fragmentation occurred at this energy and that the transition to “pure” fragmentation needed to be explored in an effort to reliably predict the cross sections of exotic nuclei and pointed out that an experiment would shortly be performed at 200 MeV/nucleon.

2.3.2 Krypton Fragmentation at 200 MeV/nucleon

An experiment by Stéphan *et al.* [ste91] measured the isotopic cross sections and velocity distributions for the fragmentation products from $^{84}\text{Kr} + ^{197}\text{Au}$ at 200 MeV/nucleon. A wide variety of isotopes ranging from $Z=11$ to $Z=37$ was measured at 0.6° and 1.5° . This energy is considered to be at the lower edge of the high energy regime, and the data was expected to exhibit the typical properties of high energy fragmentation.

The experimentally measured cross sections are shown as a contour plot in Figure 2.13 along with predicted “ridge lines” that were obtained through the use of a) a participant spectator model [gos77] (see [ste91] for the details), and b) an INC model. In

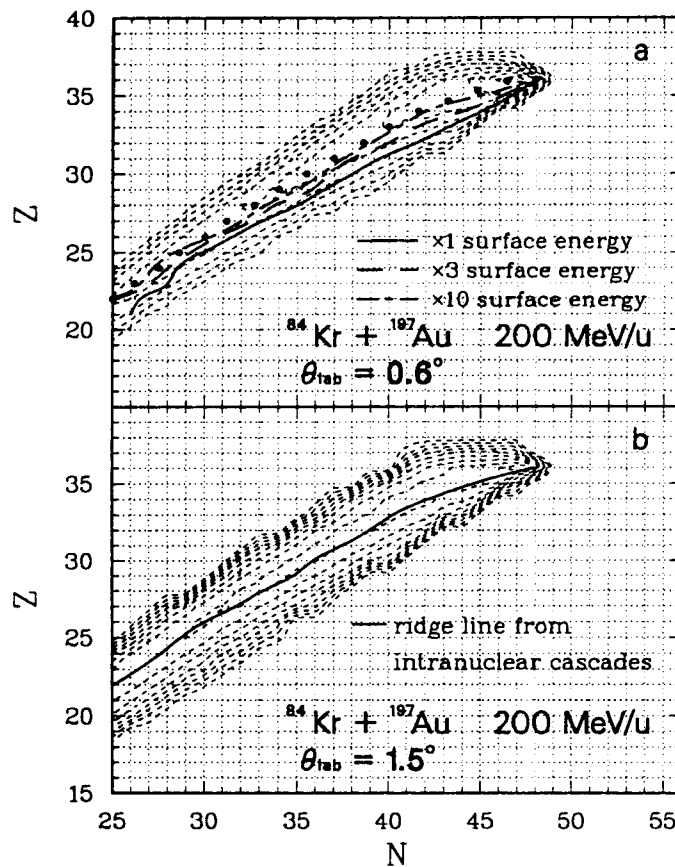


FIGURE 2.13: Cross sections from krypton fragmentation at 200 MeV/nucleon.

order to reproduce the experimental cross sections with the participant-spectator model the value of the prefragment excitation energy had to be drastically increased (by a factor of 10) to have the theoretical ridge line approximate the ridge line of the experimental data. This clearly indicated that the prefragments had a much greater excitation energy than had previously been assumed during high energy target fragmentation (from which most models had been developed). A large portion of the previous research had been target fragmentation or had been performed with either light ($A < 40$) or heavy ($A > 100$) projectiles, and it was becoming apparent that intermediate energy/intermediate mass fragmentation could not be easily understood with the current models. The increased excitation energy was discussed in a previous work [oli79], and a frictional interaction was added to the standard surface energy term which had been used with the clean cut abrasion-ablation model. Stéphan points out that this frictional term could not account for the tenfold increase in prefragment excitation energy.

The INC based model (in this case Stéphan used the ISABEL INC code followed by a deexcitation code called LOTO [got91]) did a relatively good job reproducing the ridge line of the experimental data, and the INC code did predict relatively high excitation energies for the prefragments. However, although the difference is small, it can be seen in Figure 2.13 that the experimental distribution is slightly shifted to the proton-rich side of the predicted values near the mass of the projectile and then shifts to the neutron-rich side of the predictions for the low Z fragments.

The velocity shift of the fragmentation products is shown in Figure 2.14. Using the formalism of Morrissey (Eq. 2.3) it can be shown that their experimental data closely follows the trend given by $-\langle P_{\parallel}' \rangle \sim 11.7 \text{ MeV}/c \cdot \Delta A$, where the constant value of 11.7

MeV/c is slightly higher than the value of 8 MeV/c which was expected from the systematics of Morrissey. Also shown in Figure 2.14 is the predicted line from the INC code which does follow the general linear trend of the experimental data and although the velocity shift is greater than the theoretical values developed from high energy models, the overall linear trend is well reproduced.

The parallel momentum widths of the fragmentation products are shown in Figure 2.15 along with comparisons to the Goldhaber model (see Chapter 4 for further details) and the INC based model. For the Goldhaber model, the constant value of $\sigma_0 \sim 90$ MeV/c (representative of the longitudinal momentum width) is typically observed during high energy fragmentation, and the 200 MeV/nucleon data resulted in a value of $\sigma_0 \sim 95$ MeV/c, which is comparable to the value from high energy

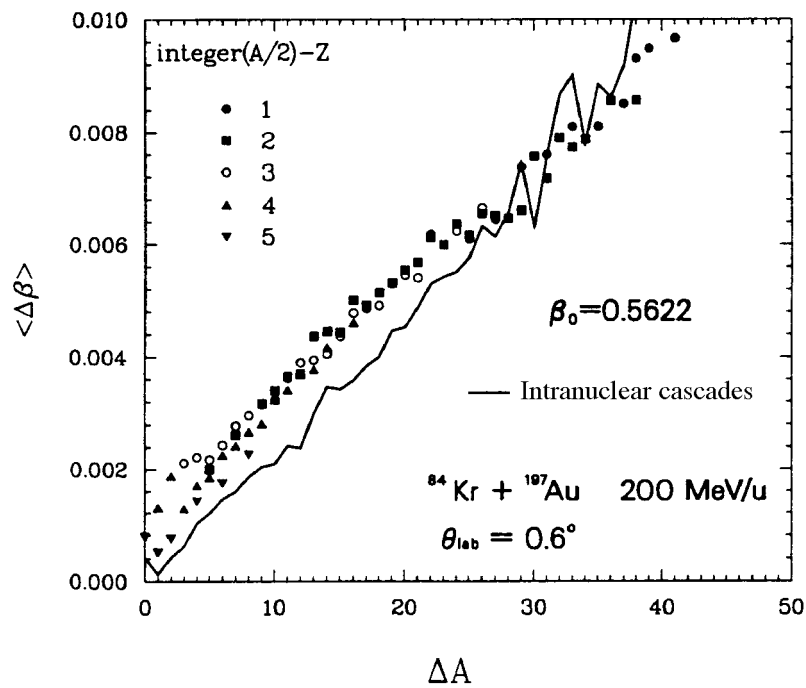


FIGURE 2.14: Velocity shift for the fragmentation products resulting from $^{84}\text{Kr} + ^{197}\text{Au}$ at 200 MeV/nucleon.

fragmentation. In the systematics presented by Morrissey [mor89] it is mentioned that σ_0 should not be sensitive to the reaction mechanism. At low energies, where fragmentation is not the principle reaction mechanism, it has been shown [bor86] that σ_0 decreases as the incident energy decreases, while a wide range of high energy fragmentation data has shown a relatively constant value.

The data consisting of cross sections, momentum shifts, and momentum widths obtained at 200 MeV/nucleon seemed to be fairly representative of high energy fragmentation. The data taken at 200 MeV/nucleon was much closer to true fragmentation compared to the 44 MeV/nucleon data, and it was evident that further exploration of intermediate energy regime was needed in order to gain a greater understanding of the reaction processes occurring during the fragmentation of intermediate mass projectiles.

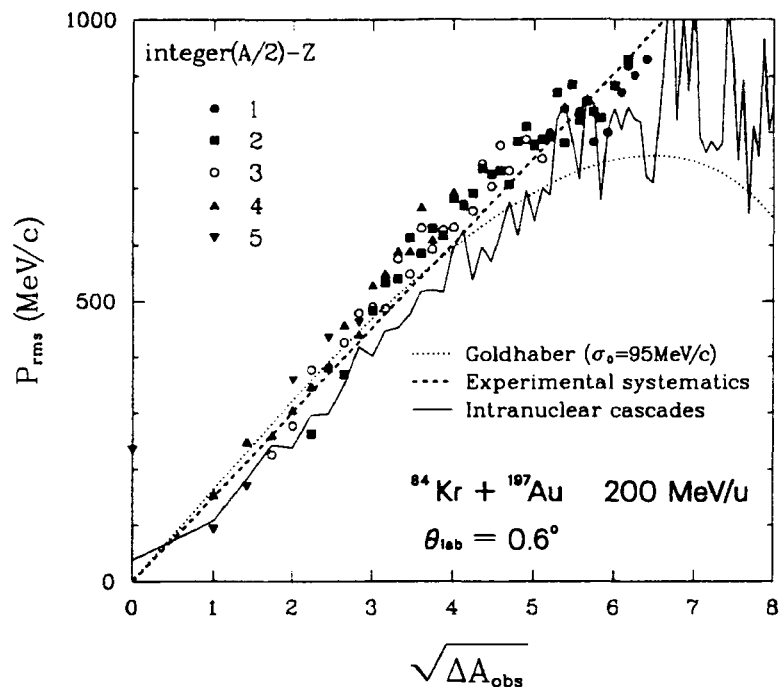


FIGURE 2.15: Parallel momentum widths for the intermediate energy fragmentation products.

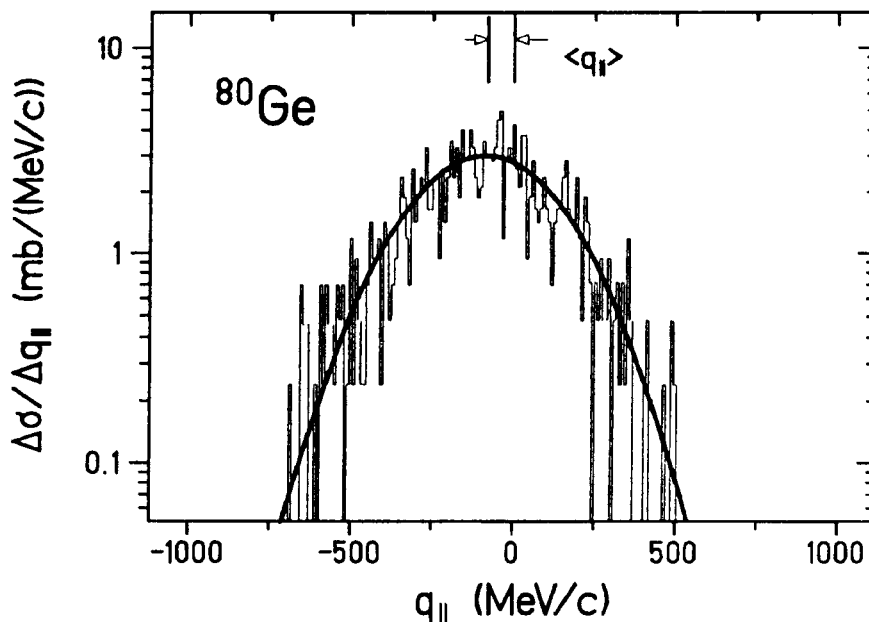


FIGURE 2.16: Typical momentum distribution observed during high energy fragmentation - in this case $^{86}\text{Kr} + ^9\text{Be}$ at 500 MeV/nucleon.

2.3.3 High Energy Krypton Fragmentation

The results from the two intermediate energy fragmentation experiments could not be completely reproduced by the theoretical models. An experiment involving high energy fragmentation of $^{86}\text{Kr} + ^9\text{Be}$, ^{59}Co , ^{181}Ta at 500 MeV/nucleon was performed at GSI by Weber *et al.* [web94]. At this energy it was expected that the EPAX parametrization and the ISApax model could reproduce the experimental data.

Shown in Figure 2.16 is a typical momentum distribution from the $^{86}\text{Kr} + ^9\text{Be}$ fragmentation which is quite Gaussian (the “tail” often seen at low and intermediate energies is not apparent at high energies). Using the momentum distributions the longitudinal momentum widths (σ) were determined. In Figure 2.17 the widths are shown along with the calculated values from the Goldhaber model (solid curve) and the

systematics developed by Morrissey [mor89] (dashed curve). The Goldhaber model seems to overpredict the width for the fragments near the mass of the projectile, while the Morrissey systematics accurately reproduce the experimental data near the projectile, but overpredicts the width of the light fragments. This is explained by two effects: 1) the Goldhaber model predicts the width for the initial reaction fragments (prefragments) rather than the final observed fragments which have undergone evaporation and 2) the Morrissey systematics were developed from target fragmentation with light ions and thus should not be extrapolated for large mass differences between the projectile and observed fragments.

The momentum shifts are shown in Figure 2.18 and the dashed line indicates the Morrissey systematics of $\langle P_{\parallel}' \rangle \sim \text{constant} \cdot \Delta A$, where a constant of 8.8 MeV/c was the best fit (recall that the Morrissey systematics predicted a value of ~ 8 MeV/c). The linear

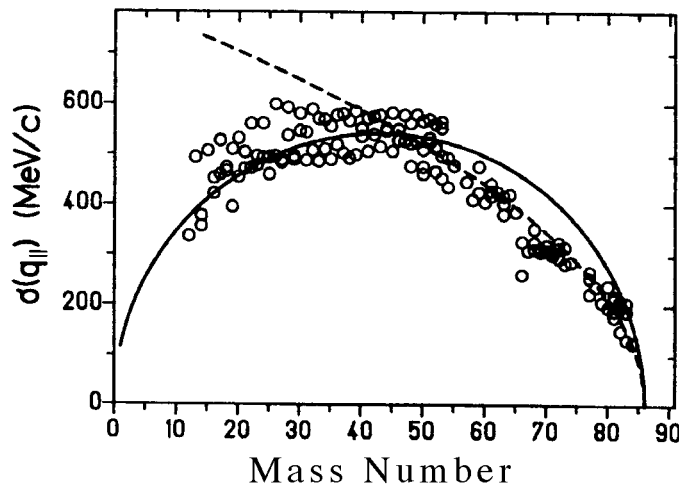


FIGURE 2.17: Parallel momentum widths observed during high energy krypton fragmentation of $^{86}\text{Kr} + ^9\text{Be}$.

relationship corresponds well to the experimental data, but closer investigation of the individual isotopic lines near the Z of the projectile showed significantly different slopes (relative to the 8.8 MeV/c overall trend) ranging from 14 MeV/c for $Z=36$ to 58 MeV/c for $Z=30$. This effect is shown in Figure 2.19 and was not observable for the isotopes with $Z \leq 28$. The author points out that this effect could indicate that the proton-rich fragments are produced in the first step of the fragmentation process and the second evaporation step does not have a large influence on those products — thus the proton-rich isotopes have a small momentum transfer relative to the neutron-rich fragments in the individual isotopic chains.

The cross sections at 500 MeV/nucleon are shown in Figure 2.20 along with the predicted yields from the EPAX parametrization (dot-dash) [sum90], a geometrical abrasion model (dashed) [gai91, sch93], and the ISApac code (histograms) [fau92]. As

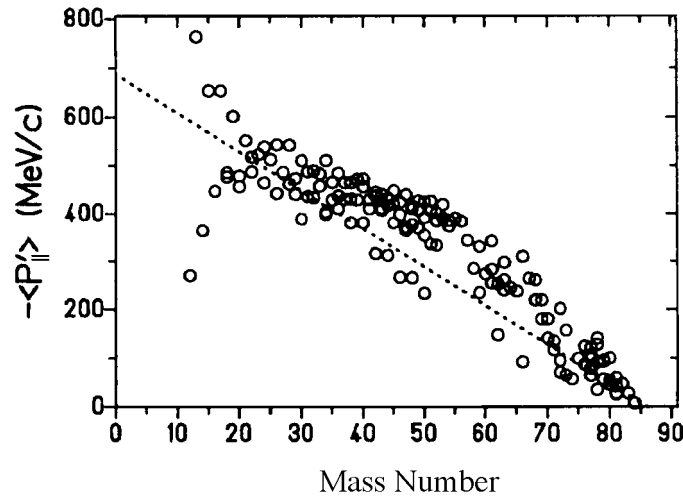


FIGURE 2.18: Momentum shifts observed during the fragmentation of $^{86}\text{Kr} + ^9\text{Be}$ at 500 MeV/nucleon.

was seen in the krypton fragmentation at lower energies, and some recent high energy projectile fragmentation, the theoretical predictions are not a true representation of the experimental data. The EPAX parametrization does not reproduce the ridge line or the width of the isotopic distributions. The abrasion model does a relatively good job of reproducing the data near the mass of the projectile but underpredicts the yield of the proton-rich fragments with $Z < 34$. The excitation energy per abraded nucleon was doubled relative to the original model in an effort to reproduce the data (that is shown in Figure 2.20). The ISApax model does a relatively good job reproducing the data but also underpredicts the yield of proton-rich fragments as did the abrasion model.

It is evident that the models can not yet reproduce recent experimental results with intermediate mass fragmentation, and further data is certainly required so that the models can be modified. However, even without accurate knowledge of the momentum transfer and momentum width, much research on projectile fragmentation has occurred in an effort to explore the rapid-proton capture process.

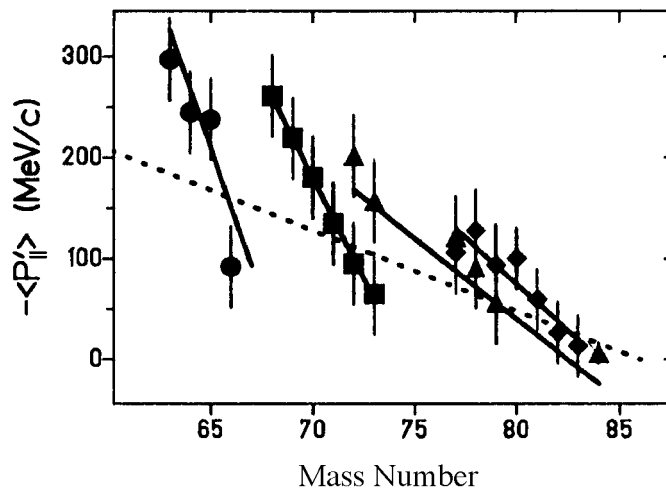


FIGURE 2.19: The momentum shift for the fragments near the mass of the projectile during high energy krypton fragmentation.

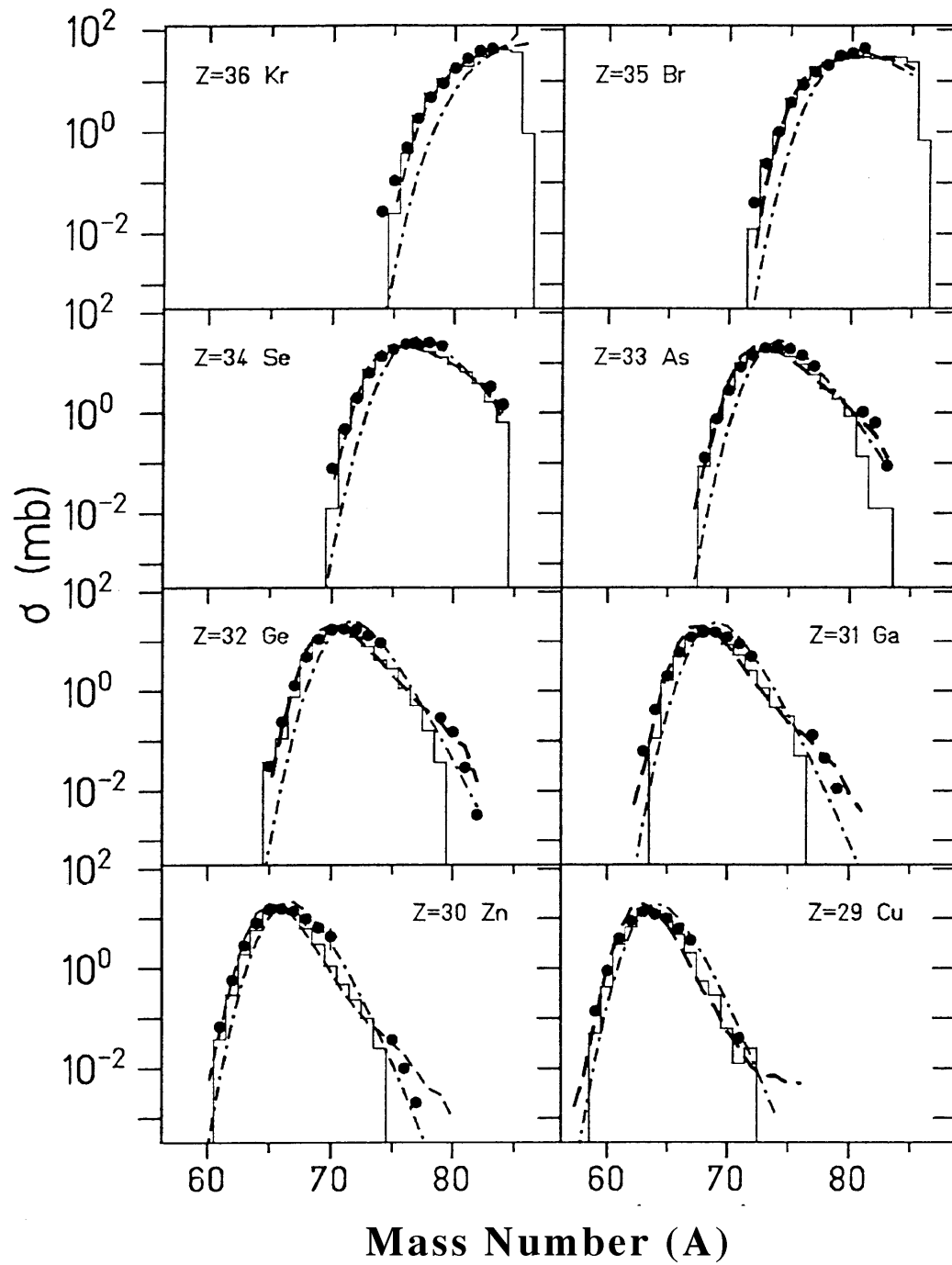


FIGURE 2.20: Cross sections for the reaction products resulting from high energy fragmentation of $^{86}\text{Kr} + ^9\text{Be}$ at 500 MeV/nucleon.

2.3.4 Rapid-Proton Capture Process

The rapid proton capture process (rp-process) was first proposed by Wallace and Woosley [wal81] as an extension to the well studied carbon-nitrogen-oxygen (CNO) and the hot carbon-nitrogen-oxygen (HCNO) processes [cha92, wor94]. These processes are shown diagrammatically in Figure 2.21. During the myriad of astrophysical events (novae, supernovae, x-ray bursts, Thorne-Zytkow objects, etc.) which can occur, a wide variety of temperatures and densities can be present. A large amount of research has been performed (both experimentally and theoretically) to explore the binding energies, half-lives, and reaction cross sections for the isotopes involved in the CNO and HCNO processes. Detailed calculations of the reaction networks for these relatively low temperature and low density processes have been carried out. When the temperature and density increases, the HCNO cycle can break free from its cyclical behavior and begin to increase to higher masses through the key reaction $^{15}\text{O}(\alpha,\gamma)^{19}\text{Ne}(p,\gamma)^{20}\text{Na}$. The path that the rp-process follows (rp-path) from this point onward shows tremendous differences depending on the temperature and density present at the time and the overall burning time of the astrophysical process. Several predicted paths for various burning conditions are shown in Figure 2.22 for which the calculations were carried out for $Z \leq 36$ [wor94].

During conditions of high density and high temperature, a large amount of uncertainty is introduced to the rp-path due to stability and half-life issues pertaining to nuclei on or near the proton drip-line. In this temperature/density regime, the rp-process consists of a sequence of proton captures that occur until the point at which the proton drip line is reached and the nucleus will then β -decay, and the sequence will continue. The rp-process near possible termination points as was proposed by Wallace and Woosley is

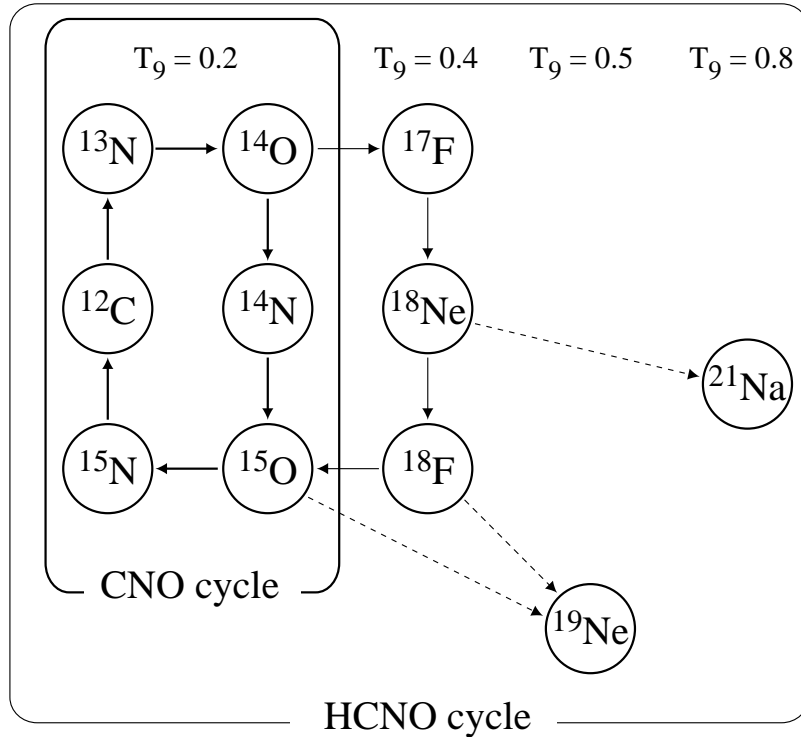


FIGURE 2.21: The CNO and HCNO cycles.

shown in Figure 2.23. This process is “terminated” when the β -decay half-life of a nucleus along the path is significantly longer than the burning time of the astrophysical event or proton capture leads to an unstable species. In recent years the search for the possible termination points has concentrated on ^{65}As , ^{69}Br , and ^{73}Rb . The isotope of ^{73}Rb is generally considered to be proton unstable ($S_p = -590 \pm 270$ keV), but the stability of ^{65}As ($S_p = -70 \pm 250$ keV) and ^{69}Br ($S_p = -180 \pm 300$ keV) is questionable as can be seen from the proton separation energies (using data from the most recent nuclear mass tables [aud93]). A large amount of research was conducted to search for proton dominant decay of ^{65}As and ^{69}Br , but no evidence for this was observed [rob90, win93].

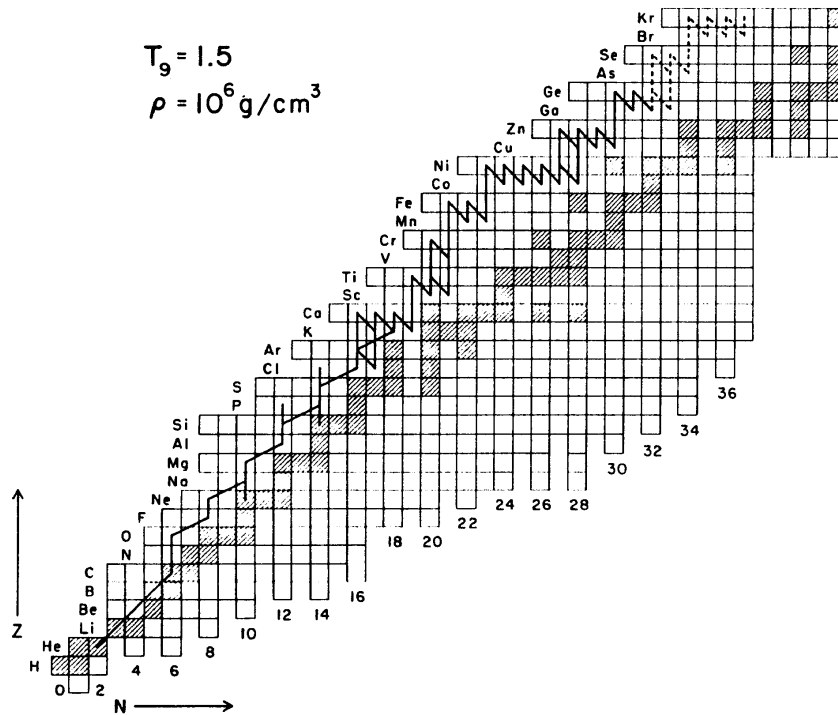
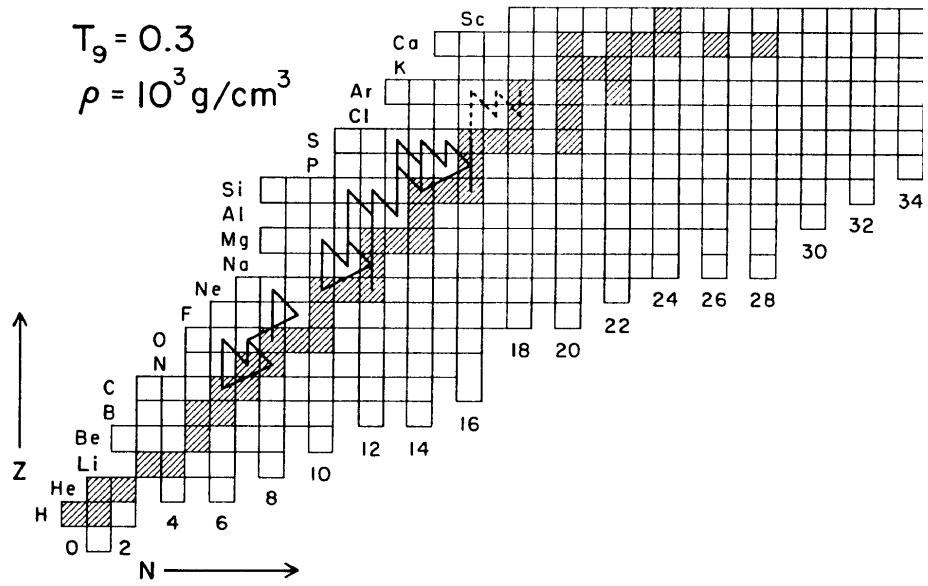


FIGURE 2.22: Proposed rp-paths for varied temperature and density conditions.

In one of the first experiments performed with the A1200 [she91], Mohar *et al.* [moh91] saw the first evidence for many new nuclei along the proton-drip line which were important for information related to the rp-process. The experiment provided clear evidence for the existence of ^{65}As , along with several possible events which could be attributed to ^{69}Br (see Figure 2.24 where first observed nuclei are indicated by arrows). No evidence for ^{73}Rb was seen, and it was concluded that ^{72}Kr was the termination point for the rp-process. In a subsequent experiment [win93] an attempt was made to measure the half-lives for many of the nuclei first observed nuclei by Mohar *et al.* [moh91] and the measurements allowed determination of the half-lives of ^{61}Ga , ^{63}Ge , and ^{65}As which provided vital information for the theoretical network calculations used in determining

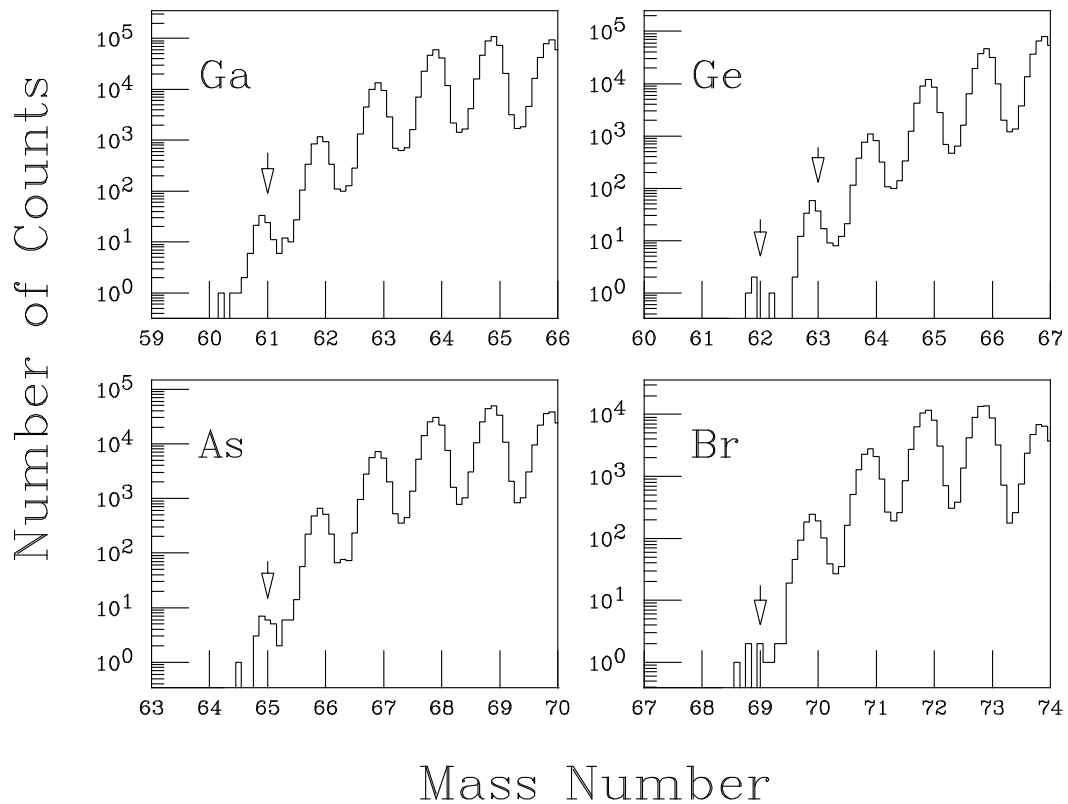


FIGURE 2.24: Isotopic yields resulting from $^{78}\text{Kr} + ^{58}\text{Ni}$ at 65 MeV/nucleon.

outcomes of the astrophysical processes. However, no evidence for ^{69}Br was obtained during this experiment. An experiment recently performed at GANIL [bla95] further extended the known limits of the proton-drip line in an attempt to study the nuclei along the rp-path. Fragmentation of $^{78}\text{Kr} + \text{Ni}$ at 73 MeV/nucleon was employed in an effort to maximize the possible rate of ^{69}Br . The yield for various isotopes is shown in Figure 2.25, and it is apparent that no evidence for the existence of ^{69}Br was observed. A limitation was placed on the possible half-life for ^{69}Br in this experiment which had a flight path over six times the length of the one performed by Mohar *et al.* and it was pointed out that this could be an indication of a very short half-life of ^{69}Br . Since the stability of ^{69}Br is critical to the understanding of the rp-process, the present work was carried out with a relatively short flight path and also mapped the momentum distributions and measured the cross sections of the isotopes produced in the reaction $^{78}\text{Kr} + ^{58}\text{Ni}$ in which evidence of ^{69}Br was first observed.

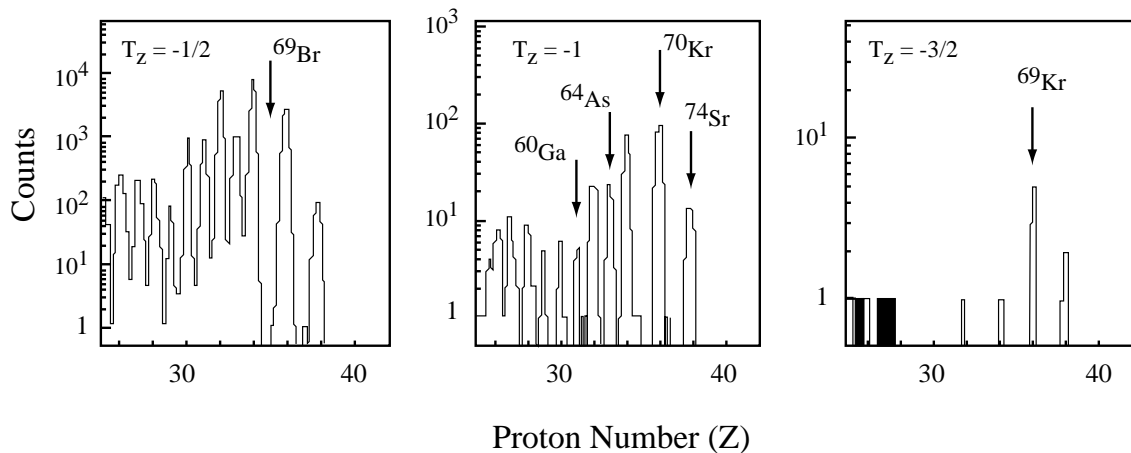


FIGURE 2.25: Yield from the fragmentation of $^{78}\text{Kr} + \text{Ni}$ at 73 MeV/nucleon.

In an effort to gain a greater understanding of the processes occurring during intermediate energy projectile fragmentation, to explore possible termination points of the rp-process, and to determine the applicability of high energy calculations to the intermediate energy regime two experiments were performed which involved the fragmentation of both neutron- and proton-rich krypton nuclei. The experimental procedure and set-up are described in the next chapter and are followed in subsequent chapters by the results that were obtained.

Chapter 3

Experimental Apparatus and Analysis

3.1 The A1200 Fragment Separator

The measurements were performed at the National Superconducting Cyclotron Laboratory using a ~ 0.1 pnA ^{86}Kr beam at 70 MeV/nucleon delivered by the K1200 cyclotron for the neutron-rich fragmentation and a ~ 45 ppA ^{78}Kr beam at 75 MeV/nucleon for the proton-rich fragmentation. The beam was incident on a 4 mg/cm^2 ^{27}Al target placed at the medium acceptance target position of the A1200 mass separator [she91] in the former experiment and a 102 mg/cm^2 ^{58}Ni target in the latter. The angular acceptance for fragments was $\Delta\theta = 34$ mrad and $\Delta\phi = 30$ mrad centered around 0° in the ^{86}Kr fragmentation experiment and the acceptance for fragments was $\Delta\theta = 20$ mrad and $\Delta\phi = 40$ mrad centered around 0° for the ^{78}Kr fragmentation. The momentum acceptance for both experiments was $\Delta p/p = 3\%$. The thickness of the target in the ^{86}Kr fragmentation experiment was chosen to limit the broadening of the fragment momentum distributions induced by energy and angular straggling in the target, rather than to optimize the production rate of specific fragments. This enabled a detailed study of the isotopic parallel momentum distributions. The target for the ^{78}Kr fragmentation was chosen to optimize the production rate for the bromine isotopes in an effort to explore the mass region relevant to possible termination points of the rp-process thoroughly. In both experiments, the

magnetic rigidity of the separator was varied in overlapping steps of 2% covering a range that would allow identification of a wide variety of isotopes in the regions of interest ($B\rho = 2.40$ to 2.85 Tm for ^{86}Kr fragmentation and $B\rho = 2.27$ to 2.49 Tm for the ^{78}Kr fragmentation). Four beam monitor detectors mounted around the target position in a cloverleaf pattern enabled normalization of the beam current for data taken at different rigidity settings.

3.2 Detector Setup

The two fragmentation experiments used similar detector setups as is shown in Figure 3.1. In order to measure possible short halfives during the ^{78}Kr fragmentation experiment, a second silicon telescope was placed 7.5 m downstream of the Final Achromatic Image position (not shown in figure). For isotopes with a half life on the order of 100 ns, a reduced isotopic count rate would be observed in the second silicon telescope relative to the first due to the decay that would occur over the final 7.5 m of additional flight path.

For the ^{86}Kr fragmentation experiment, the velocity of each particle was determined from the time-of-flight (TOF) measured between two 8 mg/cm^2 plastic scintillators separated by a 14 m flight path. The timing scintillators were located at the Dispersive Image #1 and the focal plane of the A1200. During the ^{78}Kr fragmentation experiment the TOF of the reaction products was measured between an 8 mg/cm^2 plastic scintillator (located at Dispersive Image #1) and the front-most detector of either silicon telescope (flight path of 14 m or 21.5 m) through the use of a time pick-off signal. The position and angle of reaction products were measured at both the second dispersive image and at the focal plane with two pairs of X-Y position sensitive parallel plate avalanche

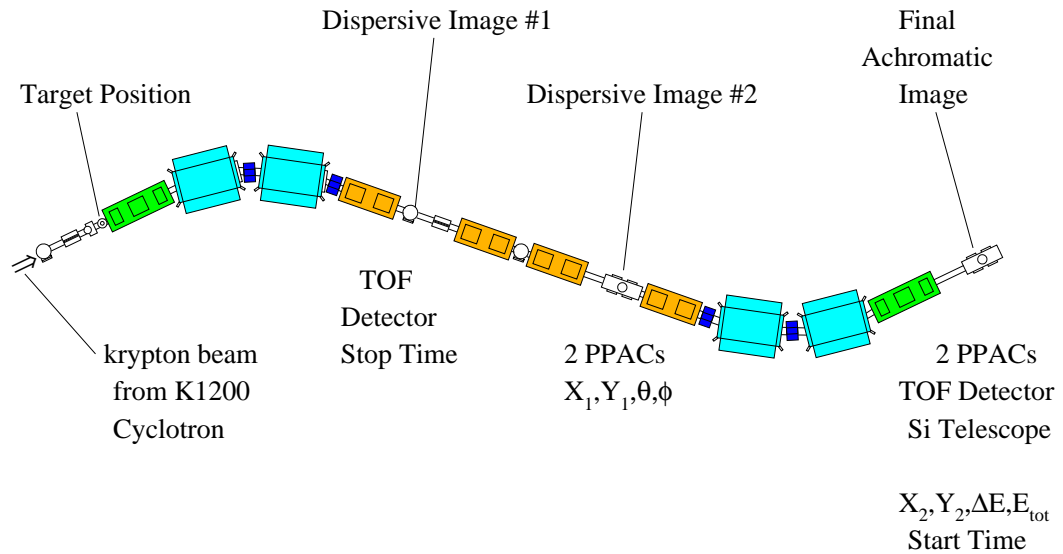


FIGURE 3.1: A schematic diagram of the A1200 fragment separator.

counters (PPAC's) [swa94] separated by approximately 40 cm. For each particle, the position information at the second dispersive image PPAC was used together with NMR measurements of the A1200 dipole fields to determine its magnetic rigidity $B\rho$, which is linearly related to the particle momentum via the equation

$$B\rho = \frac{p}{q}, \quad (3.1)$$

where q is the particle charge. Reaction products reaching the focal plane were implanted into a four-element silicon detector telescope, consisting of two $300\ \mu\text{m}$ ΔE detectors followed by two $1000\ \mu\text{m}$ thick E detectors in the ^{86}Kr experiment (the ^{78}Kr experiment was composed of detectors with thicknesses of $100\ \mu\text{m}$, $75\ \mu\text{m}$, $500\ \mu\text{m}$, and $1000\ \mu\text{m}$). All silicon telescope detectors had an active area of $300\ \text{mm}^2$.

3.3 Electronic Setup

Both fragmentation experiments were performed with a standardized A1200 electronics configuration. A schematic diagram of the electronic modules is shown in Figure 3.2. The TOF was measured with a TAC between the timing scintillator at Image #1 and the timing detector located in the focal plane (either a second timing scintillator or the first silicon detector time pick-off). The four signals (left, right, up, and down) from each PPAC were read by ADC's. The energy signals from the silicon detectors were sent to ADC's and the time signal from the front most silicon detector was read by a TDC. The master gate was constructed using valid signals from the two ΔE detectors and a NOT BUSY CPU signal. Additional software gating insured that each energy signal had a valid PPAC signal by checking the validity of BIT 2 and BIT 3. A total of 30 detector events were recorded for every valid master gate. The data acquisition system (both hardware and software) that was used to read the ADC's, TDC's, QDC's, and write the data to tape was the standard NSCL data acquisition system [fox89].

3.4 Isotopic Identification

By transporting charge states of the primary beam through the A1200 at different rigidity settings the relationship between the magnetic rigidity and the horizontal position at the second dispersive image was calibrated. An example of this can be seen in Figure 3.3. The momentum for each of the primary beam charge states is then determined through the use of Eq. 3.1. Using the momentum of the charge states, an energy calibration for each silicon detector is initially determined by comparing the ADC channel for the silicon detector to the amount of energy that should have been deposited in the detector (through the use of the formalism found in Hubert *et al.* [hub89]). The total

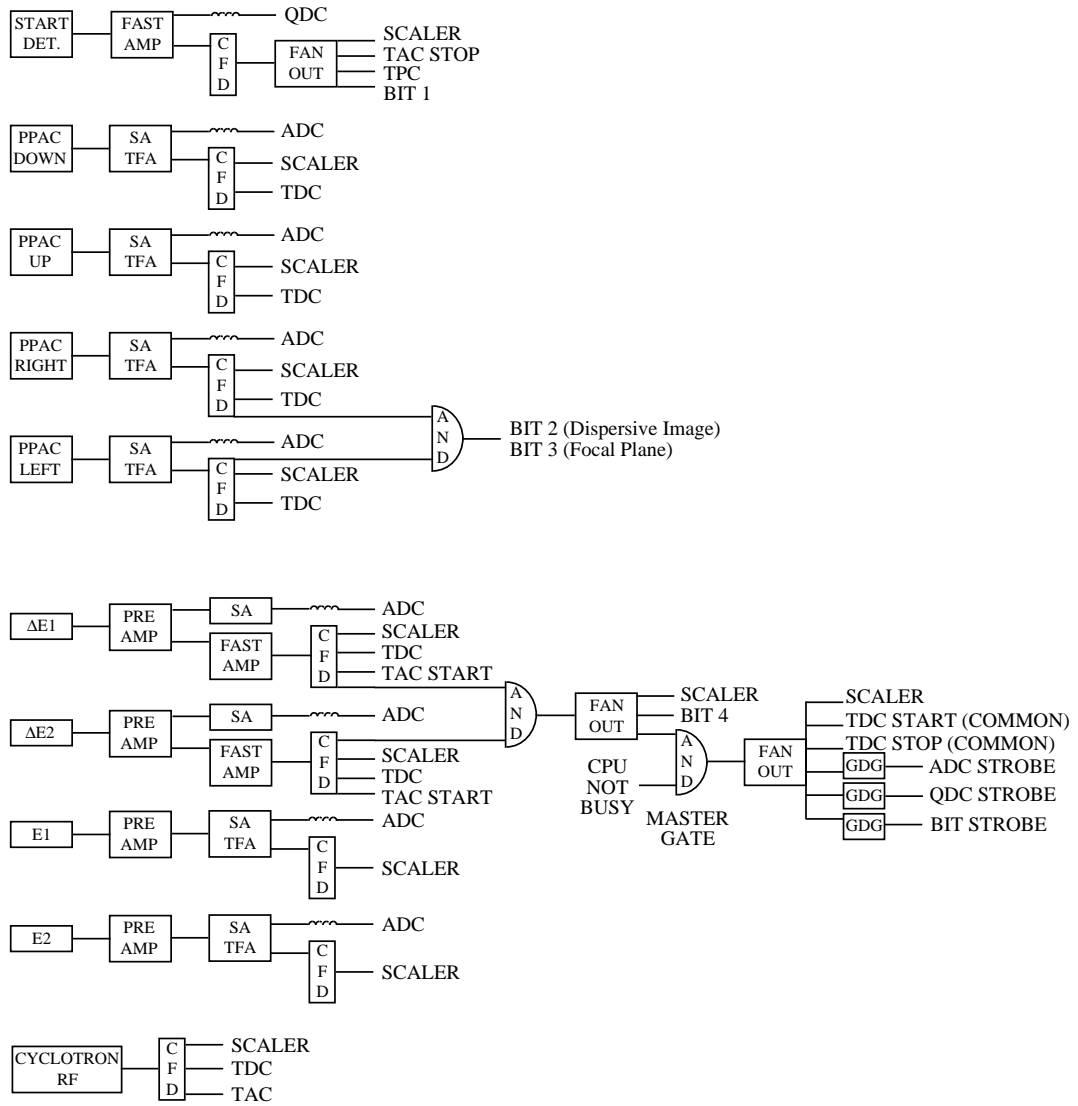


FIGURE 3.2: A schematic diagram of the electronic setup that was used during the fragmentation experiments.

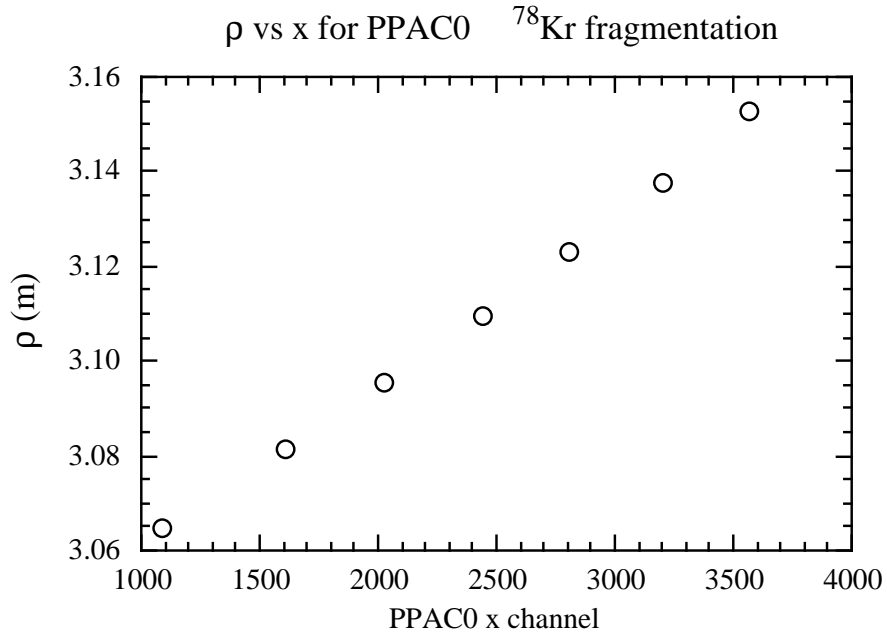


FIGURE 3.3: Turning radius vs. horizontal position for PPAC0 at Dispersive Image #2 that was observed during the ⁷⁸Kr fragmentation experiment.

kinetic energy is then determined by summing the energy loss in all four silicon detectors. Using the obtained values of ΔE , total kinetic energy, TOF, and magnetic rigidity, it is possible to determine unambiguously the mass (A), proton number (Z), and charge state (Q) of individual isotopes using standard relationships:

$$Z = a + b\sqrt{\Delta E(\gamma - 1)} \quad (3.2)$$

$$Q = \frac{3.105}{931.5} \cdot \left(\frac{T \cdot m}{\text{MeV}} \right) \cdot \frac{\text{TKE} \cdot B\rho}{B\rho(\gamma - 1)} \quad (3.3)$$

$$A = \frac{QB\rho}{3.105\beta\gamma} \cdot \frac{1}{T \cdot m} \quad (3.4)$$

where a and b are constants determined for each detector, TKE is the total kinetic energy with dimensions of MeV, and $B\rho$ is the magnetic rigidity with dimensions of Tesla-meter, and β and γ are the standard relativistic parameters ($\beta = v/c$ and $\gamma = 1/\sqrt{1 - \beta^2}$)

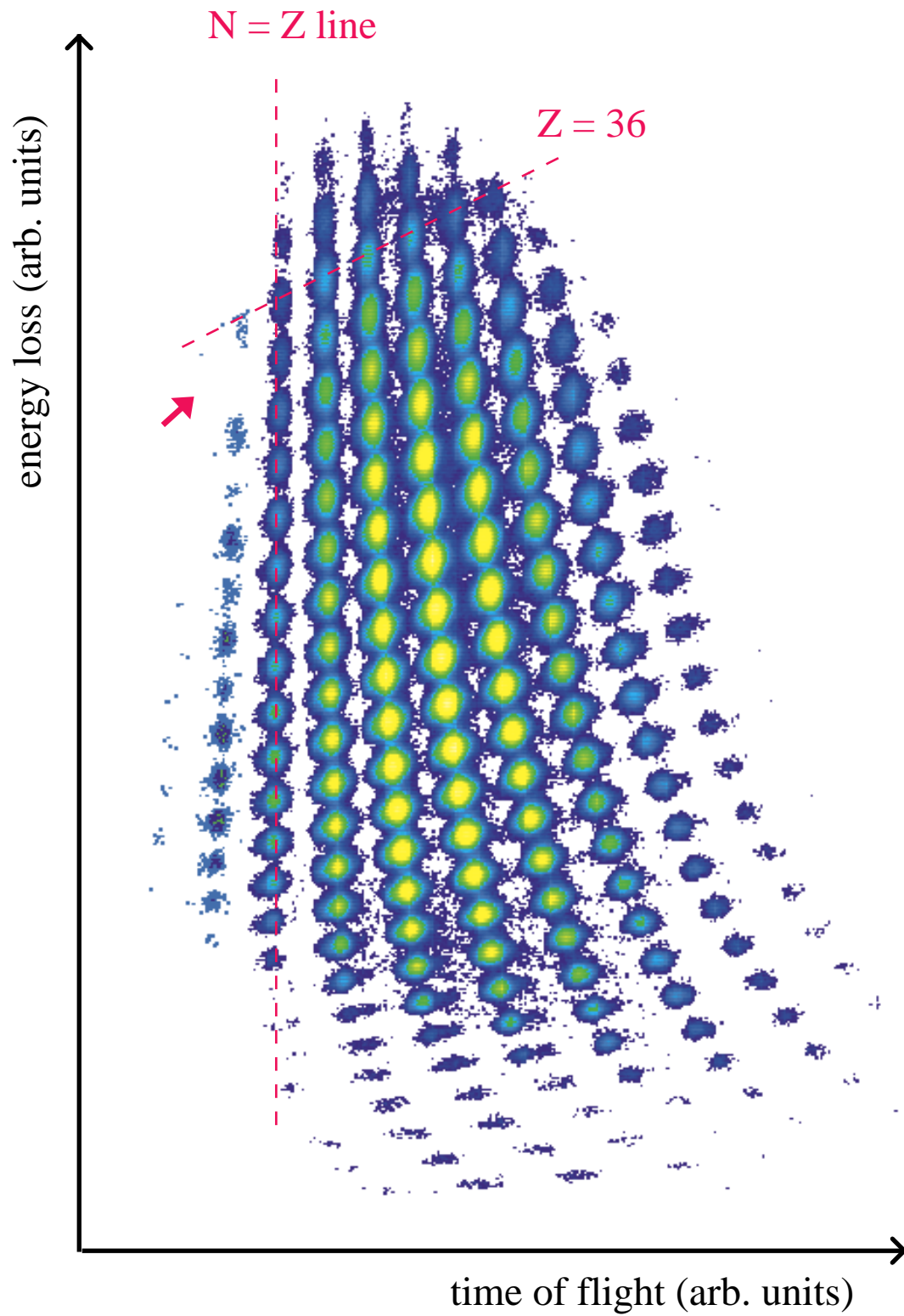


FIGURE 3.4: A plot of ΔE vs. TOF observed during the reaction $^{78}\text{Kr} + ^{58}\text{Ni}$. The arrow indicates the “gap” where ^{69}Br should be observed.

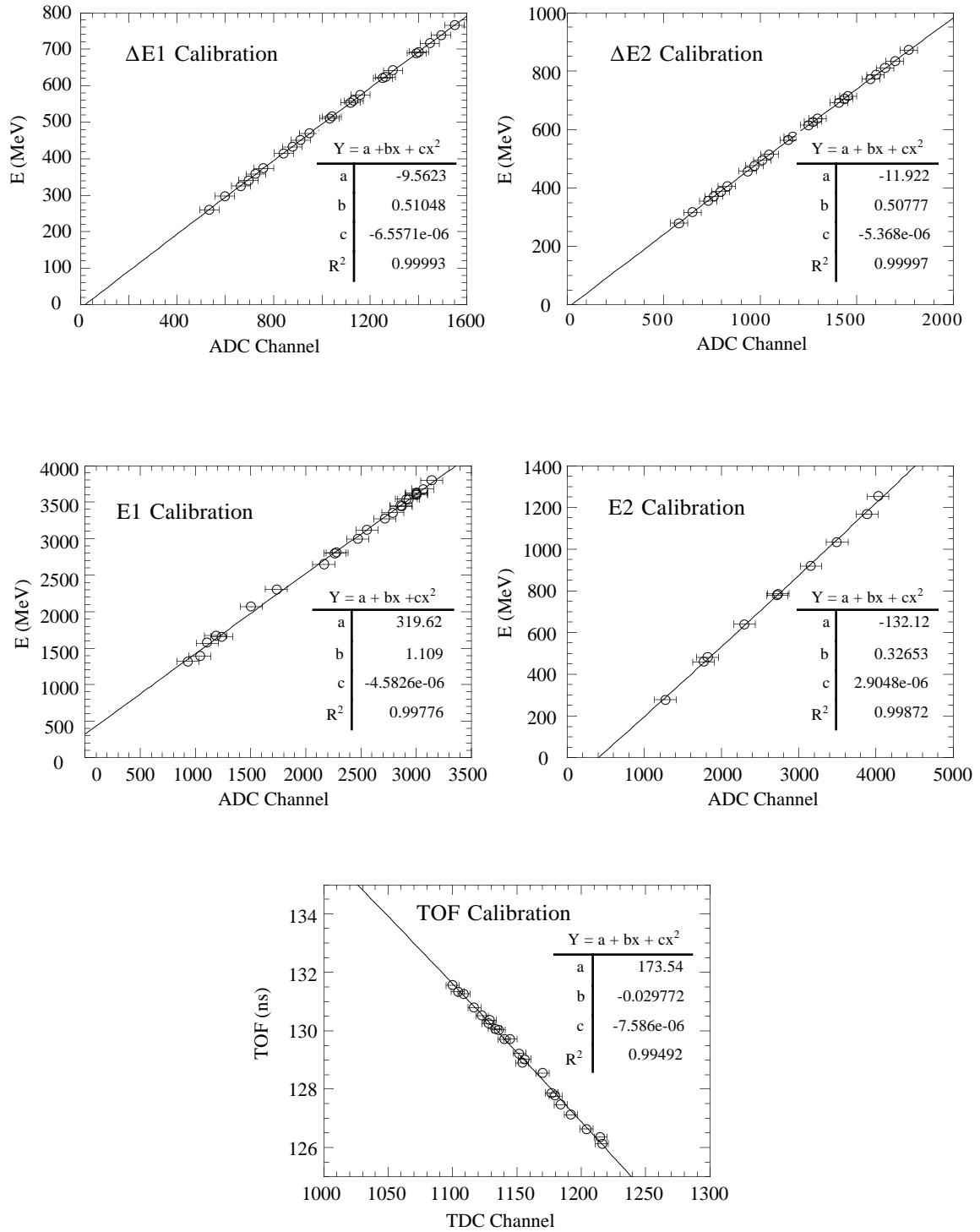


FIGURE 3.5: Energy and time calibrations for the detectors during the ^{86}Kr fragmentation experiment.

determined from the TOF of the fragment. The two ΔE measurements provided redundant proton number (Z) determinations. The Z calibration was done using the 2-dimensional ΔE vs. TOF data for a given magnetic rigidity. A sample ΔE vs. TOF plot in which the magnetic field was optimized to observe ^{69}Br is shown in Figure 3.4. The figure indicates the $N=Z$ line and the krypton isotopic line. By selectively gating on a wide variety of isotopes in the ΔE vs. TOF plot, it is possible to obtain good energy and time calibrations which span the range of the observed data. Energy and time calibrations for the ^{86}Kr experiment are shown in Figure 3.5.

The charge of each particle is then determined with Eq. 3.3. The good charge resolution enabled an integer value of Q to be used when determining the mass number (A) with Eq. 3.4. Using these equations, the present measurements had resolutions (FWHM) of $\Delta A \sim 0.004$, $\Delta Z \sim 0.01$, and $\Delta Q \sim 0.01$ (shown in Figure 3.6), which allowed clear separation of all the fragments. With the A, Z , and Q of each event determined, it became possible to explore the momentum distributions and cross sections of the fragmentation products.

3.5 Parallel Momentum Distributions

Given the number of events for each individual isotope at a given magnetic rigidity (which corresponds to a particular momentum through the use of Eq. 3.1), a figure consisting of the number of events (or events/sec) plotted against the momentum of the individual particle is constructed. The number of events at the individual rigidity settings were normalized relative to each other with the information provided by the beam monitor

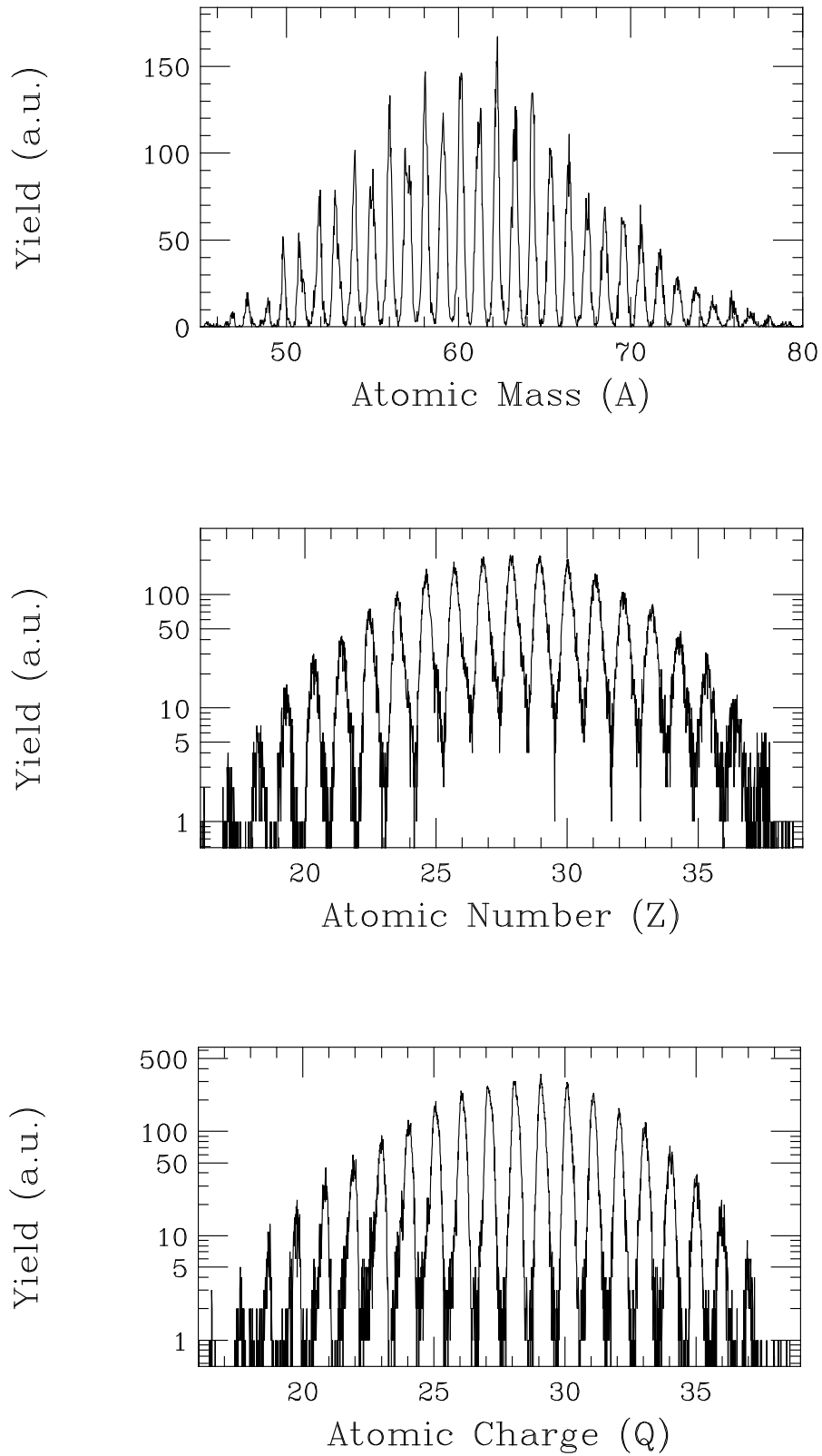


FIGURE 3.6: The A,Z, and Q resolution obtained in the ^{86}Kr fragmentation experiment.

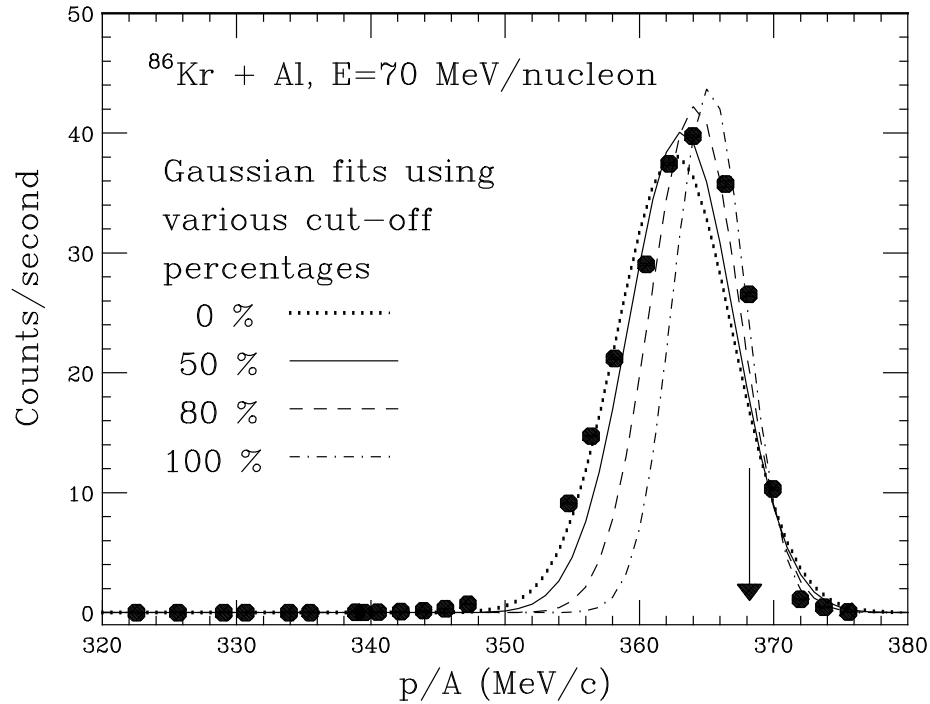


FIGURE 3.7: The momentum distribution of $^{80}\text{Br}^{35+}$ with varied Gaussian fits. The arrow indicates the projectile momentum.

detectors. Since the particle momentum is parallel to the momentum of the projectile this type of figure provides the parallel momentum distribution for each individual isotope (as an example, parallel momentum distribution for $^{80}\text{Br}^{35+}$ is shown in Figure 3.7).

The parallel momentum distribution of each isotope was fitted with a Gaussian function from which the parallel momentum width and the mean momentum transfer were obtained. The isotopic yield was extracted by integrating the Gaussian fit over momentum space, however, the projectile-like fragment momentum distributions at this energy are generally asymmetric, with a tail on the low-momentum side of the momentum distribution. The effect of this asymmetry on the present data was explored through the use of “cut-off percentages” on the low-momentum side of the distributions. For the ^{86}Kr experiment the Gaussian functions were fitted to the data with a least-squares technique

from varying percentages of the peak height on the low momentum side to the end of the high momentum side of the distribution. A typical momentum distribution from the ^{86}Kr data is shown in Figure 3.7 along with Gaussian fits done with varying cut-off percentages on the low momentum side of the distribution. The figure indicates that the width of the distribution becomes narrower as the cut-off increases toward the top of the peak. Previous papers have used a variety of cut-off percentages during the data analysis and there is no standardized percentage that is typically used. The 50% cut was selected as the best representation of the ^{86}Kr data for subsequent discussion, and the errors introduced by the varied cut-off percentages will be discussed along with the results. The ^{78}Kr experiment was performed with a relatively thick target and the momentum distributions were far more Gaussian in shape than was the case for the ^{86}Kr data. The choice of cut-off percentage for the ^{78}Kr data did not have a noticeable effect on the fits, and no cut-off was applied to the low momentum side of the ^{78}Kr data.

After determining a Gaussian fit for each isotope, the momentum shift was obtained by comparing the centroid of the Gaussian fit in momentum space to the momentum of the primary beam (indicated by the arrow in Figure 3.7).

The cross section for each isotope was determined by integrating the Gaussian fit over momentum space to obtain the total yield for each individual isotope. The beam current measurement (from the four beam monitor detectors and a measurement made periodically with a Faraday cup inserted at the entrance of the A1200) provided information about the total number of projectile particles incident upon the target. After correcting the isotopic yield of each element for the acceptance of the A1200 fragment separator, the cross section was then determined from standard formulae.

Chapter 4

Results and Discussion

4.1 Fragmentation of ^{86}Kr Projectiles

4.1.1 Momentum Widths

In the Goldhaber model [gol74], the removal of independent nucleons from the projectile results in a Gaussian momentum distribution. The width of this distribution is given by the expression

$$\sigma_{\parallel} = \sigma_0 \sqrt{\frac{A_F(A_P - A_F)}{A_P - 1}} \quad (4.1)$$

where A_F is the fragment mass, A_P is the projectile mass, and σ_0 is a reduced width related to the Fermi momenta of the individual nucleons ($\sigma_0^2 = p_{\text{Fermi}}^2 / 5$). This model reproduces the parallel momentum distribution widths of the PLF's relatively well for high energy fragmentation, and for light ion fragmentation at intermediate energies [gol74]. However, the experimental value of σ_0 is typically found to be smaller than the values predicted using known Fermi momenta. Several arguments have been presented to explain the observed narrowing of the width. One possibility is that Pauli exclusion effects could lead to a decreased width [ber81], while another argument [web94] points out the fact that the width predicted by the Goldhaber model is relevant to the prefragments - not the final

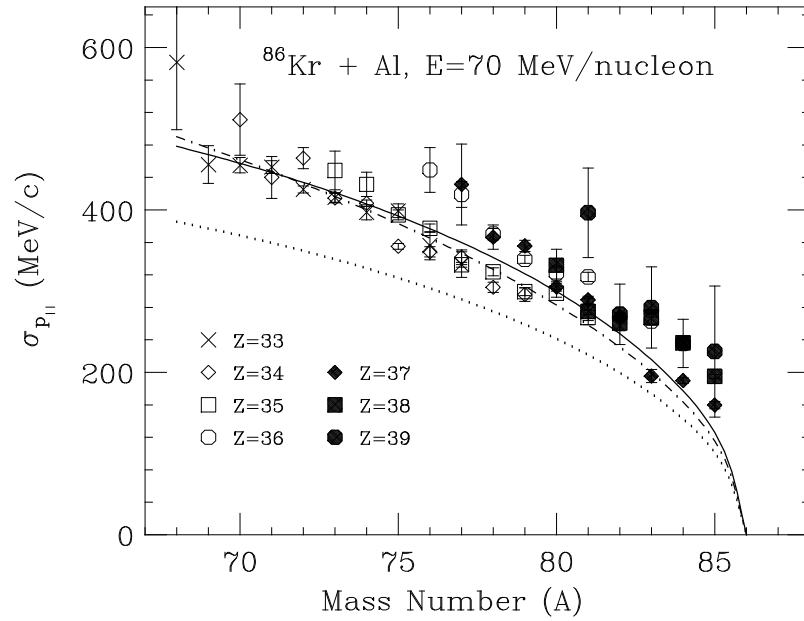


FIGURE 4.1: Parallel momentum distribution widths for isotopes observed during the fragmentation of ^{86}Kr .

observed fragments. The prefragments will undergo a particle evaporation step leading to mass loss but little increase in momentum width (given isotropic evaporation), thereby yielding momentum widths smaller than expected. The present measured values of the parallel momentum widths in the projectile rest frame are shown in Figure 4.1 (error bars represent the statistical error added in quadrature with the uncertainty due to cuts on the tail of the momentum distributions). The best fit to our data using the Goldhaber model with $\sigma_0 = 124 \text{ MeV/c}$ is indicated by the solid line. By interpolating results obtained in a quasi-elastic electron scattering measurement [mon71], we obtain a value of $p_{\text{Fermi}} = 260 \text{ MeV/c}$ for ^{86}Kr which translates into a $\sigma_0 \sim 116 \text{ MeV/c}$. Also shown in Figure 4.1 are the results from calculations with the ISApac code [fau92] fit with the Goldhaber model (dotted line). This approach yields a reduced width of $\sigma_0 \sim 100 \text{ MeV/c}$ which is also

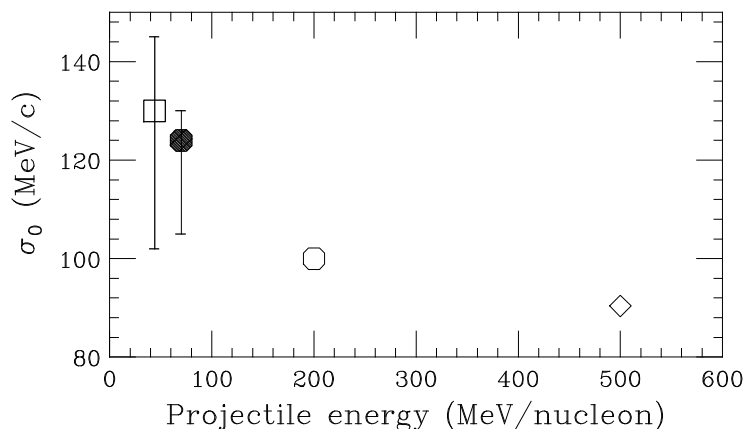


FIGURE 4.2: Parallel momentum width from recent krypton fragmentation experiments.

smaller than the value obtained with our data. The dot-dash line in Figure 4.1 shows a calculation based on the systematics of Morrissey [mor89] that were obtained from parametrization of high energy fragmentation data. The parallel momentum width in this parametrization is given by

$$\sigma_{\parallel} = \text{const} \cdot \sqrt{\Delta A} \quad (4.2)$$

where $\Delta A = A_P - A_F$ and the constant is generally between 85 - 100 MeV/c. The best fit to our data requires a constant of 120 MeV/c, which is again larger than the typical value determined from high energy fragmentation. Values of the reduced width obtained from other experiments involving krypton fragmentation at various energies [web94, ste91, baz90] are summarized in Figure 4.2. The values of the reduced width for both the 200 MeV/nucleon and 500 MeV/nucleon data were obtained by applying a best fit with the Goldhaber model while limiting the fit to the fragment range covered in the present work. The experiments performed at higher energies (^{84}Kr at 200 MeV/A [ste91] and ^{86}Kr at 500 MeV/A [web94]) have best fit values of $\sigma_o \sim 100$ MeV/c and $\sigma_o \sim 90$ MeV/c,

respectively. After applying a 50% cut to the $^{72}\text{Ge}^{31+}$ momentum distribution shown in Figure 4 of Bazin *et al.* [baz90] a value of $\sigma_0 \sim 130$ MeV/c is estimated for the 44 MeV/nucleon $^{86}\text{Kr} + ^{27}\text{Al}$ data. Applying an 80% cut to the low energy side of the momentum distribution yields a value of $\sigma_0 \sim 105$ MeV/c. Figure 4.2 shows that the reduced width observed during heavy-ion fragmentation exhibits a definite broadening as the projectile energy is lowered into the intermediate energy regime. This is in contrast to fragmentation involving light and intermediate mass projectiles where the general trend shows a relatively constant reduced width until the intermediate energy range is reached, where the reduced width begins to decrease smoothly [mur83].

The large parallel momentum distribution widths observed in the present data are probably due to the coexistence of competing reaction mechanisms in the intermediate energy regime. Apart from the ‘pure’ fragmentation component (that completely dominates at higher energies), both the low-energy tail typical of more dissipative processes [got91] and the broadening associated with nucleon pick-up reactions during the formation of the prefragment [sou92] will increase the distribution width. The value of $\sigma_0 \sim 124$ MeV/c was obtained with a cut-off at 50% of the peak height on the low momentum side of the momentum distribution. It should be noted that as the momentum distributions begin showing tails on the low momentum side for experiments performed in the intermediate and low energy regimes, various assumptions have to be made about the effect of the low energy tail. Qualitative decisions have been made on how much of the tail to include and this, of course, can lead to different interpretations of data. In the present data, Gaussian fits including the entire tail yield a value of $\sigma_0 \sim 130$ MeV/c while placing the cut-off at 80% of the peak height yields a value of $\sigma_0 \sim 115$ MeV/c. Performing a fit

exclusively with the high energy side of the momentum distribution (i.e. a 100% cut-off) yields a value of $\sigma_o \sim 105$ MeV/c, although the fit is rather qualitative (see Figure 3.7).

4.1.2 Momentum Transfer

Morrissey [mor89] has defined average parallel momentum transfer $\langle P'_{\parallel} \rangle$ as the product of the projectile mass, the average measured velocity of the fragment β_{\parallel} , and a kinematic factor of $\beta\gamma/(\gamma+1)$, and has shown that a linear relationship exists between $\langle P'_{\parallel} \rangle$ and the product of the total number of nucleons removed from the projectile ΔA , with a slope parameter of 8 MeV/c (see Section 2.1). This dependence was derived from high energy fragmentation data. The average parallel momentum transfer $\langle P'_{\parallel} \rangle$ for the individual elements is shown in Figure 4.3 together with the results of a calculation with the ISApac code [fau92] (denoted by asterisks) which shows good agreement with the present data. The statistical error is smaller than the plotted points. Changing the Gaussian fit cut-off percentage on the momentum tail has a relatively small effect on the determination of the parallel momentum transfer, introducing an uncertainty of $\sim 2\%$ (the shift of the Gaussian centroid can be seen in Figure 3.7) which was added in quadrature to the statistical uncertainty. The solid lines in Figure 4.3 are the result of a linear fit to all the fragment data with $Z \leq 36$. The resulting slope parameter of 8.8 MeV/c (represented by solid lines) is in good agreement with the overall trend of the fragmentation products ($Z \leq 36$), while the pick-up products differ significantly from this trend. Recent measurements [ste91] at an energy of 200 MeV/nucleon have a similar slope for the overall fit to the fragmentation products while the slopes of the individual elements exhibit deviations from this trend. As is evident from Figure 4.3, the slopes of the individual fragmentation elements ($Z \leq 36$) are slightly steeper than the 8.8 MeV/c average slope, where linear best-

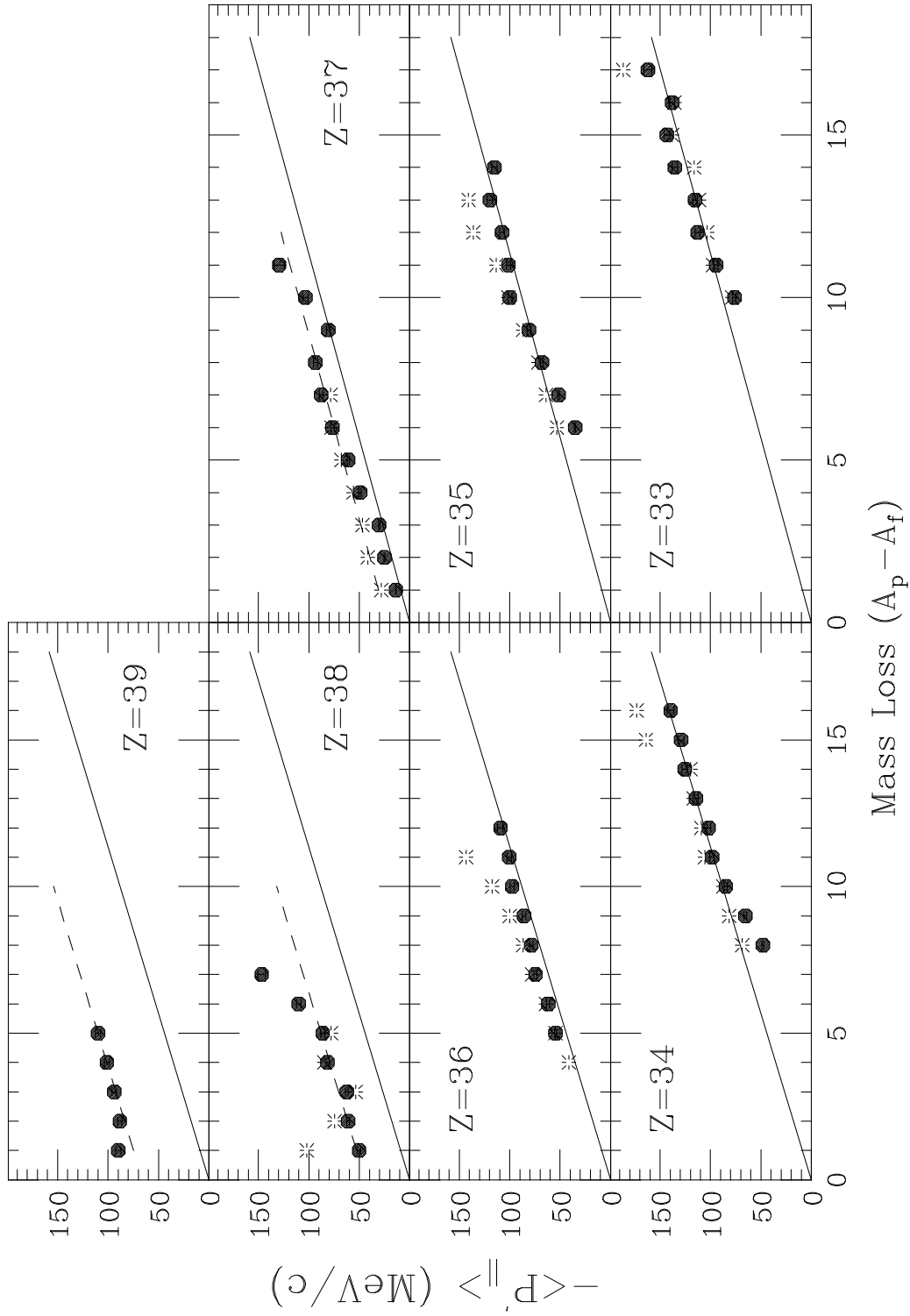


FIGURE 4.3: Momentum transfer vs. mass loss for the projectile-like fragments observed during ^{86}Kr fragmentation at 70 MeV/nucleon.

fit slope parameters for the individual elements change monotonically as shown in Table 4.1. This effect indicates that a larger excitation energy is required to produce the proton-rich isotopes which then causes a greater downshift in momentum relative to the neutron-rich isotopes. Recent data from krypton fragmentation at 500 MeV/nucleon [web94] showed a very similar effect, with the slope parameters of the PLF's being larger than 8.8 MeV/c. However, the slope parameters in the high energy krypton fragmentation [web94] increase strongly as the proton number decreased from $Z = 36$ (14 MeV/c) to $Z = 30$ (58 MeV/c). An increased slope parameter for individual elements was also observed in xenon fragmentation at 790 MeV/nucleon [fri93] in which case the data yielded a slope of ~ 16 MeV/c for the near-projectile elements.

Table 4.1: Fitted slope parameters for individual elements from ^{86}Kr fragmentation.

Proton number (Z)	Slope Parameter
33	11.6 ± 0.4
34	12.2 ± 0.3
35	12.1 ± 0.2
36	12.5 ± 0.2
37	10.7 ± 0.2
38	11.9 ± 0.4
39	5.5 ± 0.8

More interesting are the parallel momentum transfers of the charge pick-up products which deviate significantly from those of the fragmentation products. The formation of the pick-up products (in this case with $Z > 36$) is assumed to take place during the initial prefragment formation when individual protons are acquired from the target nucleus. The final observed fragment is then formed through neutron evaporation. Another possible production mechanism is the excitation of a Δ -resonance that can

change the isospin of a projectile nucleon. However, the ISApac calculations indicate that for ^{86}Kr fragmentation at 70 MeV/nucleon this effect can account for no more than 0.5% of the total charge pick-up products. Using momentum conservation arguments similar to those used by Souliotis *et al.* [sou92], we can determine the momentum shift arising purely from picking up protons. Initially the projectile has a momentum p_P with a mass number A_P and the proton in the target has a momentum of p_t . After the collision the prefragment has a momentum of p_{PF} and a mass number of $A_P + \Delta A_t$ where ΔA_t is the number of nucleons removed from the target. Assuming the evaporation is isotropic, the average final fragment velocity (v_F) will be identical to the average velocity of the prefragment, and it can then be shown that the velocity shift due to picking up the target nucleons is given by

$$\Delta\beta_{\parallel} = \frac{1}{m_0c} \cdot \frac{\Delta A_t}{A_P + \Delta A_t} \left[p_{\text{Fermi}} - \left(\frac{p_P}{A_P} \right) \right] \quad (4.3)$$

which corresponds to a shift in the parallel momentum transfer of

$$P'_{\text{offset}} = \frac{A_P}{A_P + \Delta A_t} \frac{\beta\gamma}{\gamma + 1} \Delta A_t \left[\left(\frac{p_P}{A_P} \right) - p_t \right] \quad (4.4)$$

where β and γ are the relativistic parameters from the initial projectile velocity and $m_0c = 931.5$ MeV/c. This offset is then added to the parallel momentum transfer yielding a parametrization of the form

$$-\langle P'_{\parallel} \rangle = 8.8 \frac{\text{MeV}}{c} \Delta A + P'_{\text{offset}} \Delta A_t \quad (4.5)$$

where the best-fit slope parameter of 8.8 MeV/c (the slope of the fragmentation products) was held fixed. Fitting the present charge pick-up data to this parametrization and adjusting the momentum of the picked-up proton(s), we obtain a value of $p_t \sim 220$ MeV/c.

The results are shown with dashed lines in Figure 4.3. The value obtained for the proton momentum indicates that the protons acquired during the pick-up process are moving parallel to the projectile with approximately their maximum Fermi momentum. This effect has previously been observed in reactions involving neutron pick-up [sou92].

4.1.3 Isotopic Cross Sections

The absolute cross sections for the $Z = 33$ (arsenic) through $Z = 39$ (yttrium) isotopes were obtained by integrating the Gaussian fits of the parallel momentum distributions over momentum space and are shown in Figure 4.4. The error bars indicate the statistical uncertainty added in quadrature to the uncertainty due to altering the fitting limits on the tail of the momentum distribution. Inclusion of the tail of the momentum distribution increases the cross sections by $\sim 8\%$. The absolute beam current was ~ 0.1 pA, however, the overall normalization is only accurate within a factor of two. The relative cross sections are much more precise than this. The absolute normalization uncertainty is not included in the error bars. The solid histograms represent the calculated cross sections from the ISApac model [fau92], which is considered to be valid between a few hundred MeV/nucleon and a few GeV/nucleon. ISApac uses the Yariv-Fraenkel ISABEL intranuclear cascade code [yar79] to model the prefragment formation step followed by a modified PACE evaporation code [gav80] to calculate the deexcitation step. The magnitudes and shapes of the predicted isotopic cross section distributions are in remarkable agreement with the experimental data for the fragmentation products ($Z \leq 36$). In contrast, the measured cross sections of the charge pick-up products are greater than predicted by ISApac, and this difference grows as the number of acquired protons increases (although the shapes of the distributions are reproduced rather well).

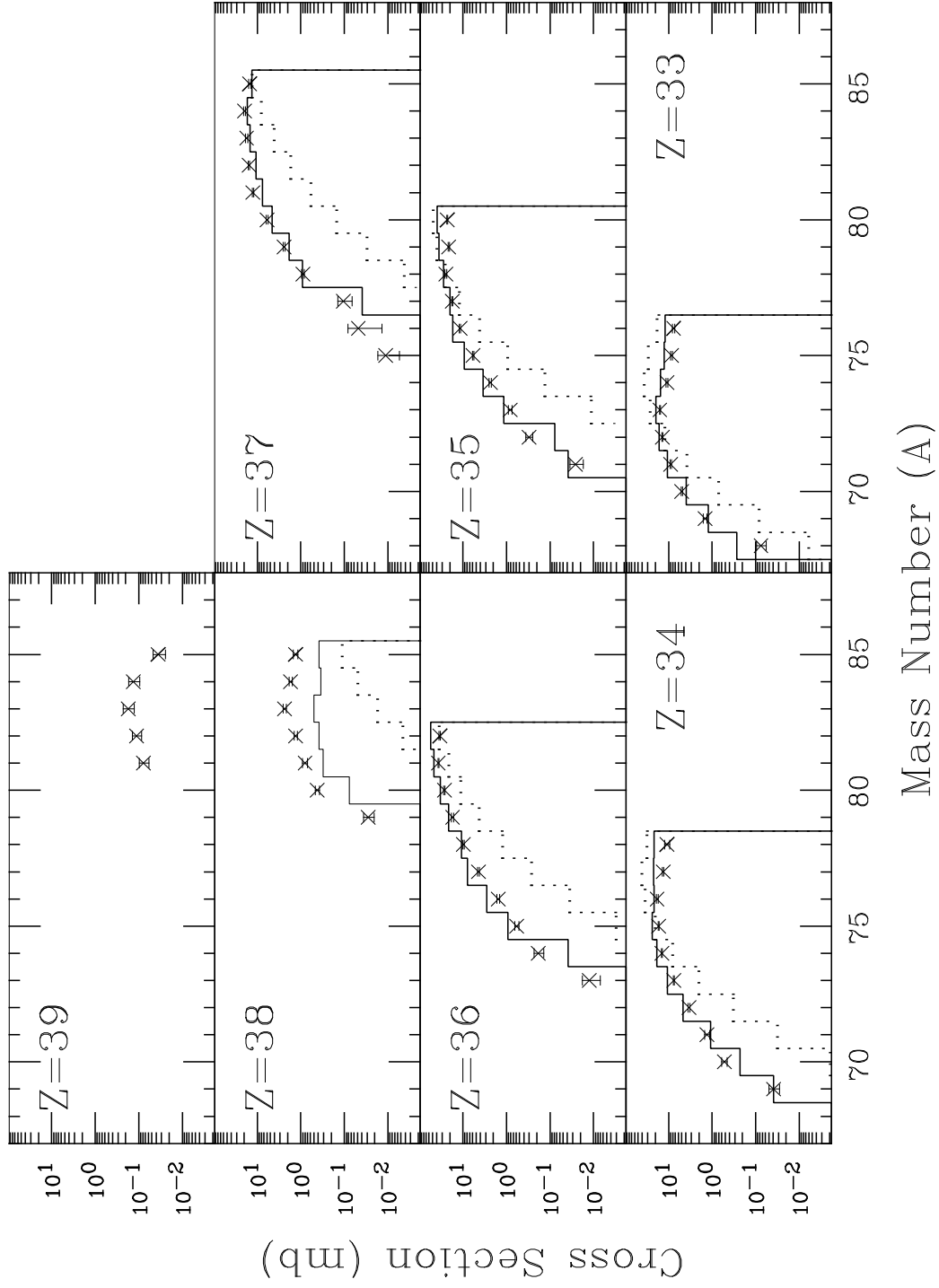


FIGURE 4.4: Isotopic cross sections determined from the fragmentation of $^{86}\text{Kr} + ^{27}\text{Al}$ at 70 MeV/nucleon.

Figure 4.4 also shows cross sections predicted from the semi-empirical parametrization (EPAX) established by Sümmerer *et al.* [sum90] (dotted histograms). Cross sections predicted by the EPAX code are generally higher than the observed cross sections for the neutron-rich isotopes while the proton-rich isotopes are underpredicted. This indicates that the evaporative step of the whole process contributes significantly to the proton-rich side of the isotopic chains, as expected for high excitation energies in the prefragments. Both ISApac and EPAX underpredict the cross sections of the charge pick-up products indicating that, as expected, the high-energy models are not able to reproduce the experimental data for the charge pick-up products.

The ISApac model has previously been used to predict the cross sections for 500 MeV/nucleon ^{86}Kr fragmentation as discussed by Weber *et al.* [web94]. In this case, the ISApac calculation predicted the cross sections fairly well, while the EPAX calculation showed a similar underprediction for proton-rich nuclei and overprediction of the neutron-rich nuclei that is observed for the current data at 70 MeV/nucleon. It was suggested that the Gaussian shape of the charge dispersion used in the EPAX formula needs to be modified in order to reproduce the data (see Eq. 2.4).

4.2 Fragmentation of ^{78}Kr Projectiles

The parallel momentum distributions of a number of reaction products were monitored on-line and fitted with a Gaussian function. The centroid values were then used to identify the most appropriate magnetic rigidity setting for the observation of ^{69}Br . The centroids (in terms of magnetic rigidity) for the isotopes covering $Z = 24$ to 38 are shown in Figure 4.5 where the horizontal dashed lines show the range of magnetic rigidity covered during this experiment. The general trends exhibited by the reaction products and

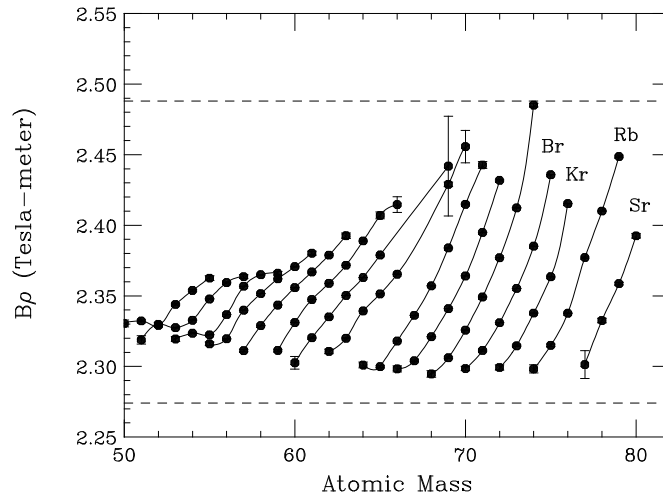


FIGURE 4.5: Centroids of parallel momentum distributions for isotopes observed during projectile fragmentation of $^{78}\text{Kr} + ^{58}\text{Ni}$ at 75 MeV/nucleon.

in particular that of the bromine isotopes, show that this rigidity range would have permitted the observation of ^{69}Br if it were stable.

4.2.1 Isotopic Cross Sections

Figure 4.6 shows the mass spectra for isotopes with atomic numbers $30 \leq Z \leq 38$ obtained at a fixed magnetic rigidity setting optimized for observation of ^{69}Br . The absence of ^{69}Br is clearly observed in the bromine mass spectrum, whereas other $T_z = -1/2$ nuclei are present. The asterisk symbols in Figure 4.6 indicate several events that can be attributed to ^{60}Ga and ^{70}Kr , confirming the recent identification of these isotopes by Blank *et al.* [bla95]. The measured isotopic cross sections, determined by integrating the Gaussian functions over momentum space after correcting for the acceptance of the A1200, are shown in Figure 4.7. Also shown in Figure 4.7 are the cross sections calculated from both the EPAX parametrization [sum90] and the ISApax model [fau92]. Both codes were originally developed for high energy (or ‘pure’) fragmentation ($E/A > 200$ MeV/

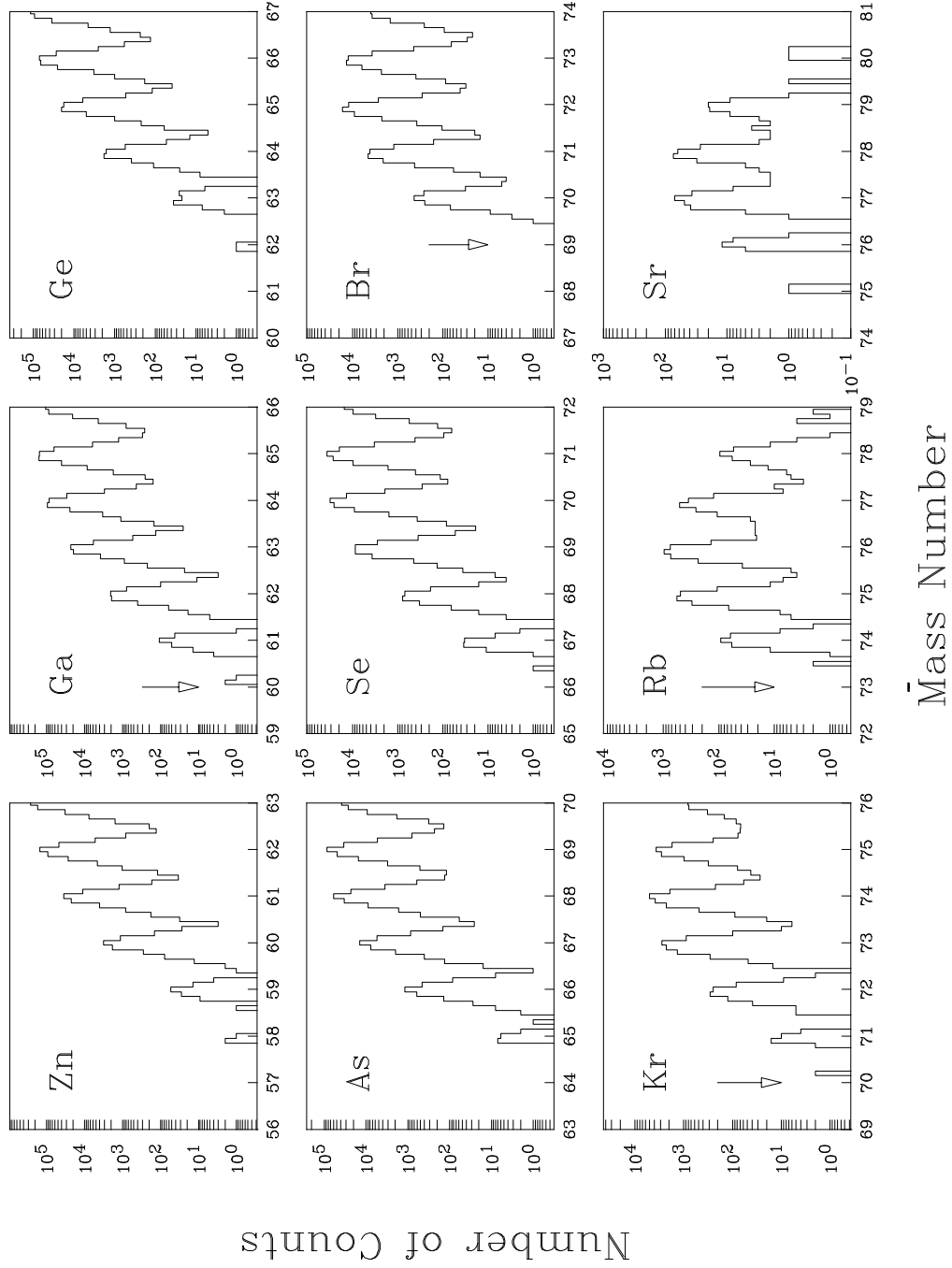


FIGURE 4.6: Mass distributions for the $Z=30$ to $Z=38$ isotopes recorded while magnetic rigidity was optimized for observation of ^{69}Br .

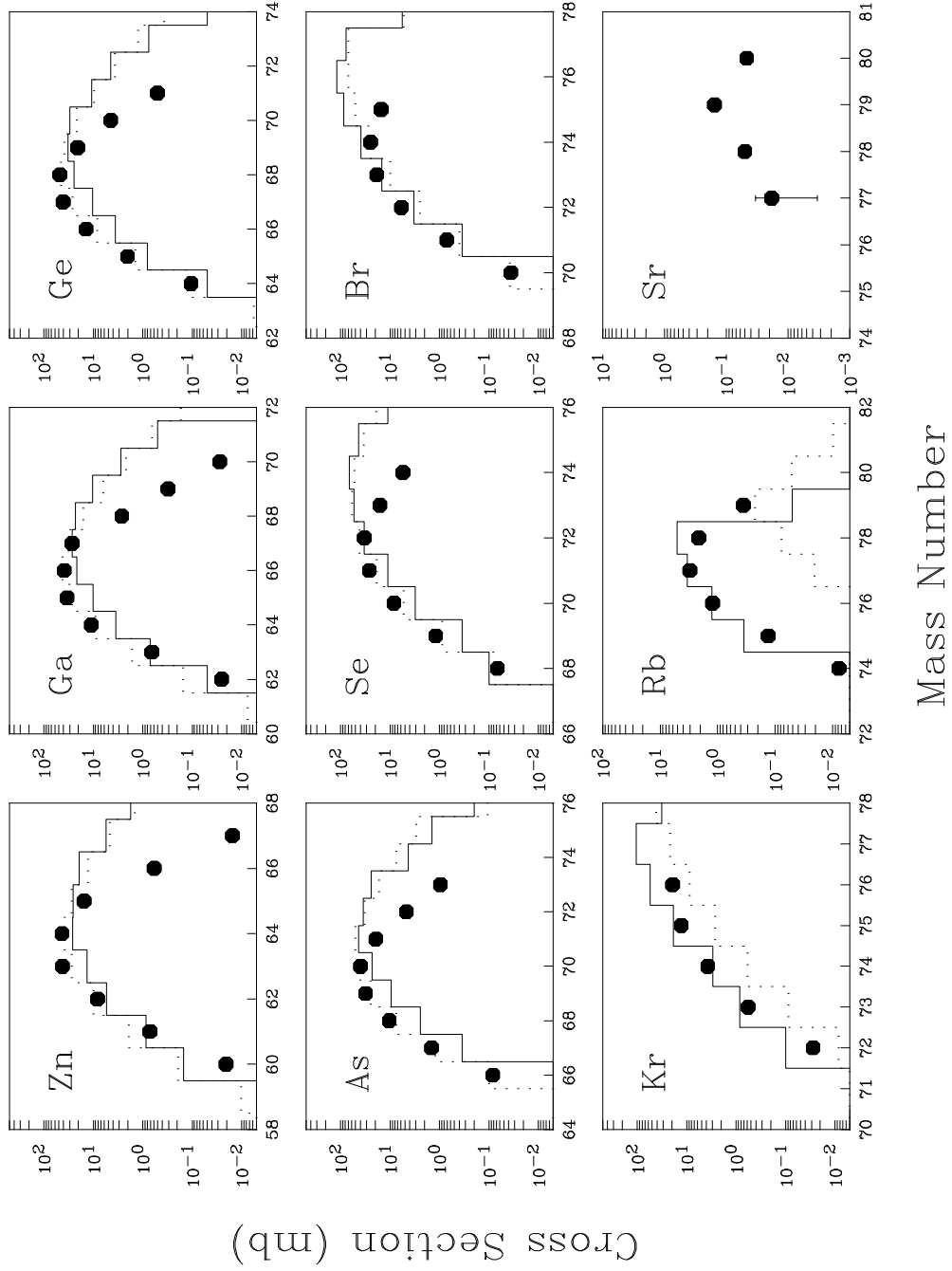


FIGURE 4.7: Isotopic cross sections determined from $^{78}\text{Kr} + ^{58}\text{Ni}$ at 75 MeV/nucleon.

nucleon), but recent experiments have shown their applicability for reactions involving intermediate-mass projectiles at intermediate energies [pfa95, fau96]. A comparison of the (absolute) experimental cross sections with the EPAX parametrization and the ISApac code shows several overall features. The EPAX code noticeably underpredicts the formation of proton pick-up products ($Z > 36$), a not unexpected feature considering this parametrization was developed from high-energy fragmentation in which pick-up reactions seldom occur. The ISApac code is able to reproduce relatively well the single-proton pick-up, but the predicted cross sections for reaction products that have acquired more than one proton ($Z > 37$) start to fall off dramatically. The magnitude of the predicted cross sections from both EPAX and ISApac agree relatively well for the reaction products below krypton ($Z < 36$), although the predicted distributions are more neutron-rich than the experimental cross section distributions ($Z \geq 30$).

4.2.2 Memory Effect

Together with the results of previous experiments which involve fragmentation of neutron-rich krypton projectiles (^{86}Kr and ^{84}Kr [pfa95, ste91]), the data from the ^{78}Kr fragmentation experiment can provide additional insight into the influence of the projectile N/Z ratio on the fragment charge dispersion distribution for reactions in the intermediate energy/intermediate mass regime. In order to include this effect properly in their semi-empirical fragmentation product cross section code, Sümmerer *et al.* [sum90] developed a parametrization that took into account previous observations from (target) fragmentation experiments; (i) the maxima of fragment charge distributions always lie on the neutron-deficient side of the valley of β stability, (ii) for targets/projectiles close to β -stability, the most probable charge of a fragment isobaric chain is only dependent on fragment mass,

and (iii) the size of the memory effect is different for neutron- and proton-rich projectiles.

Chu *et al.* [chu71] had described this effect as

$$Z_p(A) = Z_\beta(A) + \Delta \quad (4.6)$$

where $Z_p(A)$ is the most probable charge and the β -stable charge $Z_\beta(A)$ can be approximated by the smooth function (thus avoiding shell effects) [mar71]

$$Z_\beta(A) = \frac{A}{1.98 + 0.0155 \cdot A^{2/3}}. \quad (4.7)$$

The Δ term, which describes the difference between experimentally obtained values of Z_p and Z_β , was parameterized by Sümmerer *et al.* [sum90] using the form

$$\Delta = \begin{cases} 2.041 \times 10^{-4} \cdot A^2 & \text{if } A < 66 \\ 2.703 \times 10^{-2} \cdot A - 0.895 & \text{if } A \geq 66. \end{cases} \quad (4.8)$$

To describe the additional shift in the charge distribution maxima (Z_p) that is caused by the N/Z ratio of the target/projectile (depending on whether target- or projectile-like residues are studied) an extra “memory effect” term Δ_m was added:

$$Z_p(A) = Z_\beta(A) + \Delta + \Delta_m. \quad (4.9)$$

A fit to the (scarce) experimental data available at the time (see Section 2.1) led to a parametrization for Δ_m in the form

$$\Delta_m(A) = \left[c_1 \left(\frac{A}{A_t} \right)^2 + c_2 \left(\frac{A}{A_t} \right)^4 \right] \Delta_\beta(A_t) \quad (4.10)$$

where A_t is the target mass and $\Delta_\beta(A_t) = Z_t - Z_\beta(A_t)$, in which Z_t is the target proton number and A_t is the target mass. Different values for the coefficients c_1 and c_2 were determined for neutron- and proton-rich fragmentation as the memory effect appeared to be smaller for fragmentation of proton-rich targets/projectiles compared to neutron-rich systems. Figure 4.8 illustrates the dependence of the memory effect Δ_m on the ratio of $A/$

A_p (where A is the fragment mass and A_p is the projectile mass) for the most abundantly produced final fragment of each isobaric chain (the so-called “ridge line”) from the present experiment. The ridge lines are shown also from two other experiments with more neutron-rich krypton isotopes: ^{86}Kr fragmentation at 70 MeV/nucleon [pfa95] and ^{84}Kr fragmentation at 200 MeV/nucleon [ste91]. The hollow symbols are indicative of proton pick-up products. Also indicated in Figure 4.8 (by the dashed line) is the curve representing the parametrization of Eq. 4.10 for the ^{78}Kr fragmentation (the parametrization for the reactions involving ^{84}Kr and ^{86}Kr are not shown on the plot, but exhibit similar agreement to the data as that for the ^{78}Kr fragmentation data). It is apparent that the memory effect for intermediate energy/intermediate mass fragmentation behaves differently than expected from the high energy data. Both the data from the

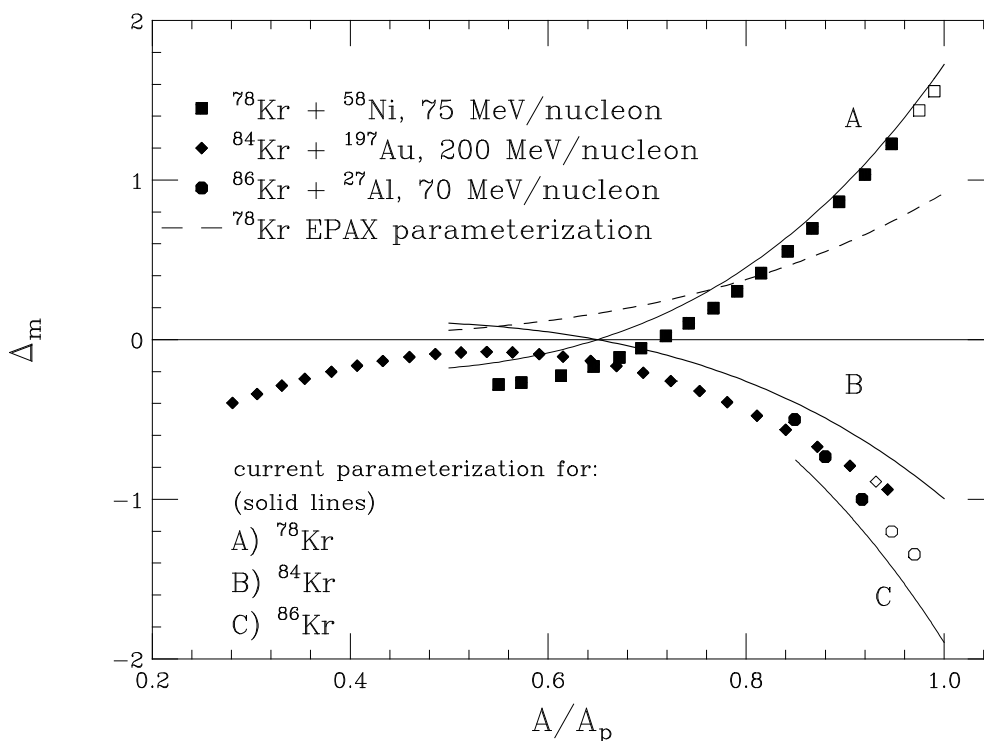


FIGURE 4.8: Parametrization of the memory effect which shows data from several krypton fragmentation experiments.

current proton-rich fragmentation of ^{78}Kr as well as the data from the neutron-rich fragmentation of ^{84}Kr and ^{86}Kr show a much steeper dependence on the mass ratio than the parametrization. Recent measurements with ^{129}Xe and ^{136}Xe beams at 790 MeV/nucleon showed a similar trend for the proton-rich projectile and the reaction products from the neutron-rich projectile (^{136}Xe) as they deviated from the standard parametrization [fri93]. Using a formalism similar to Sümmerer *et al.* [sum90], the memory effect from the three intermediate-energy krypton fragmentation experiments can be described by

$$\Delta_m(A) = \left[c_1 \left(\frac{A}{A_t} \right)^4 + c_2 \left(\frac{A}{A_t} \right) \right] \Delta_\beta(A_t) \quad (4.11)$$

with values of $c_1 = 1.55$ and $c_2 = -0.425$. The modified parametrization was determined by performing a least square fit (with two n-th order polynomial terms) to the experimental data. The c_2 coefficient becomes negative to account for the fact that the proton-rich fragmentation data dips below the $\Delta_m = 0$ line (this effect was also observed in the limited data (see Figure 2.4) used by Sümmerer *et al.* [sum90]). The parametrization shows that fragments far from the projectile approach the valley of β stability ($\Delta_m/\Delta_\beta(A_t) \sim 0$) and those near the projectile mass are close to the N/Z ratio of the projectile ($\Delta_m/\Delta_\beta(A_t) \sim 1$). This modified parametrization does a good job reproducing the experimental data and is indicated by solid curves in Figure 4.8. (Because the ^{86}Kr fragmentation experiment [pfa95] was concentrated on fragments near the Z of the beam, this data is limited to $Z \geq 33$.) It should also be noted that, in contrast to the two other data sets which were measured around 0° , the ^{84}Kr [ste91] data was obtained at angles of 0.6° and 1.5° . The fact that the ^{84}Kr ridge line in Figure 4.8 begins to curve downward for $Z < 20$ indicates that parts of the parametrization used in this analysis are not applicable near and below argon

($Z = 18$), as was discussed by Sümmerer *et al.* [sum90]. Charge pick-up products ($Z > 36$ in this case), which are rarely produced from high energy fragmentation, are commonly observed at intermediate energies. The memory effects for the pick-up products observed in previous krypton fragmentation experiments [ste91, pfa95], as indicated in Figure 4.8 by unfilled symbols, seem to follow closely the general trend of the fragmentation products ($Z \leq 36$). This fact, together with the observation that the overall curvature of the memory effect is steeper than the standard parametrization, is a strong indication that the prefragments are produced by processes other than the “pure” fragmentation that occur in high energy reactions. This assumption is also supported by the relatively large pick-up product cross sections that were observed in the current experiment and the ^{86}Kr fragmentation [pfa95].

4.2.3 Implications for the rp-process

From the isotopic cross sections shown in Figure 4.7, it is possible to estimate the number of ^{69}Br events that should have been observed. Assuming an exponential decrease in cross section near the proton drip line (as is predicted by the EPAX parametrization [sum90]), ~ 300 counts of ^{69}Br should have been observed as determined from the number of ^{70}Br events that were identified. This estimated number of events that should have been observed can, together with the short flight path (~ 14 m from production target to the focal plane silicon telescope), be used to place an upper limit on the half-life of ^{69}Br of 24 ns. Most mass models predict ^{69}Br to be only slightly proton unbound. In the 1993 Atomic Mass Tables [aud93] the value of $S_p = -180 \pm 300$ keV is found from the listed binding energies of ^{69}Br and ^{68}Se . Assuming that the proton is emitted from a $p_{3/2}$ state (as is the case in the mirror nucleus ^{69}Se), the proton penetrability WKB

approximation indicates a half-life of $\sim 10^3$ seconds which implies that the main decay mode is β^+ /EC with an estimated half-life on the order of 100 ms [tak73]. For the WKB approximation a normalized Wood-Saxon nuclear potential was used in conjunction with the centrifugal, spin-orbit, and Coulomb terms as was described by Winger *et al.* [win93]. The recent GANIL experiment [bla95] limited the ^{69}Br half-life to 100 ns or less which corresponds to being proton unbound by at least 450 keV. The current tighter limit on the ^{69}Br half-life of 24 ns or less indicates that this nucleus is proton unbound by at least 500 keV. The present experiment also gives some information on ^{73}Rb . Because of its non-observation in a wide variety of measurements over a number of years [moh91, bla95, aur77, hen94], this isotope should be considered to be particle unbound.

The systematics in Figure 4.5 show that the magnetic rigidity range covered in the present experiment would also have included ^{73}Rb . Using the EPAX parametrization and the observed number of ^{74}Rb events, approximately 75 ^{73}Rb events should have been observed, yielding an effective upper limit of 30 ns for the half-life of ^{73}Rb . In the case of ^{73}Rb , the majority of mass models predict this isotope to be proton unbound. The value of $S_p = -590 \pm 270$ keV determined from binding energies in the 1993 Atomic Mass Tables [aud93] yields a proton emission half-life of ~ 700 ns (using the WKB approximation). The present data limits the half-life of ^{73}Rb to less than 30 ns and assuming the emitted proton comes from the $f_{5/2}$ state (since the mirror nucleus is ^{73}Kr) indicates that ^{73}Rb is unbound by at least 680 keV. Under the previous assumption that ^{69}Br was particle stable [cha92], the rp-process was generally thought to proceed via



In view of their recent results (regarding the particle instability of ^{69}Br), Blank *et al.* [bla95] have proposed an alternative rp-process path:



The most significant modification is that the rp-process must now wait for the decay of ^{68}Se which has a long half-life (1.6 min) relative to the assumed burning time (~ 10 sec) of the astrophysical processes in which the rp-process is likely to proceed to the high mass region ($A > 70$). In processes with extended burning times (~ 100 sec) [wor94, cha92], the rp-process can slowly continue to ^{72}Kr which slows the process due to the fact that ^{73}Rb is unstable and ^{72}Kr has a 17.2 second half-life. Many of the rp-process calculations [wor94, cha92] are extended to ~ 1000 seconds to explore the astrophysical effects of an extended burning time, and in this situation the rp-process could slowly proceed to masses

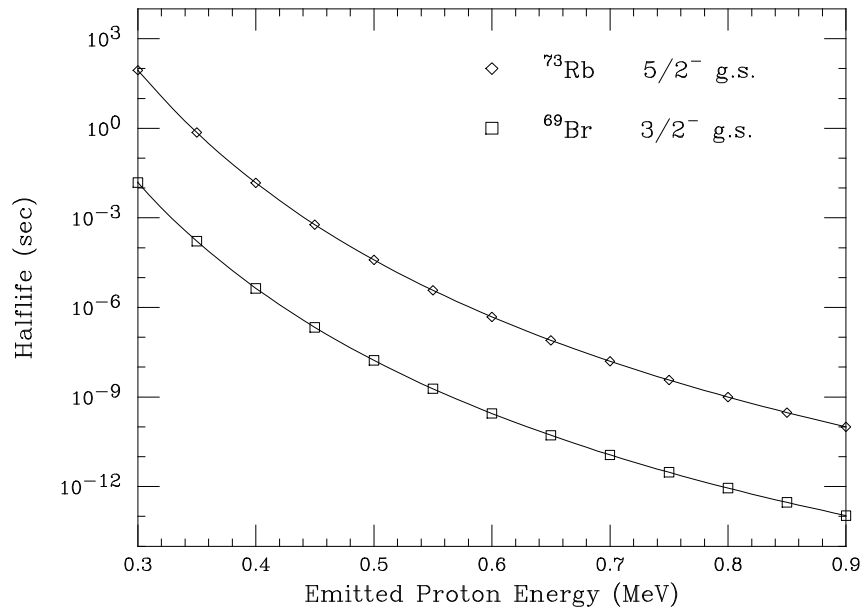


FIGURE 4.9: Half-lives calculated using the WKB approximation for ^{69}Br and ^{73}Rb .

higher than ^{72}Kr . Of the five new isotopes reported by Blank *et al.* [bla95], two (^{60}Ga and ^{64}As) could alter the rp-process path as it approaches ^{68}Se . The other three isotopes (of ^{69}Kr , ^{70}Kr , and ^{74}Sr), however, have no influence on the modified rp-path due to the “bottle-necks” caused by the instability of ^{69}Br and ^{73}Rb . Although no evidence for ^{64}As , ^{69}Kr , and ^{74}Sr was seen in the present experiment (assuming an exponential decrease in cross section and the number of events attributed to ^{65}As , ^{70}Kr , and ^{75}Sr , no counts of ^{64}As , ^{69}Kr , and ^{74}Sr should have been observed), the modified rp-process path presented by Blank *et al.* [bla95] seems to reflect the current experimental evidence accurately.

Chapter 5

Summary

The present work involved systematic measurements of fragment yields from the intermediate energy projectile fragmentation of ^{78}Kr and ^{86}Kr isotopes, and several major points were presented: 1) The EPAX parametrization and the ISApac code can be used with mixed results in the intermediate energy/intermediate mass regime, as is shown in Figure 4.4 and Figure 4.7; 2) when the final observed fragments have acquired one or more protons, their parallel momentum shift can be explained through the use of momentum conservation when the Fermi momentum of the individual protons is considered; and 3) with the results of the present work and some other recent experiments involving intermediate energy krypton fragmentation, modifications to the memory effect parametrization were made. These three points are pertinent for future planning of radioactive nuclear beam experiments - most notably the cross section predictions since it is important to have a reasonably accurate estimate for the time required to produce the required number of a particular exotic isotope. The present work also helped add to the growing database of systematic studies of momentum distributions and cross sections in this energy/mass regime, and the additional information will help in the modification of the EPAX parametrization and the ISApac code.

The experiment on the projectile fragmentation of ^{78}Kr helped supply systematic cross section data but, it also had the specific goal of determining the termination point of the rapid-proton capture process – most notably the particle stability of ^{69}Br . The data shown in Figure 4.6 showed that ^{69}Br is not particle stable, and this will cause the termination of the rp-process. Tight limits were placed on the half-lives of both ^{69}Br and ^{73}Rb (both were considered important to understanding the rp-process) and this data will now have to be incorporated into astrophysical network calculations.

Further research in this area is still necessary in order to gather additional systematic measurements of cross sections and momentum distributions from a variety of target/projectile combinations at varying energies in the intermediate energy/intermediate mass regime.

Appendix A

Measured Cross Sections

The following tables list the experimental cross sections for the individual observed isotopes in the reaction $^{78}\text{Kr} + ^{58}\text{Ni}$ at 75 MeV/nucleon (Table A.1) and the reaction $^{86}\text{Kr} + ^{27}\text{Al}$ at 70 MeV/nucleon (Table A.2). The uncertainty listed is statistical in nature. Further details on other uncertainties can be found in the text along with plots of this data (See Figure 4.4 on page 69 and Figure 4.7 on page 73).

Table A.1 (con't).

Table A.1: Isotopic cross sections from $^{78}\text{Kr} + ^{58}\text{Ni}$ at 75 MeV/nucleon.

Z	A	Cross Section (mb)	Stat. unc. (mb)
21	44	3.85E-02	8.8E-03
21	45	4.73E-02	7.0E-03
21	46	2.91E-02	5.2E-03
21	47	1.21E-02	3.5E-03
21	48	2.29E-02	1.1E-02
22	45	9.50E-03	3.4E-03
22	46	5.33E-02	7.8E-03
22	47	6.76E-02	7.4E-03
22	48	6.53E-02	8.3E-03
22	49	1.04E-01	2.7E-02
22	50	6.46E-01	4.5E-01
22	51	7.55E-03	3.6E-03
22	52	3.10E-03	2.3E-03
23	47	4.56E-03	2.4E-03
23	48	1.99E-02	3.8E-03
23	49	5.37E-02	3.1E-03
23	50	1.47E-01	5.4E-03
23	51	1.17E-01	4.9E-03
23	52	4.95E-02	3.8E-03
23	53	1.23E-02	2.8E-03
24	49	6.52E-03	3.1E-03
24	50	4.54E-02	5.6E-03
24	51	1.86E-01	4.7E-03
24	52	5.33E-01	8.0E-03
24	53	4.73E-01	1.0E-02
24	54	1.60E-01	6.7E-03
24	55	2.39E-02	3.7E-03
25	51	7.36E-03	1.8E-03
25	52	1.04E-01	4.8E-03
25	53	9.01E-01	1.0E-02
25	54	1.99E+00	1.7E-02
25	55	1.15E+00	1.6E-02
25	56	4.17E-01	1.4E-02
25	57	4.38E-02	5.2E-03
26	53	1.46E-02	2.0E-03
26	54	4.37E-01	7.7E-03

Table A.1 (con't).

Z	A	Cross Section (mb)	Stat. unc. (mb)
26	55	3.14E+00	1.9E-02
26	56	4.86E+00	2.7E-02
26	57	3.72E+00	3.6E-02
26	58	7.74E-01	2.0E-02
26	59	5.99E-02	6.7E-03
27	55	4.72E-02	3.3E-03
27	56	1.50E+00	1.5E-02
27	57	1.23E+01	5.9E-02
27	58	1.82E+01	8.2E-02
27	59	8.12E+00	6.1E-02
27	60	1.04E+00	2.3E-02
27	61	1.01E-01	9.0E-03
28	57	1.65E-01	4.7E-03
28	58	3.76E+00	2.7E-02
28	59	1.93E+01	7.0E-02
28	60	2.73E+01	9.3E-02
28	61	1.10E+01	7.3E-02
28	62	1.47E+00	2.6E-02
28	63	1.30E-01	1.0E-02
29	59	3.50E-01	8.1E-03
29	60	5.56E+00	3.3E-02
29	61	3.19E+01	1.2E-01
29	62	3.87E+01	1.4E-01
29	63	1.29E+01	8.4E-02
29	64	1.73E+00	3.5E-02
29	65	1.90E-01	1.2E-02
29	66	1.54E-02	1.8E-03
30	60	2.07E-02	2.5E-03
30	61	7.19E-01	1.4E-02
30	62	8.26E+00	4.3E-02
30	63	4.21E+01	1.5E-01
30	64	4.30E+01	1.5E-01
30	65	1.55E+01	1.0E-01
30	66	5.87E-01	1.6E-02
30	67	1.53E-02	1.4E-04
31	62	2.54E-02	5.0E-03
31	63	6.54E-01	1.4E-02
31	64	1.10E+01	8.5E-02
31	65	3.40E+01	1.5E-01

Table A.1 (con't).

Z	A	Cross Section (mb)	Stat. unc. (mb)
31	66	3.88E+01	1.7E-01
31	67	2.69E+01	1.7E-01
31	68	2.66E+00	6.6E-02
31	69	3.07E-01	9.0E-03
31	70	2.77E-02	2.6E-03
32	64	1.05E-01	8.4E-03
32	65	2.03E+00	2.8E-02
32	66	1.40E+01	7.3E-02
32	67	4.09E+01	1.4E-01
32	68	4.72E+01	1.6E-01
32	69	2.08E+01	1.1E-01
32	70	4.43E+00	4.1E-02
32	71	5.04E-01	1.3E-02
33	66	8.37E-02	7.3E-03
33	67	1.45E+00	2.3E-02
33	68	1.04E+01	6.5E-02
33	69	3.12E+01	1.2E-01
33	70	3.95E+01	1.4E-01
33	71	1.94E+01	9.0E-02
33	72	4.68E+00	3.6E-02
33	73	9.60E-01	4.5E-02
34	68	6.71E-02	6.2E-03
34	69	1.20E+00	2.5E-02
34	70	8.30E+00	5.9E-02
34	71	2.61E+01	1.0E-01
34	72	3.29E+01	1.1E-01
34	73	1.60E+01	6.5E-02
34	74	5.49E+00	4.3E-02
35	70	3.58E-02	4.7E-03
35	71	7.14E-01	1.8E-02
35	72	5.87E+00	5.2E-02
35	73	1.87E+01	8.3E-02
35	74	2.49E+01	8.5E-02
35	75	1.51E+01	5.4E-02
36	72	2.80E-02	4.2E-03
36	73	5.75E-01	1.6E-02
36	74	3.78E+00	4.1E-02
36	75	1.28E+01	6.4E-02
36	76	1.93E+01	6.1E-02

Table A.1 (con't).

Z	A	Cross Section (mb)	Stat. unc. (mb)
37	74	7.81E-03	1.9E-03
37	75	1.32E-01	8.5E-03
37	76	1.23E+00	2.6E-02
37	77	3.06E+00	4.8E-02
37	78	2.14E+00	2.2E-02
37	79	3.59E-01	7.3E-03
38	77	1.86E-02	1.5E-02
38	78	5.03E-02	5.9E-03
38	79	1.55E-01	9.1E-03
38	80	4.69E-02	4.0E-03

Table A.2: Isotopic cross sections from $^{86}\text{Kr} + ^{27}\text{Al}$ at 70 MeV/nucleon.

Z	A	Cross Section (mb)	Stat. Unc. (mb)
33	68	7.57E-02	1.9E-02
33	69	1.46E+00	1.4E-01
33	70	4.99E+00	1.9E-01
33	71	8.92E+00	3.0E-01
33	72	1.38E+01	3.0E-01
33	73	1.58E+01	4.1E-01
33	74	1.09E+01	5.8E-01
33	75	8.58E+00	3.7E-01
33	76	7.66E+00	5.0E-01
34	69	3.87E-02	1.0E-02
34	70	5.25E-01	7.8E-02
34	71	1.31E+00	1.7E-01
34	72	3.41E+00	1.7E-01
34	73	7.60E+00	2.4E-01
34	74	1.43E+01	3.4E-01
34	75	1.67E+01	3.7E-01
34	76	1.83E+01	8.4E-01
34	77	1.34E+01	5.5E-01
34	78	1.08E+01	1.5E+00
35	71	2.62E-02	8.9E-03
35	72	3.05E-01	5.5E-02
35	73	8.18E-01	8.1E-02
35	74	2.35E+00	1.5E-01
35	75	5.85E+00	2.2E-01
35	76	1.17E+01	3.8E-01
35	77	1.75E+01	3.5E-01
35	78	2.45E+01	1.1E+00
35	79	2.11E+01	6.9E-01
35	80	2.30E+01	7.8E-01
36	73	1.26E-02	5.5E-03
36	74	1.86E-01	4.6E-02
36	75	5.80E-01	6.6E-02
36	76	1.55E+00	1.2E-01
36	77	4.38E+00	2.3E-01
36	78	9.69E+00	3.5E-01
36	79	1.73E+01	9.0E-01
36	80	2.68E+01	8.1E-01
36	81	3.68E+01	9.1E-01

Table A.2 (con't).

Z	A	Cross Section (mb)	Stat. Unc. (mb)
36	82	3.40E+01	1.2E+00
37	75	1.13E-02	5.9E-03
37	76	4.79E-02	3.4E-02
37	77	1.04E-01	3.8E-02
37	78	8.97E-01	6.8E-02
37	79	2.41E+00	1.1E-01
37	80	5.97E+00	3.2E-01
37	81	1.26E+01	3.7E-01
37	82	1.55E+01	6.4E-01
37	83	1.76E+01	1.2E+00
37	84	1.96E+01	8.4E-01
37	85	1.49E+01	8.1E-01
38	79	2.84E-02	7.4E-03
38	80	4.21E-01	4.6E-02
38	81	8.03E-01	1.0E-01
38	82	1.32E+00	1.0E-01
38	83	2.35E+00	1.9E-01
38	84	1.73E+00	1.5E-01
38	85	1.32E+00	1.6E-01
39	81	7.79E-02	2.0E-02
39	82	1.13E-01	2.7E-02
39	83	1.76E-01	5.0E-02
39	84	1.32E-01	3.6E-02
39	85	3.58E-02	1.1E-02

Appendix B

ISApce Input Parameters

The following is the input file used for the ISApce [fau92] calculation for the $^{78}\text{Kr} + ^{58}\text{Ni}$ at 75 MeV/nucleon reaction. The input for the ^{86}Kr calculation looked similar other than the target and projectile masses and proton numbers.

```
$PUT
CSA = 0.000000E+00, 1006.500 , 58.00000 , 28.00000 ,
    10.10000 , 10000.00 , 9*0.000000E+00,
AP = 78.00000 ,
ZP = 36.00000 ,
YP = -99.00000 ,
IRAND = 1234567,
CUTOFA = 11*0.000000E+00,
MODEL = 73,
NP = 1,
KNP = 2,
GAPL = 1.100000 ,
IPAULI = 1,
ISONSW = 0,
GAMISO = 0.000000E+00,
IDEN = 7,
JKEY = 3,
MPRIN = 0,
VAP = 0.000000E+00,
VPION = 0.000000E+00,
NZMAN = 6000000,
NTDEL = 3,
RCAS = 3.000000 ,
TIMEF = 20.00000 ,
KASKEW = 0,
NOPOT = 0,
DX = -2.500000 , 1.000000 , 5*0.6000000 , 1.000000 ,
DXP = -2.500000 , 1.000000 , 0.9000000 , 0.6000000 ,
    0.3000000 , 2*0.2000000 , 2*0.3000000 , 7*0.4000000 ,
BDD = 0.000000E+00,
NMIN = 4
$END
```

List of References

- [arm87] P. Armbruster *et al.*, Proc. Fifth Int. Conf. on nuclei far from stability, ed. I.S. Towner, Rosseau Lake, Ontario, Canada 1987.
- [aud93] G. Audi and A.H. Wapstra, Nucl. Phys. A **565**, 1 (1993).
- [aur77] J.M. D'Auria *et al.*, Phys. Rev. Lett. **66B**, 233 (1977).
- [baz90] D. Bazin, D. Guerreau, R. Anne, D. Guillemaud-Mueller, A.C. Mueller, and M.G. Saint-Laurent, Nucl. Phys. A**515** 349 (1990).
- [ber81] G. Bertsch, Phys. Rev. Lett. **46** 472 (1981).
- [ber88] G. Bertsch and S. Das Gupta, Phys. Reports 160, No. 4, 189 (1988).
- [bla95] B. Blank *et al.*, Phys. Rev. Lett. **74**, 4611 (1995).
- [boh36] N. Bohr, Nature **137**, 344 (1936).
- [bol86] L. M. Bollinger, Annu. Rev. Nucl. Part. Sci. **36**, 475 (1986).
- [bor86] V. Borrel, B. Gatty, D. Guerreau, J. Galin, and D. Jacquet, Z. Phys. A - Atoms and Nuclei **324**, 205 (1986).
- [cha92] A.E. Champagne and M. Wiescher, Annu. Rev. Nucl. Part. Sci. **42**, 39-76 (1992).
- [che68] K. Chen, Z. Fraenkel, G.F. Friedlander, J.R. Grover, J.M. Miller, and Y. Shimamoto, Phys. Rev. **166** 949 (1969).
- [chu71] Y.Y. Chu, E.M. Franz, G. Friedlander, and P.J. Karol, Phys. Rev. C **4**, 2202 (1971).
- [fau92] M. Fauerbach, Diploma thesis, TH Darmstadt (1992).
- [fau96] M. Fauerbach, D.J. Morrissey, W. Benenson, B.A. Brown, M. Hellström, J.H. Kelley, R.A. Kryger, R. Pfaff, C.F. Powell, B.M. Sherrill, Phys. Rev. C **53**, 647 (1996).

- [fle74] A. Fleury and J. M. Alexander, *Annu. Rev. Nucl. Part. Sci.* **24**, 279 (1974).
- [fox89] R. Fox, R. Au, and A. VanderMolen, *IEEE Trans. Nucl. Sci.*, 1562 (1989).
- [fri93] J. Friese, H.J. Körner, J. Reinhold, R. Schneider, K. Zeitelhack, H. Geissel, A. Magel, G. Münzenberg, K. Sümmerer, *Proc. of the 3rd Int. Conf. on Radioactive Nuclear Beams (East Lansing, USA, May 1993)*, D.J. Morrissey, Ed., Edition Frontières (Gif-sur-Yvette, France, 1993), pg. 333.
- [gai91] Y.B. Ivanov, V.N. Russkikh, M. Schönhofen, M. Cubero, B.L. Friman and W. Nörenberg, *Proc. Int. Workshop on gross properties of nuclei and nuclear excitations XX*, Hirschegg, Austria, January 1992, ed. H. Feldmeier, Darmstadt 1990, p. 239.
- [gav80] A. Gavron, *Phys. Rev. C* **21** 230 (1980).
- [gol74] A.S. Goldhaber, *Phys. Lett.* **B53** 306 (1974).
- [gol78] A. S. Goldhaber and H. H. Heckman, *Annu. Rev. Nucl. Part. Sci.* **38**, 161 (1978).
- [gos77] J. Gosset, H.H. Gutbrot, W.G. Meyer, A.M. Poskanzer, A. Sandoval, R. Stock, and G.W. Westfall, *Phys. Rev. C* **16** 629 (1977).
- [got91] L. Tassan-Got and C. Stéphan, *Nucl. Phys.* **A524** 121 (1991).
- [hel95] M. Hellström and D. J. Morrissey, *Nucl. Instrum. Methods B* **99**, 342 (1995).
- [hen94] M. Hencheck *et al.*, *Phys Rev. C* **50**, 2219 (1994).
- [hub89] F. Hubert, R. Bimbot, and H. Gauvin, *Nucl. Instrum. Methods B* **36**, 357 (1989).
- [jan88] J. Jänecke and P.J. Mason, *At. Data Nucl. Data Tables* **39**, 185 (1988).
- [kra76] H. J. Krappe, *Annals of Physics* **99**, 142 (1976).
- [luc87] R. Lucas *et al.*, *Nucl. Phys.* **A464**, 172 (1987).
- [mar71] P. Marmier and E. Sheldon, *Physics of Nuclei and Particles* (Academic, New York and London, 1971), Vol. I, p. 15.
- [moh91] M.F. Mohar, D. Bazin, W. Benenson, D.J. Morrissey, N.A. Orr, B.M. Sherrill, D. Swan, and J.A. Winger, *Phys. Rev. Lett.* **66**, 1571 (1991).
- [mon71] E.J. Moniz, I. Sick, R.R. Whitney, J.R. Ficenec, R.D. Kephart, and W.D. Trower, *Phys. Rev. Lett.* **26** 445 (1971).

- [mor89] D.J. Morrissey, Phys. Rev. C **39** 460 (1989).
- [mue93] A. C. Mueller, Proc. of the 3rd Int. Conf. on Radioactive Nuclear Beams (East Lansing, USA, May 1993), D.J. Morrissey, Ed., Edition Frontières (Gif-sur-Yvette, France, 1993), pg. 1.
- [mur83] M.J. Murphy and R.G. Stokstad, Phys. Rev. C **28** 428 (1983).
- [nol89] J.A. Nolen Jr., A.F. Zeller, B. Sherrill, J.C. Dekamp, and J. Yurkon, NSCL Internal Report # MSUCL-694, July 1989.
- [oli79] L.F. Oliveira, R. Donnangelo, and J.O. Rasmussen, Phys. Rev. C **19**, 460 (1989).
- [pfa95] R. Pfaff *et al.*, Phys. Rev. C **51**, 1348 (1995).
- [por64] N.T. Porile and L.B. Church, Phys. Rev. **B310**, 133 (1964).
- [rob90] J.D. Robertson, J.E. Reiff, T.F. Lang, D.M. Moltz, and J. Cerney, Phys. Rev. C **42**, 1922 (1990).
- [sch92] K.-H. Schmidt *et al.*, Nucl. Phys. **A542**, 699 (1992).
- [sch93] K.-H. Schmidt *et al.*, Phys. Lett. **B300**, 313 (1993).
- [ser47] R. Serber, Phys. Rev. **72** 1114 (1947).
- [she91] B.M. Sherrill, D.J. Morrissey, J.A. Nolen Jr., and J.A. Winger, Nucl. Instrum. Methods **B56** 1106 (1991).
- [sou91] G.A. Souliotis, Diploma Thesis, NSCL (1991).
- [sou92] G.A. Souliotis, D.J. Morrissey, N.A. Orr, B.M. Sherrill, and J.A. Winger, Phys. Rev. C **46** 1383 (1992).
- [ste91] C. Stéphan *et al.*, Phys. Lett. **B262** 6 (1991).
- [sum90] K. Sümmerer, W. Brüche, D.J. Morrissey, M. Schädel, B. Szweryn, and Yang Weifan, Phys. Rev. C **42** 2546 (1990).
- [swa94] D. Swan, J. Yurkon, and D.J. Morrissey, Nucl. Instrum. Methods A **348**, 314 (1994)
- [tak73] K. Takahashi, M. Yamada, T. Kondoh, At. Data Nucl. Data Tables **12**, 101 (1973).
- [wal81] R.K. Wallace and S.E. Woosley, Astrophys. J. Suppl. **45**, 389 (1981).

- [web94] M. Weber *et al.*, Nucl. Phys. **A578**, 659 (1994).
- [wes79] G. Westfall *et al.*, Phys. Rev. Lett. **43**, 1859 (1979).
- [win93] J.A. Winger *et al.*, Phys. Rev. C **48**, 3097 (1993).
- [wor94] L. Van Wormer, J. Görres, C. Iliadis, F.-K. Thielemann, and M. Wiescher, Astrophys. J. **432**, 326 (1994).
- [yar79] Y. Yariv and Z. Fraenkel, Phys. Rev. C **20**, 2227 (1979).